

DEVELOPMENT OF METHYLAMMONIUM LEAD TRIBROMIDE FOR DETECTORS OF
IONIZING RADIATION

By

Kaleab Ayalew

Bachelor of Science in Mechanical Engineering
Addis Ababa University
2016

Masters of Science in Mechanical Engineering
University of Nevada, Las Vegas
2019

A dissertation submitted in partial fulfillment
of the requirements for the

Doctor of Philosophy – Mechanical Engineering

Department of Mechanical Engineering
Howard R. Hughes College of Engineering
The Graduate College

University of Nevada, Las Vegas
May 2024



Dissertation Approval

The Graduate College
The University of Nevada, Las Vegas

December 19, 2023

This dissertation prepared by

Kaleab Ayalew

entitled

Development of Methylammonium Lead Tribromide for Detectors of Ionizing Radiation

is approved in partial fulfillment of the requirements for the degree of

Doctor of Philosophy – Mechanical Engineering
Department of Mechanical Engineering

Alexander Barzilov, Ph.D.
Examination Committee Co-Chair

Jaeyun Moon, Ph.D.
Examination Committee Co-Chair

Brendan O'Toole, Ph.D.
Examination Committee Member

Yi-Tung Chen, Ph.D.
Examination Committee Member

Jin Ouk Choi, Ph.D.
Graduate College Faculty Representative

Alyssa Crittenden, Ph.D.
*Vice Provost for Graduate Education &
Dean of the Graduate College*

Abstract

Organic-inorganic hybrid perovskites, such as MAPbBr₃, have garnered significant interest in recent years as a potential material for radiation detection due to their outstanding optoelectronic properties, low-cost solution growth, and easily tunable stoichiometry. As a result, perovskites have emerged as a promising low-cost option for spectroscopy and nuclear imaging applications. However, several challenges must be addressed to develop MAPbBr₃ for ionizing radiation detection. This dissertation presents the development of MAPbBr₃ for radiation detection through three interrelated components. First, an improved crystal growth method was designed and studied to address the large size and high-quality crystals needs of radiation detectors. This method has significantly advanced the growth of MAPbBr₃ single crystals, yielding crystals with fewer trap sites and better performance. These crystals have been thoroughly tested and exhibit exceptional purity, thermal stability, and enhanced optical and electrical properties. Their X-ray detection sensitivity is notably higher than existing materials and meets the requirements of radiation detection. Second, Cl-doping with MAPbBr₃ was studied to enhance material properties necessary for radiation detection. MAPbBr₃ single crystals with varying amounts of Cl doping and their chemical, optical, electrical, and radiation detector performance were evaluated. The results showed that Cl doping successfully enhanced the electrical properties of the crystal, resulting in improved electrical resistivity. Gamma-ray and X-ray detection were achieved, and the X-ray sensitivity of 4% Cl-doped MAPbBr₃ single crystal was found to be 155 times better than the currently widely utilized α -Se X-ray detector material. Lastly, the effect of electrode selection on detection performance was investigated by preparing semiconductor devices with various metal combinations. The results showed that chromium and nickel are excellent electrode selections and

have demonstrated improved X-ray sensitivity. Although certain challenges remain, the methods and developments presented in this dissertation demonstrate the exceptional potential of MAPbBr₃ for detection of ionizing radiation.

Acknowledgment

I would like to acknowledge and send my sincere gratitude to:

Dr. Alexander Barzilov and Dr. Jaeyun Moon for their guidance, mentorship, and advice, without them this could not be possible.

Dr. Ganesh Balakrishnan and his student Shea Tonkinson for their help performing PL measurements.

Dr. Chad Hansley, for letting me use his medical diagnostic X-ray device.

To NNSS detectors group for all their technical support.

To my fellow student, Suraj Pochampally, we have been in this together.

Last, but the most, to my lovely family, for them, I live, for me they live.

Dedication

To the man who inspired me in every way possible, my father Mengesha Ayalew.

And

To my mom, present for my dissertation defense but passed away before we can properly enjoy my graduation. Mom, I miss you every single micro second.

Table of Contents

Abstract.....	iii
Acknowledgment.....	v
Dedication.....	vi
List of Tables.....	xi
List of Figures.....	xii
List of Abbreviations.....	xvi
Chapter 1. Research Background.....	1
1.1 Introduction.....	1
1.2 Gamma-Ray Detection Technologies.....	2
1.2.1 Scintillator Detectors.....	5
1.2.2 Semiconductor Detectors.....	6
1.2.2.1 Ambient Temperature Semiconductor Detectors.....	8
1.3 Interaction of Gamma Rays and X-Rays with Matter.....	10
1.4 Requirements for Semiconductor Gamma Detectors.....	14
1.4.1 Stopping Power.....	15
1.4.2 Band Gap Energy.....	16
1.4.3 Charge Collection Efficiency.....	18
1.4.4 Resistivity.....	20
1.5 Why Perovskite and MAPbBr ₃ ?.....	20

1.5.1 Low-Cost Crystal Growth	21
1.5.2 Radiation Stopping Potential	22
1.5.3 Excellent Semiconductor Property	23
1.5.4 Tunable Stoichiometry.....	24
1.6 MAPbBr ₃ Challenges	24
1.6.1 Crystal Growth Methods	24
1.6.2 Electrode Engineering	25
1.6.3 Low Resistivity.....	26
Chapter 2. Methods.....	27
2.1 Material Synthesis.....	27
2.1.1 MAPbBr ₃ and MAPbCl ₃ Powder Synthesis	27
2.1.2 Single Crystal Growth	28
2.1.2.1 MAPbBr ₃	28
2.1.2.2 Chlorine-Doped MAPbBr ₃	29
2.2 Material Characterization.....	30
2.2.1 XRD.....	30
2.2.2 EDS.....	30
2.2.3 Room Temperature and Cryogenic PL	31
2.2.4 I-V.....	31
2.2.4.1 Resistivity and Trap Density	31

2.2.4.2 Mobility Lifetime.....	33
2.3 Detector Fabrication.....	33
2.4 Radiation Tests	34
2.4.1 X-Ray Detection.....	34
2.4.2 Gamma-Ray Detection.....	36
Chapter 3. Detection of Ionizing Radiation Using MAPbBr ₃ Single Crystals Grown Through Polymer-Assisted Inverse Temperature Crystallization (PAITC) Method	39
3.1 Introduction.....	39
3.2 Polymer-Assisted Inverse Temperature Crystallization (PAITC) Method.....	42
3.3 Results.....	44
3.3.1 X-ray diffractometry analysis.....	46
3.3.2 Photoluminescence (PL) Study	48
3.3.3 I-V Characterization	53
3.3. 4. X-Ray Detection Using MAPbBr ₃ Single Crystals Grown with PAITC Method. ...	58
3.4 Conclusion.....	63
Chapter 4. Radiation Detection Using Cl-doped MAPbBr ₃ Single Crystals Grown Through the Polymer-Assisted Inverse Temperature Crystallization Method.	64
4.1 Introduction.....	64
4.2 Results.....	68
4.2.1 XRD.....	68

4.2.2 EDS.....	70
4.2.3 Photoluminescence (PL) Study	73
4.2.4 I-V Characterization	78
4.2.4.1 Charge Carriers Mobility lifetime product	81
4.2.5 Radiation detection using Cl-doped MAPbBr ₃ single crystals.....	83
4.2.5.1 X-ray detection.....	83
4.2.5.2 γ -ray detection.....	86
4.3 Conclusion	90
Chapter 5. Electrode Engineering for Improved Sensitivity of MAPbBr ₃ X-Ray Detectors	91
5.1 Introduction	91
5.2 I-V characterization.....	95
5.3 X-Ray Detection Performance	97
5.4 Impedance Spectroscopy.....	102
5.5 Conclusion.....	103
Chapter 6. Conclusion and Future Work.....	104
References.....	107
Curriculum Vitae.....	130

List of Tables

Table 1.1. Summary of material properties of selected ambient-temperature radiation detectors	23
Table 3.1. Summary of electrical resistivity and trap density of MAPbBr ₃ single crystals.....	56
Table 3.2. Summary of selected representative X-ray sensitivity of new and commercially available detector materials.....	62
Table 4.1. Summary of EDS measured elemental atomic percentage of MAPbBr ₃ single crystals, prepared with 1% - 4% substitution of MAPbBr ₃ with MAPbCl ₃	72
Table 4.2. Summary of electrical resistivity and trap density of Cl doped-MAPbBr ₃ single crystals.	79
Table 4.3. Summary of selected representative X-ray sensitivity of new and commercially available detector materials.....	85

List of Figures

Figure 1.1. ^{133}Ba gamma-ray spectrum.....	3
Figure 1.2. ^{133}Ba gamma-ray spectrum measured by various photon detectors [40].	4
Figure 1.3. Diagram of a scintillation detector.	6
Figure 1.4. Schematic diagram of ionizing radiation interaction with a semiconductor: (A) Righley scattering, (B) no interaction, (C) Compton scattering, (D) pair production, (F) electron created by annihilation, (F) positron created by annihilation, (G) positron and electron coming together, (H) photoelectric effect, (I) cloud of secondary electrons produced by impact ionization of electrons from C,H and G.....	13
Figure 1.5. Diagram showing the photon cross-sections (interaction probabilities) as a function of the atomic number of the absorber material.[70].....	14
Figure 1.6. Plot showing the intrinsic charge carrier concentration as a function of temperature for Ge, diamond, and MAPbBr_3 semiconductors.	18
Figure 1.7. Cubic crystal structure [79].	21
Figure 1.8. Attenuation length of CZT, TlBr , and MAPbBr_3 , the data taken from NIST XCOM library.	22
Figure 2.1 Schematic illustration of the process to synthesize the MAPbBr_3 powder.....	28
Figure 2.2. Schematic illustration of the process to grow MAPbBr_3 single crystals.....	29
Figure 2.3. Schematic illustration of steps followed to fabricate MAPbBr_3 detectors.	34
Figure 2.4. Image of the X-ray detection setup.	35
Figure 2.5. Image of the custom build detector box.	37
Figure 2.6. Schematic illustration of the radiation spectroscopy setup.	38

Figure 3.1. Depiction of crystal growth steps in standard inverse temperature crystallization method.....	43
Figure 3.2. Crystal growth steps in polymer assisted inverse temperature crystallization method.	44
Figure 3.3. Image of the synthesized MAPbBr ₃ powder(a), single crystal(b),(c) histogram plot comparing the maximum size of single crystal grown through ITC and PAITC methods(d).	45
Figure 3.4. X-ray diffraction patterns of as-prepared MAPbBr ₃ perovskite powder and single crystals.	47
Figure 3.5. The thermogravimetric plot, loss of mass as a function of temperature change	47
Figure 3.6. comparison of room temperature PL emission peak of MAPbBr ₃ single crystal grown through PAITC and ITC methods (a), Comparison of emission peak FWHM under cryogenic PL tests (b).....	51
Figure 3.7. Pseudo color heatmap of temperature-dependent PL emission intensity of MAPbBr ₃ single crystals, grown through ITC (a), grown with 0.1g/ml PPG PAITC (b) Temperature-dependent MAPbBr ₃ PL emission peak position shift observed under cryogenic PL study (c)...	52
Figure 3.8. Current-voltage (I-V) curve of MAPbBr ₃ crystals grown with ITC (a), PAITC methods with PPG amount of 0.01 g/ml (b), 0.02 g/ml (c), and 0.03 g/ml (d).....	55
Figure 3.9. Capacitance-frequency curves of MAPbBr ₃ crystals grown with ITC, (0 g/ml), and PAITC methods with PPG amount of 0.01 g/ml, 0.02 g/ml, and 0.03 g/ml.	56
Figure 3.10. Current-voltage (I-V) curve of MAPbBr ₃ crystals grown with ITC (a), PAITC methods with PPG amount of 0.01 g/ml (b), 0.02 g/ml (c), and 0.03 g/ml (d).....	58
Figure 3.11. Net X-ray photo current-voltage (I-V) curve of MAPbBr ₃ crystals grown with ITC, and PAITC methods with PPG amount of 0.01 g/ml, 0.02 g/ml, and 0.03 g/ml.	60

Figure 3.12. X-ray sensitivity of MAPbBr ₃ crystals grown with ITC, and PAITC methods with PPG amount of 0.01 g/ml, 0.02 g/ml, and 0.03 g/ml.	61
Figure 4.1. Plot of temperature and intrinsic carrier concentration, plot shows intrinsic charged carrier concentration decreases because of band gap widening.....	67
Figure 4.2. X-ray diffraction patterns of the as-prepared precursor perovskite powders (a), MAPbBr ₃ single crystals with and without Cl doping (b), closeup view of the 100face peak of the as grown crystals (c).	69
Figure 4.3. EDS elemental map of Cl-doped MAPbBr ₃ single crystals, 1%, 2%, 3% and 4% Cl doped from top to bottom, respectively.	71
Figure 4.4. Cl to Br atom ratio of Cl-doped MAPbBr ₃ single crystals, prepared with 1% - 4% substitution of MAPbBr ₃ with MAPbCl ₃	72
Figure 4.5. Photoluminescence peaks of MAPbBr ₃ single crystal with 0% - 4% Cl doping (a), and the measured band gap of the crystals (b).....	74
Figure 4.6. Pseudo-color maps of temperature dependent PL emission spectra of pure MAPbBr ₃ (a) 1%, 2% and 4% Cl doped MAPbBr ₃ single crystals (b),(c), and (d), respectively.	76
Figure 4.7. Temperature dependent PL emission spectra of pure (a) and 4% Cl- doped (b)MAPBbr ₃ single crystals.	77
Figure 4.8. Dark current response of MAPbBr ₃ single crystals with 0% up to 4% Cl doping (a), Dark current response of a pure MAPbBr ₃ single crystal (b).	79
Figure 4.9. I-V curves of Cl-doped MAPbBr ₃ single crystals under dark condition with varying amount of Cl doping level 1% (a), 2% (b), 3% (c), and 4% (d).	80

Figure 4.10. photocurrent- electric field curves and fitted modified Hect function (a), (b), (c), (d), and (e), and for 0%, 1%, 2%, 3%, 4% Cl-doped MAPbBr ₃ single crystals, respectively. bar plot of calculated mobility life time product (f).....	82
Figure 4.11. X-ray photo current-voltage (I-V) curve of 0% - 4% Cl-doped MAPbBr ₃ crystals (a), X-ray sensitivity of MAPbBr ₃ crystals grown 0% - 4% Cl-doping (b).	84
Figure 4.12. ²⁴¹ Am 56 keV gamma spectrum acquired using 4% Cl- doped MAPbBr ₃ crystal and Kromek GR1 CZT detector (a), a close-up view of the ²⁴¹ Am spectrums (b).....	88
Figure 4.13. X-ray photo current-voltage (I-V) curve of 0%-4% Cl-doped MAPbBr ₃ crystals (a), X-ray sensitivity of MAPbBr ₃ crystals grown 0%-4% Cl-doping (b).	89
Figure 5.1. Work function of commonly used electrode materials and the energy level of MAPbBr ₃ perovskite.	94
Figure 5.2. Formation energy of metal complex with N type perovskite [144].	95
Figure 5.3. I-curves of MAPbBr ₃ devices fabricated with Cr-Sc-Cr (a), Au-Sc-Au(b) Cr-Sc-Au(c), and Cr-Sc-Ni (d) electrode metal contact.	97
Figure 5.4. X-ray photo current-voltage (I-V) curve of MAPbBr ₃ devices made with various electrode metal combination.	99
Figure 5.5, X-ray sensitivity of MAPbBr ₃ devices made with various electrode metal combination,.....	100
Figure 5.6. X-ray on and off current of MAPbBr ₃ devices made with various electrode metal combination.....	101
Figure 5.7. Frequency-dependent capacitance of MAPbBr ₃ devices prepared with Au-Sc-Au, Cr-Sc-Au, Cr-Sc-Cr, and Cr-Sc-Ni electrode combination.	103

List of Abbreviations

Au - Gold

Br - Bromine

CCE - Charge Collection Efficiency

Cl - Chlorine

Cr - Chromium

CZT - CdZnTe

DMF - Dimethylformamide

EDS - Energy Dispersive Spectroscopy

FA - Formamidinium ($\text{HC}(\text{NH}_2)_2^+$)

FWHM - Full Width Half Maximum

HPGe - High Purity Germanium

ITC - Inverse Temperature Crystallization

I-V - Current Voltage

MA - Methylammonium (CH_3NH_3^+)

MCA - Multi Chanel Analyzer

Ni - Nickel

PA – Polymer Assisted

PAITC – Polymer Assisted Inverse Temperature Crystallization

PL – Photo Luminescence

PPG - Poly Propylene Glycol

SC - Single Crystal

SNR - Signal to Noise Ratio

TRPL - Time Resolved Photo Luminescence

XRD - X-ray Diffractometry

Chapter 1. Research Background

1.1 Introduction

Technological advancements in nuclear science and engineering have enabled the harnessing and use of ionizing radiation to improve our lives[1], [2], [3]. Consequently, radiation detection technologies have found irreplaceable roles in applications such as the detection and analysis of radioactive materials, identification of nuclear security threats, monitoring industrial radiation emissions for safety and compliance, medical imaging, nuclear medicine, and academic research[4], [5], [6], [7], [8], [9], [10], [11], [12], [13], [14], [15], [16], [17], [18], [19][20], [21], [22], [23], [24], [25]. Commercially deployed detection systems require improvements including the use of new materials to reduce costs, improve detection efficiency, and maintain long-term stability[26], [27], [28], [29], [30]. As a result, perovskites have received attention as low-cost and high-efficiency alternatives to state-of-the-art detector materials[26], [31], [32], [33], [34], [35]. This dissertation presents a methodical study conducted in the development of MAPbBr₃ for detectors of ionizing detectors, the first chapter presents a review of the development of detector materials, followed by a discussion of the essential physics and requirements for such detector materials, and explains why methylammonium lead tribromide (MAPbBr₃) perovskite is a good candidate material. Finally, the chapter concludes by discussing the challenges that must be addressed to develop MAPbBr₃ based radiation detectors. The second chapter presents the experimental methods for all the chapters to follow. The third chapter discusses the design and development of polymer assisted crystal growth process. The fourth chapter discusses the rational and results of Cl-doping with MAPbBr₃, the fifth chapter discusses the results of electrode

engineering studies. Lastly the dissertation concludes by discussing conclusion and future work in Chapter 6.

1.2 Gamma-Ray Detection Technologies

First discovered by Paul Villard in 1900 , gamma rays are high-energy electromagnetic waves generated from the nucleus of an atom. Ten years after their discovery, Bragg demonstrated that much like X-rays, gamma rays are an ionizing radiation. The early days of gamma-ray detection were mainly focused on observing their presence using photographic plates, and proper gamma radiation measuring technologies were not developed until 1928 .

In 1928, Hans Geiger and Erwin Wilhelm Muller developed the Geiger-Mueller (G-M) tube, which, in the same year, led to the development of the first radiation counter called the Geiger counter. Geiger counters are composed of a gas-filled tube with a wire-type electrode; when ionizing radiation is incident on the counter, it ionizes the gas and generates an avalanche of electrons, resulting in a current pulse. Counting these electric pulses enables measurements of the intensity of the incident radiation[36], [37], [38]. For specific values of the high voltage applied to the electrode of the gas-filled counter, the generated current pulse can be proportional to the energy of the ionizing radiation incident on the counter, and the counter in such ‘proportional’ mode is used to measure the energy of gamma rays. However, due to their inability to measure gamma-ray energy spectrum, they are entirely used for radiation dosimetry applications.

Gamma spectroscopy is a quantitative measurement of the energy of gamma-ray radiation[39], [40], [41]. A gamma-ray spectrum is a histogram of the number of counts recorded at each specific energy bin. The energy scales of the histograms are calibrated using the known radiation emitters. By measuring the energy of a gamma ray and counting the number of

occurrences, a gamma-ray spectroscopy system produces an energy spectrum (an example is shown in *Figure 1.1.*), the shape and the pattern of such spectral histograms are characteristic of a single radiation source or multiple sources. As a result, the radiation emitters could be fingerprinted by comparing the spectrum generated by the detection system with the gamma spectrum library of radionuclides.

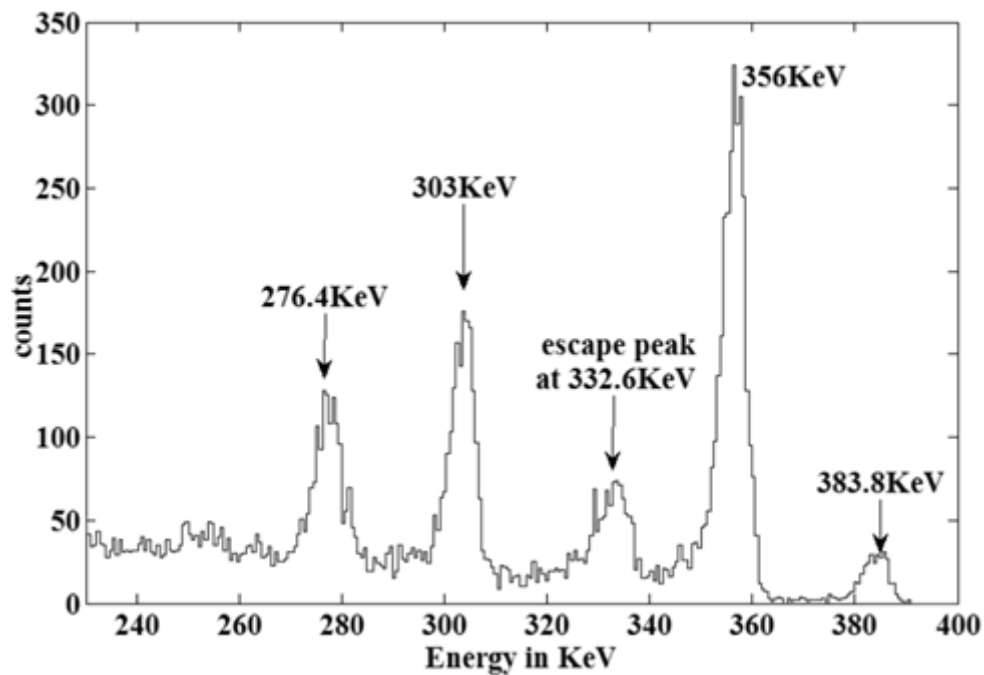


Figure 1.1. ^{133}Ba gamma-ray spectrum.

The spectroscopic gamma detectors are characterized using energy resolution (ER) and detection efficiency (DE). Energy resolution describes the detector's ability to resolve gamma-ray peaks in the energy spectrum; it is defined using the full width at half maximum (FWHM) of a peak, divided by the energy of the peak's centroid[42], [43]. Generally, detectors that generate

sharper peaks are preferred for precise radiation measurements. Scintillators and semiconductors are the two main types of gamma detectors used for gamma spectroscopy. As shown in *Figure 1.2.*, the detector's energy resolution depends on the gamma detector technology and materials. Generally, scintillators underperform semiconductors when it comes to the energy resolution. Gamma detection efficiency (DE) characterizes how well a detector can detect the gamma ray, it is defined as the ratio between the number of counts recorded by the detector to the number of gamma-rays emitted by the source. DE depends on several factors such as, detector material, size, radiation energy, and the source-to-detector distance.

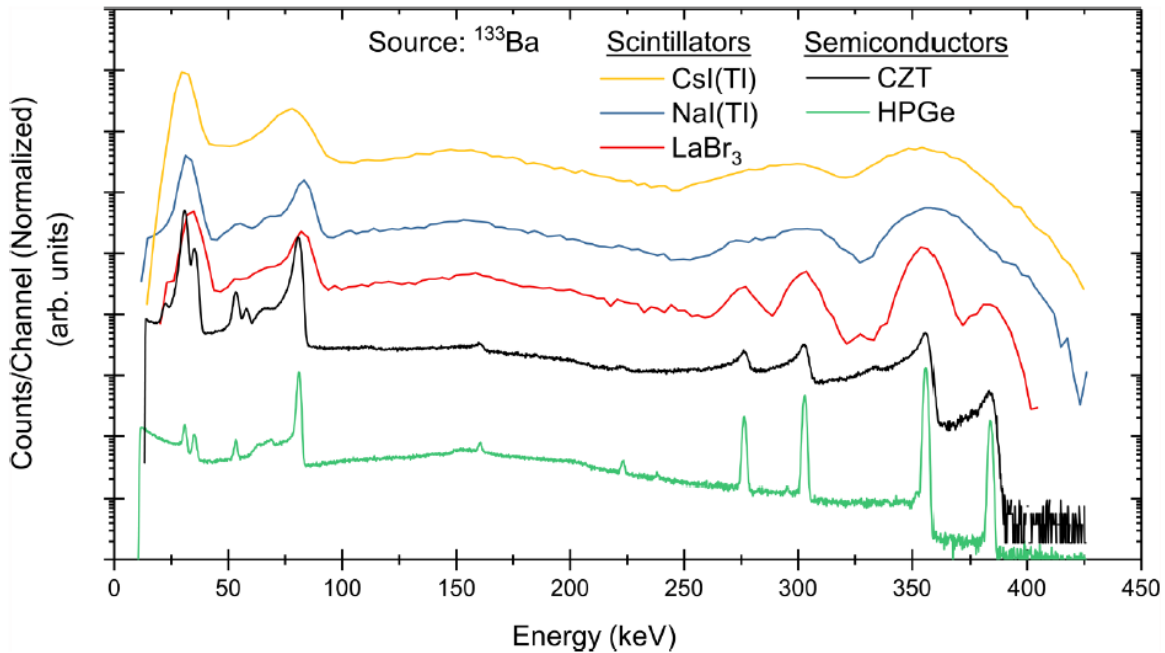


Figure 1.2. ^{133}Ba gamma-ray spectrum measured by various photon detectors [44].

1.2.1 Scintillator Detectors

Scintillator detectors are devices that use scintillating materials that generate light when hit with the ionizing radiation[45], [46], [47], [48], [49][24], [50], [51], [52]. A scintillator detector consists of scintillators that emit light of the intensity that is proportional to the energy of the absorbed radiation, a photodetector that converts the scintillation photons into photoelectrons, and a photomultiplier tube (or a similar optical readout device, e.g., a silicon photomultiplier) that multiplies the electrons thus amplifying the electric current signal at the output anode as shown in *Figure 1.3*.

Scintillation detector materials can be classified into three main categories: organic, inorganic, and liquid scintillators. Each category has its advantages and disadvantages. Liquid and organic scintillators generally have a low atomic number and low stopping power. Consequently, their use for gamma spectroscopy has remained limited. On the other hand, the inorganic scintillator, sodium iodide doped with thallium (NaI(Tl)), is the oldest, most efficient (ER < 10%), and the most widely used for gamma spectroscopy. Despite the tremendous effort applied to improve the ER of NaI(Tl) and other prospective materials, progress have still remained limited [53].

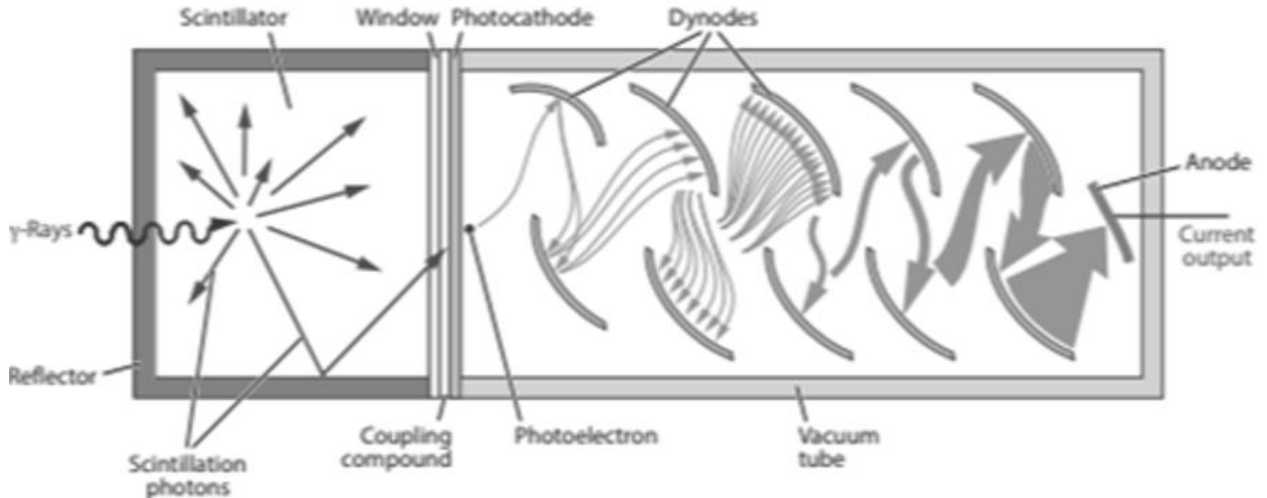


Figure 1.3. Diagram of a scintillation detector.

1.2.2 Semiconductor Detectors

Semiconductor detectors use single-crystal semiconductor wafers that respond to ionizing radiation by directly generating an electric signal[54], [55], [56][57]. The components of a semiconductor radiation detector include a semiconductor wafer and thin layers of metal electrodes deposited on the surface of the wafer. For gamma spectroscopy application, the wafer with electrodes must be connected to a power supply to set the bias voltage across the crystal, and to the electronics to process and analyze the generated signals. The electronics components required are a preamplifier, an amplifier or a digitizer, a multi-channel analyzer (MCA), and a computer.

The main attraction of semiconductor detectors is their ability to provide high energy resolution and efficiency for detecting gamma rays and X-rays. Semiconductor detector materials have a long and fascinating history that reflects the progress of science and technology in physics, chemistry, and engineering. The first modern semiconductor detector was a small p-n junction diode that was built at Bell Laboratories in 1951 [58]. The detector was used to detect alpha particles; however,

the performance of this device was far lower than scintillators, which were the gold standard for radiation detectors of the time.

The real breakthrough occurred in the 1960s, when developments in crystallography enabled the production of high-quality large-size semiconductor single crystals, and the advances in engineering enabled practical pulse height analysis systems. During this period, research focused on the development of silicon and germanium-based alpha and gamma spectroscopy detectors. Alister Tavendale and George Ewan invented a lithium-drifted germanium (Ge(Li)) detector in 1963 [59]. The Ge(Li) detector enabled an order of magnitude improvement in the energy resolution compared to the NaI(Tl) scintillator and, in just one year, replaced scintillator detectors as the gold standard for gamma spectroscopy systems.

During the early 1960s, there were no reliable ways to predict the impurity levels of semiconductor single crystals. As such, there were difficulties consistently building high-quality detector systems. The problem was resolved by the decade's end through research and development funded by the Atomic Energy Commission. At the same time, scientists at Oak Ridge National Laboratory discovered a method to grow Ge crystals of high purity. They named the crystal after the process, high-purity germanium (HPGe) [60]. In about a decade, HPGe crystals made Li drifting obsolete, and the Ge(Li) system evacuated its seat as the gold standard gamma spectroscopy technology to HPGe based systems. Even though HPGe detectors are the best gamma spectroscopy systems we have got to date, they have two main drawbacks. Firstly, HPGe detectors require operationally challenging cryocooling. Secondly, HPGe single crystals are very expensive to produce.

1.2.2.1 Ambient Temperature Semiconductor Detectors

The cryogenic cooling requirements for HPGe have spurred interest in a separate group of semiconductor materials called ambient-temperature semiconductor detectors (ATSD)[61], [62], [63], [64], [65]. While the band gap of HPGe is 0.63eV, ATSDs employ semiconductor crystals with band gap energy greater than 1 eV, which limits the thermal noise and enables reasonable discrimination between the signal and the background noise. The early venture in ASTDs by the Paul Scherrer Institute in Switzerland in 1968 led to the development of cadmium telluride (CdTe) detectors. CdTe crystals have a high atomic number and good stopping power, which enables them to have an appreciable spectroscopic response. However, CdTe suffers from many intrinsic drawbacks, such as low resistivity, low charge collection efficiency, and crystal polarization, which limits the detector's efficiency [44][66], [67], [68], [69], [70].

Many of the CdTe deficiencies were later overcome by doping CdTe with other metals [71]. Brookhaven National Laboratory accomplished the leading work in CdTe doping in 1989, which developed the first zinc-doped CdTe (CZT) detector. CZT detectors often contain less than 15% Zn doping. Zn doping is reported to cause the widening of the CdTe bandgap, increase the resistivity by up to two orders of magnitude, and decrease the polarization by balancing the mobility of electrons and holes [60]. Due to the combined effects caused by Zn doping, CZT has achieved ER below 1% at room temperature [72], [73]. As a result, CZT detectors are the primary ambient-temperature gamma spectroscopy detector systems, and it is not common to see prospective new detectors get compared with CZT.

Despite the outstanding progress in using CZT as an ATSD, growing large-size CZT crystals is an unaccomplished task due to several intrinsic issues [74]. The primary and most challenging

problem is the presence of a secondary phase that appears during the crystal growth; this secondary phase limits the maximum size of the crystal that can be used for the detector. Additionally, the presence of the secondary phase in impurity acts as a quenching site for charge carriers and degrades the detector's performance. Furthermore, CZT is prone to structural defects such as a grain boundary, twins, and secondary density precipitation. Lastly, growing CZT crystals is a very expensive process.

Inspired by the success of CZT, several research groups have explored doping CdTe with other metals; among the studied materials, CdMnTe (CMT) is found to be the most promising and has achieved ER 2.1% at 662 keV [75], like all the Te based materials, CMT falls for the same issues like CZT. An effort has also been made to replace Te with Se to avoid the secondary phase. Crystals of CdZnSe and CdMnSe have been grown and showed a spectroscopic response to ionizing radiation. Nonetheless, the effort has not paid a meaningful dividend yet [76].

The other most developed detector material for ambient-temperature gamma spectroscopy is mercury iodide (HgI_2). Excellent stopping power and high density make HgI_2 suitable for gamma detection applications. Single crystals of HgI_2 are grown through the physical vapor transport (PVT) method; progress in PVT method optimization has unlocked improvement in energy resolution from 3.5% to 1% at 122 keV gamma rays as the crystal size increased from 16 mm^3 to 2000 mm^3 [77]. However, HgI_2 is plagued with a persistent mismatch problem between the movement of holes and electrons, which causes spectroscopy capability loss when both holes and electrons are equal contributors to the signal.

In summary, significant progress has been made towards development of efficient ambient temperature radiation detectors. Despite the progress, the difficulty of growing large crystals and the associated cost has become a bottleneck for the comprehensive utilization of such detectors.

Hence, further advancement in semiconductor radiation detectors requires developing less costly and more efficient materials.

1.3 Interaction of Gamma Rays and X-Rays with Matter

Before discussing the design requirements for gamma-ray detectors, it is expedient to explain how ionizing radiation interacts with matter. Gamma rays and X-rays are high-energy photons that are highly ionizing. The only difference between X-rays and gamma rays is their place of origin; the earlier one originates from the electronic shells of an atom, whereas the latter arises from an atom's nucleus. Depending on the incident photon's energy, ionizing radiation could drive various types of response from the material it interacts with. At energy below 2 MeV, interactions such as photoelectric absorption, Compton scattering, pair production or no interaction could be observed. Energy in excess of 2 MeV can cause photonuclear reactions including photofission (it depends on the type of the target nucleus and the energy of the incident photon), however this type of photons do not exist naturally and they have to be made artificially.

No interaction describes a scenario where literally no interaction or change in the energy of the incident gamma ray is observed after its transport through the matter; it could also be extended to represent **Rayleigh scattering**, which is a process where an incident photon interacts with an electron of an atom and changes its direction without losing a portion of its energy. In either case, the incident gamma ray leaves the material without causing any change or depositing any part of its energy.

Photoelectric effect describes a process by which an interaction of a photon with a semiconductor frees an electron from an atom. All semiconductors have a minimum threshold energy required to separate an electron from the atom, known as pair creation energy (E_p). A good

rule of thumb is that E_p is between two and three times the semiconductor's band gap energy (E_g). In the photoelectric effect, a gamma ray with energy greater than E_p deposits all of its energy and knocks off an electron from the atom. The energy of the separated electron is the difference between the energy of gamma ray and E_p . If the separated electron has enough energy, it will go on to create secondary electrons through impact ionization, which, in the process, generates numbers of free charge carriers, electrons, and holes. As a result, photoelectric effect enables a direct measurement of the gamma-ray energy.

Compton scattering is a process, in which, as the name implies, a gamma ray scatters off of an electron, depositing a portion of its energy and freeing an electron. The conservation of momentum governs the amount of energy deposited (E_{dep}) onto the electron. Both free and atom-bound electrons could have a Compton scatter event. The energy of the Compton-freed electron is essentially the difference between the energy of the incident and scattered gamma rays. A single gamma ray could cause cascades of Compton scattering events, depositing varying amounts of energy in each event; also, a scattered gamma ray could go through the material without having another interaction, which makes Compton scattering the undesired event for spectroscopy applications because of the difficulty of directly measuring the energy of the gamma-ray.

Pair production happens when a high-energy gamma ray interacts with an atom, generating an electron and positron pair. The minimum energy required for pair production is 1.022 MeV. If the incident gamma ray has energy more than 1.022 MeV, the particles produced will carry this excess energy. Once created, the electron and the positron lose their kinetic energy scattering through the material matrix, eventually annihilating by generating 511 keV photons. Most naturally occurring gamma rays have lower energy than the requirements to create pairs. Therefore, pair production is not a primary contributor to gamma-ray detectors' signals.

Figure 1.4 shows the relationship between the probability of occurrence of various interactions based on the energy of the incident radiation and the atomic number of the subject being irradiated. At energy below 1 MeV, the photoelectric effect is the dominant form of interaction; this dominance increases with an increase in Z . Compton scattering is primarily responsible for how an incident photon loses energy in low Z materials. Lastly, high energy radiation (>5 MeV) is more likely to cause pair production. If we assume the irradiated subject is a radiation detector, *Figure 1.5* provides essential guidance on selecting the appropriate material to optimize the desired interaction. For instance, semiconductor radiation detectors mainly employ the photoelectric effect to measure radiation; the plot indicates high Z materials increase the probability of the photoelectric effect. As such, they are sought after for gamma detection.

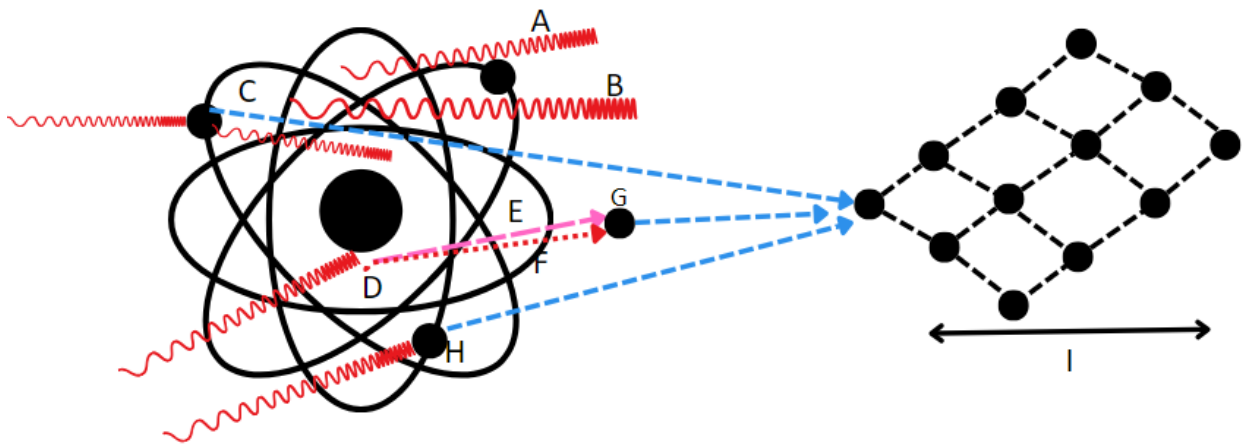


Figure 1.4. Schematic diagram of ionizing radiation interaction with a semiconductor: (A) Rayleigh scattering, (B) no interaction, (C) Compton scattering, (D) pair production, (E) electron created by annihilation, (F) positron created by annihilation, (G) positron and electron coming together, (H) photoelectric effect, (I) cloud of secondary electrons produced by impact ionization of electrons from C,H and G.

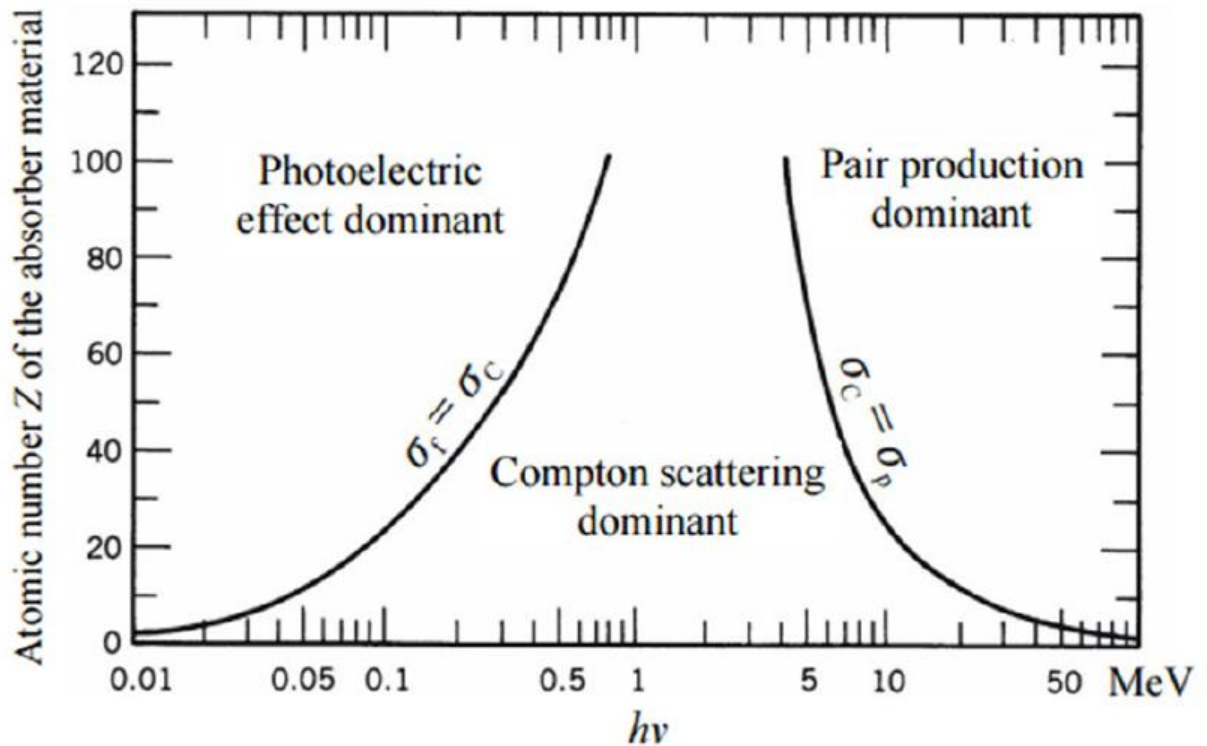


Figure 1.5. Diagram showing the photon cross-sections (interaction probabilities) as a function of the atomic number of the absorber material.[78]

1.4 Requirements for Semiconductor Gamma Detectors

As previously discussed, semiconductor gamma-ray detectors primarily rely on the photoelectric effect to generate charge carriers. The generated charge carriers are subsequently drifted and collected at a metal electrode through the application of an external bias voltage. To achieve efficient detection, three key properties require optimization [71]–[73]. Firstly, the detector material must maximize the probability of gamma-ray interaction within the detector body. Secondly, the excited electrons must possess the capability to generate additional charge carriers

in order to efficiently measure the entire energy. Lastly, the created charge carriers must be collected by the circuitry prior to their loss due to recombination or relaxation to ground states.

1.4.1 Stopping Power

Before delving into the semiconductor properties that pertain to signal generation and collection, it is essential to confirm that the incident radiation can interact with the candidate detector material. Stopping power, which characterizes the detector material's ability to interact with radiation and stop it, is a crucial parameter. The larger the volume, the higher the probability of interaction. In other words, the use of larger-sized crystals is a primary means of increasing the rate of interactions, provided that other material properties are not adversely affected.

Stopping (attenuation) of gamma rays is illustrated by Equation 1-1[78], where μ is the linear attenuation coefficient, I and I_0 are the intensity of incident radiation exiting and entering the detector, respectively; t is the thickness of the detector. As shown in Equation 1-2, the linear attenuation coefficient is a sum of the probabilities of various gamma interactions, photoelectric effect (σ_f), Compton (σ_c), and pair production (σ_p). Also, as shown in Equations 1-3,1-4,1-5, the probabilities of each interaction type are related to the number density (N), atomic number, and energy of the gamma ray. In totality, the equations imply that the attenuation increases with increasing Z (density). Let's compare to what is the state of the art: CZT has an average effective $Z=49$ [58] and density over 5 g/cm^3 ; therefore, materials with Z and density values close to CZT or higher make a good candidate for a radiation detector.

$$\frac{I}{I_0} = e^{-\mu t} \quad (1-1)$$

$$\mu = \sigma_f + \sigma_c + \sigma_p \quad (1-2)$$

$$\sigma_f \propto \frac{NZ^{4-5}}{E_\gamma^{3-4}} \quad (1-3)$$

$$\sigma_c \propto NZ \quad (1-4)$$

$$\sigma_p \propto NZ^2 \quad (1-5)$$

1.4.2 Band Gap Energy

Once it is assured that a gamma ray could be stopped and interacted with in a detector body, the next set of requirements deals with successfully converting the gamma interaction event into an electric signal [78]. The first parameter in this line is the energy required to ionize (activate) an electron-hole pair from the atoms of the detector material. The pair creation energy (E_p) is directly related with the band gap energy of the semiconductor detector; generally, E_p is more than two times the band gap energy[44]. Semiconductors with a low bandgap require relatively lower energy to ionize an atom releasing an electron, due to that higher number of charge carriers could be generated from a single interaction. In addition, the minimum ionization energy is the best energy resolution a detector could achieve, which enhances the need for narrow-bandgap materials. However, semiconductors with narrow E_g are susceptible to enhanced thermal activation of charge carriers, which generates significant background noise signal. Perfect example for this situation is HPGe, this detector has a bandgap energy of 0.63 eV [44] which makes it ideal for high energy

resolution measurements, however, the low bandgap means the detector could easily be thermally activated at room temperature, which completely inhibit its spectroscopic capacity. Therefore, cryogenic cooling is required to prevent thermal activation of the HPGe detector.

Designing a room temperature detector requires a barbell balancing act between maximizing the number of charge carriers created per a gamma-ray interaction and minimizing the background noise level to discriminate each gamma interaction effectively. The maximum amount of charge carriers generated from a single gamma interaction (N_T) is directly related to the band gap energy, as illustrated by *Equation 6*. The noise-causing intrinsic carrier concentration is an exponential function of the band gap and operating temperature. The intrinsic charge carrier concentration (N_i) is the number of available charge carriers in a pure semiconductor at a given temperature (T), N_i could be calculated using *Equation 7*, where n_c , and n_v are effective densities of states related to masses of electrons and holes in the conduction and valence bands, respectively, and k is the Boltzmann constant. As shown in *Figure 1.6*, N_i increases with temperature and decreases with an increase in band gap. Ge, which has the narrowest band gap, has significantly higher N_i , which caused the need for cryogenic cooling to decrease noise; meanwhile, a diamond, the material with the largest band gap among the listed, has minimal carrier concentration, which is excellent for room temperature operation. However, diamond has not been able to achieve spectroscopic response yet, due to the large pair creation energy it requires and the reduced number of carriers available. Therefore, an excellent band gap ‘sweet spot’ for ambient-temperature radiation detector semiconductor material is between 1 eV and 3 eV.

$$N = \frac{E_\gamma}{E_g} \quad (1-6)$$

$$N_i = \sqrt{n_c n_v} \exp\left(-\frac{E_g}{2kT}\right) \quad (1-7)$$

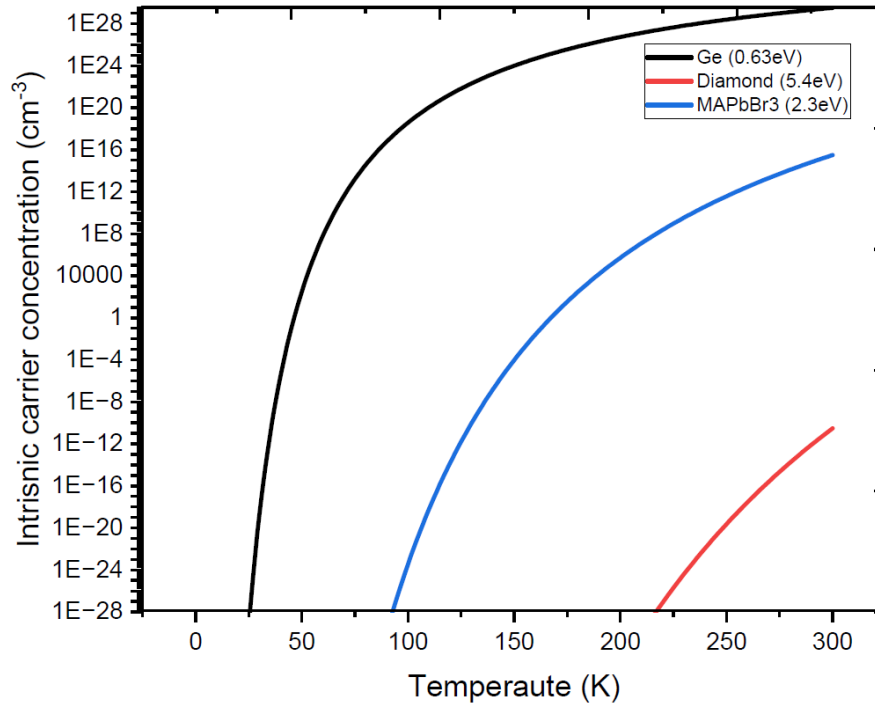


Figure 1.6. Plot showing the intrinsic charge carrier concentration as a function of temperature for Ge, diamond, and MAPbBr₃ semiconductors.

1.4.3 Charge Collection Efficiency

Charge collection efficiency (CCE) measures the ratio of radiation-generated charge carriers that can effectively travel across the detector thickness (d) and be registered as a signal. Various semiconductor and externally applied parameters affect the charge collection efficiency. These parameters could be mathematically related to CCE, as shown in *Equation 8* [79]

$$CCE = \frac{Q}{Q_o} = \frac{\mu_e \tau_e V}{d^2} \left[1 - e^{-\left(\frac{d^2}{\mu_e \tau_e V}\right)} \right] + \frac{\mu_h \tau_h V}{d^2} \quad (1-8)$$

where Q and Q_o are the charge collected and the charge generated from the incident radiation, respectively, $\mu_e \tau_e$ and $\mu_h \tau_h$ are the mobility - lifetime products for electrons and holes, respectively, V is the externally applied bias voltage. The parameter $\mu\tau$ is also known as the mobility-lifetime product; it is an often-cited figure of merit in semiconductor radiation detectors because it describes the potential of charge collection efficiency in any given crystal. The charge collection efficiency is strongly imposed by the $\mu\tau$ product, therefore materials with higher value of $\mu\tau$ are sought after to optimize the CCE of a radiation detector. The current state-of-the-art ambient-temperature detector CZT has $\mu\tau$ in excess of $10^{-3} \text{cm}^2/\text{V}$, a material with $\mu\tau$ value closer to the one of the CZT or better makes for a good candidate for radiation detectors.

Semiconductors are prone to various types of defects ranging from point to volumetric defects. These defect sites affect both the mobility and lifetime of carriers. In the case of mobility, defect sites slow down and reduce the charge mobility by acting as a scattering point. Also, defect sites affect charge lifetime by acting as a trap site, that charge carriers could be trapped for a time while in route to collection points, which overall reduces the effective lifetime during which a carrier could be collected. In a nutshell, the defect concentration is inversely proportional to both the mobility and the lifetime of charge carriers; as a result, to optimize the charge collection efficiency, materials with low defect concentrations are preferred.

1.4.4 Resistivity

The external applied bias voltage is the driving force for the collection of charge carriers in gamma detectors. A higher driving force means higher efficiency of collecting the generated charge carriers. However, the ability to apply bias voltage is dependent on the intrinsic resistivity of the detector material. Higher resistivity is required to limit the collection of thermally activated charge carriers and the noise level. The currently commercially available ambient-temperature gamma detectors have a resistivity of $10^9 \Omega\text{-cm}$ or greater. Therefore, an ambient-temperature gamma detector requires better or similar resistivity value.

1.5 Why Perovskite and MAPbBr₃?

Recently, perovskites have garnered tremendous attention as a semiconductor material for various applications due to their success at significantly improving solar cell efficiencies [79], [80], [81], [82], [83], [84]. The excellent electrical and optical properties, flexibility of manufacturing methods, lower cost of growing perovskite crystals make them good candidates for radiation detection systems. Below, a brief discussion is provided about perovskite structures, and what makes them good candidates as new materials for radiation detection.

Perovskites represent a variety of materials that share ABX₃ structure, where A sites are occupied by a monovalent cation such as Cs, Methylammonium (MA), and Formamidinium (FA). B sites are for divalent cation such as Pb, Sn, Ge, and X is halide anions such as Cl, Br, I. The shape of a perovskite structure is governed by the Goldschmidt tolerance factor $t = (r_A + r_x) / \sqrt{2}(r_B + r_x)$ [85]. A value of t between 0.8 and 1 is required to form a perovskite material. A unity value of t gives an ideal cubic structure (see *Figure 1.7*) whereas as the value of t decreases to 0.8, the structure trends towards orthorhombic shape.

The discovery of halide perovskites dates to 1893, when CsPbBr_3 was synthesized by wells for the first time. Later organic-inorganic halide perovskites were discovered by replacing the A sites with the organic MA and FA. The simplicity to completely or partial substitute A, B, and X site is what gives perovskite the amenability to fine-tune the property of the material. Literature indicates that halide substitution allows for tuning band gap, B site substitution could enable increase in carrier density as in the case of Bi^{3+} doping with Pb. Lastly, A site replacements have shown promising results in stabilizing the perovskite structure [44], [86].

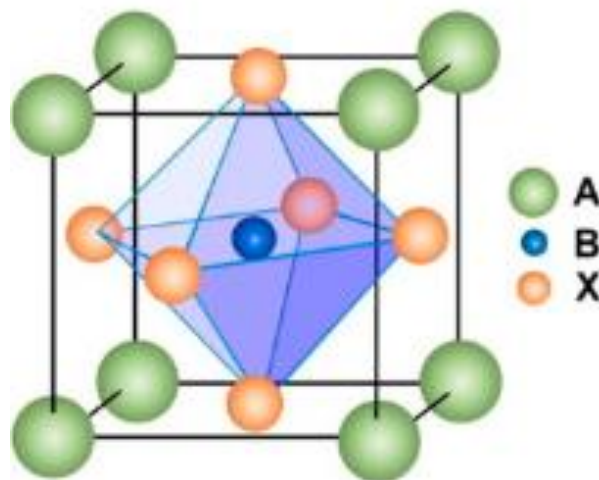


Figure 1.7. Cubic crystal structure [87].

1.5.1 Low-Cost Crystal Growth

Almost all commercial grade semiconductor radiation detectors are produced through expensive high temperature furnace growth methods. It costs more than \$10,000 and \$2,000 [88] to grow a 1 cm^3 of HPGGe and CZT radiation detector grade single crystals, respectively. While MAPbBr_3 single crystals can be fabricated through an easy solution method of mixing precursor powders, and it costs less than \$10 to grow a 1 cm^3 single crystal. Although, less controllable, and

the quality of single crystals made through solution method could be lower than the furnace method, the defect tolerance behavior of perovskite could still enable them to be an excellent low-cost option for ambient-temperature radiation detection applications.

1.5.2 Radiation Stopping Potential

Previous discussions have shown that materials with high Z value have better stopping power for ionizing radiation. MAPbBr_3 is a material with a high effective Z value of 67.13 [89], which is higher than the average atomic number of CZT ($Z=49$). This is because MAPbBr_3 contains Pb ($Z=82$) atoms, which compensate for the low Z elements such as C, N, and H. Although MAPbBr_3 has a lower density (3.5 g/cm^3) than CZT, its attenuation coefficient is higher at a low radiation energy, as shown in *Figure 1.8*. Therefore, MAPbBr_3 has a good potential as a detector material due to its high radiation stopping ability.

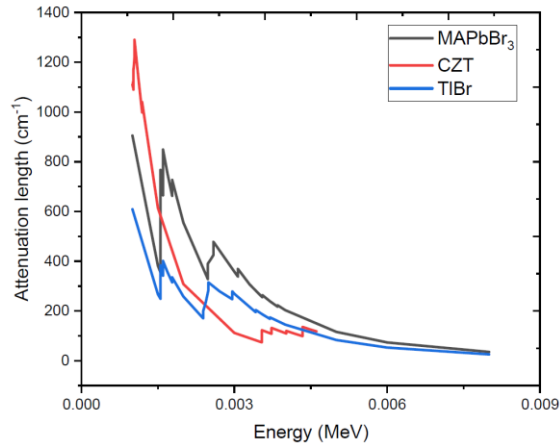


Figure 1.8. Attenuation length of CZT, TlBr, and MAPbBr₃, the data taken from NIST XCOM library.

1.5.3 Excellent Semiconductor Property

Radiation detection at ambient temperature requires a material with a wide band gap to avoid thermal excitation of charge carriers. MAPbBr₃ is a material that meets this criterion, with a reported band gap of 2.3 eV, which is within the optimal range of 1 eV to 3 eV. Moreover, MAPbBr₃ has a high charge carrier mobility-lifetime product, up to 10⁻² cm²V⁻¹ (as shown in *Table 1.1*). This is an important factor for achieving high energy resolution and charge collection efficiency. Unlike many other detector materials, MAPbBr₃ also has balanced transport properties for both holes and electrons, which can prevent polarization effects and enhance the detector performance. Therefore, MAPbBr₃ is a promising candidate for ambient-temperature radiation detection.

Table 1.1. Summary of material properties of selected ambient-temperature radiation detectors

Material	Density (g/cm³)	Band gap (eV)	Resistivity ($\Omega \cdot cm$)	$\mu_e \tau_e$ (cm²V⁻¹)	$\mu_h \tau_h$ (cm²V⁻¹)	Ref.
CdTe	5.85	1.44	10 ⁹	3×10 ⁻³	2×10 ⁻⁴	[90]
CZT	5.78	1.57	10 ¹⁰	4×10 ⁻³	1.2×10 ⁻⁴	[90]
TlBr	7.56	2.68	10 ¹²	5×10 ⁻⁴	2×10 ⁻⁶	[91]
CsPbBr₃	4.85	2.25	10 ⁹	1.7×10 ⁻³	9.5×10 ⁻⁴	[92]
MAPbBr₃	3.58	2.3	10 ⁷	1.2×10 ⁻²	2.1×10 ⁻²	[89]

1.5.4 Tunable Stoichiometry

MAPbBr₃ is a versatile material that can be easily modified by adding or substituting different ions at any of its perovskite sites (A, B, and X). This allows for tailoring the material properties for specific applications. For example, Li can be added at the A site to make MAPbBr₃ sensitive to thermal neutron detection, or Br can be replaced by Cl at the X site to increase the bandgap and improve the gamma-ray and X-ray detection performance. Therefore, MAPbBr₃ offers a promising opportunity to design customized detector materials by manipulating its ionic composition.

1.6 MAPbBr₃ Challenges

1.6.1 Crystal Growth Methods

The development of efficient radiation detection technologies requires large volume, and high-quality single crystals[93], [94], [95]. In recent years, the growth of perovskite crystals has been a central area of research due to its pivotal role in this endeavor[96], [97], [98]. Conventional radiation detectors have traditionally been fabricated using crystals grown from precursor powder melts, which offer meticulous control over the growth process and result in high-quality crystals[99], [100], [101]. However, the organic components of hybrid perovskites exhibit high-temperature instability, rendering melt growth methods ineffective and prompting a shift towards low-temperature solution processes. While these methods offer advantages in terms of flexibility and cost-effectiveness, the single crystals produced through such methods are significantly lower in quality, and growing large crystals through these methods is challenging. Therefore, there is a need to explore alternative methods for producing high-quality single crystals of MAPbBr₃.

1.6.2 Electrode Engineering

The signal generating crystal and the external circuit system that measures and interprets the signal are connected only by electrode contacts. Hence, producing an efficient and reliable contact surface is obligatory for the detector system to achieve its desired purpose. However, despite the due attention it received, developing a stable contact interface has remained an elusive task because of the high polarity and chemical reactivity of the ionic bond in perovskites.

Selection of electrode material should consider several factors. Traditionally the utmost importance in the selection process was given to matching the work function of the semiconductor crystal and the metal. The work function is defined as the minimum energy required to remove an electron from a material. Matching the work function is necessary because a mismatch causes inefficient charge transfer. In the case of a higher electrode work function, there will be a potential barrier at the metal-semiconductor interface that prevents the electrons from flowing freely, which leads to a high leakage current and a low signal-to-noise ratio. On the other hand, in the case of lower electrode work function, electrons will scatter from the electrode and build up on the surface; the buildup will then reduce the effectiveness of the externally applied electric field and cause charge collection efficiency loss.

Another set of considerations for selection is electrode materials reaction with the crystal's surface. Contrary to most traditional detectors, which mainly comprise stable covalent bonding, perovskites are composed of very mobile and active ionic components. The highly reactive crystal surface can often cause an electrochemical reaction with the electrode material. The electrochemical effect is reported [102], [103] to cause several undesired results, such as corrosion

of electrode materials, unstable contact interface, diffusion of electrode metal into the perovskite crystal lattice, and vice versa.

1.6.3 Low Resistivity

The reported resistivity values (10^7 - 10^8 Ω .cm) of MAPbBr₃ are low compared to traditional detector materials (10^9 - 10^{11} Ω .cm) [89]. Due to such a fact, building a spectroscopic MAPbBr₃ is a challenging task. Low resistivity affects detector signal in two main ways; primarily, it prevents enhancement in carrier drift length. Drift length is defined as the product of carrier mobility, lifetime, and the applied electric field ($\mu\tau E$) and in addition to improving the quality of the crystal, which enhances the $\mu\tau$ part of the equation, in gamma spectroscopy, it is a common practice to apply large electric field to increase the carrier drift length and reduce charge trapping. But an increase in the electric field also increases the dark current. Therefore, large resistivity is required. Besides, low resistive materials have significant leakage current and noise levels, which causes a low signal-to-noise ratio; to a certain extent, a very high noise could completely mask the detector signal and make it unusable.

Chapter 2. Methods

2.1 Material Synthesis

The chemicals employed in this study were acquired from Sigma Aldrich with a purity of more than 99.9%, and were utilized without further purification. The following is a list of the chemicals used in the experiment: Lead (II) acetate trihydrate ($\text{Pb}(\text{Ac})_2 \cdot 3\text{H}_2\text{O}$), hydrobromic acid (40 wt% in water), hydrochloric acid (36.5 wt% in water), methylamine (CH_3NH_2 , 40 wt% in water), γ -butyrolactone (GBL, $\geq 99\%$), N, N-dimethylformamide (DMF, $\geq 99.9\%$), Polypropylene glycol (PPG) with a molecular weight of 2000 Da, 200 proof ethanol, and toluene.

2.1.1 MAPbBr_3 and MAPbCl_3 Powder Synthesis

The synthesis of MAPbBr_3 powder was achieved by combining lead acetate trihydrate ($(\text{CH}_3\text{COO})_2\text{Pb} \cdot 3\text{H}_2\text{O}$), methylamine (CH_3NH_2) (40 wt% in water), and hydrobromic acid (HBr) (40 wt% in water) as shown in *Figure 2.1*. First, the lead acetate trihydrate powder was mixed with hydrobromic acid in a 1:6 molar ratio, and the solution was stirred until the lead acetate trihydrate was completely dissolved, which typically takes an hour. Then, methylamine with a molar ratio of 1:1 with the lead acetate tri hydrate was added to the solution dropwise, resulting in the formation of MAPbBr_3 precipitate. The solution was stirred for 2 hours, and the precipitate was collected and washed with pure ethanol four times using a centrifuge. Finally, the powder was dried in a vacuum oven at 60°C for 4 hours. The synthesis of MAPbCl_3 powder was accomplished by following the same steps used for the synthesis of MAPbBr_3 and by replacing hydrobromic acid with hydrochloric acid.

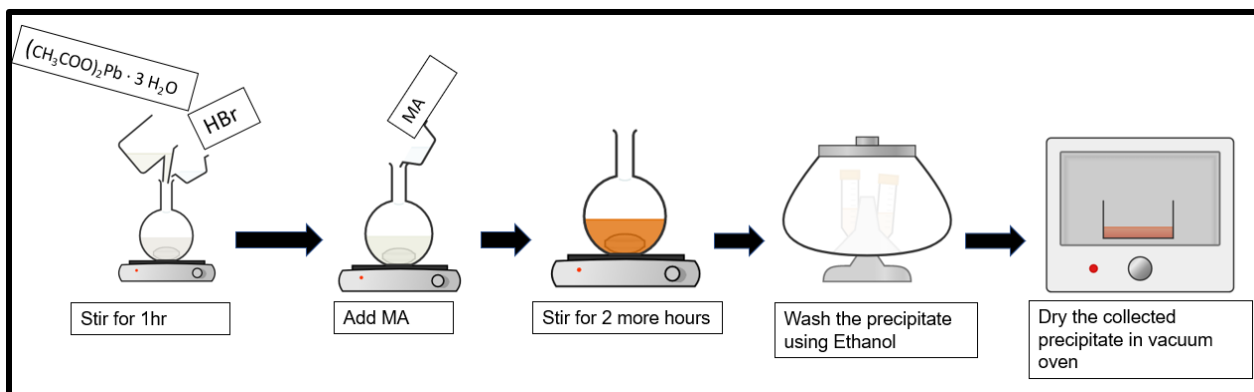


Figure 2.1 Schematic illustration of the process to synthesize the MAPbBr₃ powder.

2.1.2 Single Crystal Growth

2.1.2.1 MAPbBr₃

In a standard polymer-assisted crystal growth process, as illustrated in *Figure 2.2*, 2.5 g of the as-prepared MAPbBr₃ powder was dissolved in 6 ml of DMF solvent at room temperature. The resulting solution was stirred at room temperature for 4 hours to ensure complete dissolution, after which (0.01 - 0.03 g/ml) polypropylene glycol (PPG) was added and the mixture was stirred for an additional 4 hours. Subsequently, the solution was filtered through a 0.2 μm PTFE filter to eliminate particulate matter and unwanted nucleation sites. The filtered solution was then placed in an oil bath at 40°C, and the temperature was increased at a rate of 5°C per hour until it reached 60°C, at which point small crystals began to form and grow over the next two days. Finally, the solution containing the single crystals was removed from the oil bath and the crystals were collected and washed with toluene to eliminate organic solvents from the crystal surface. To compare the effects of utilizing and not utilizing polymers, MAPbBr₃ crystals were also grown without the PPG addition step.

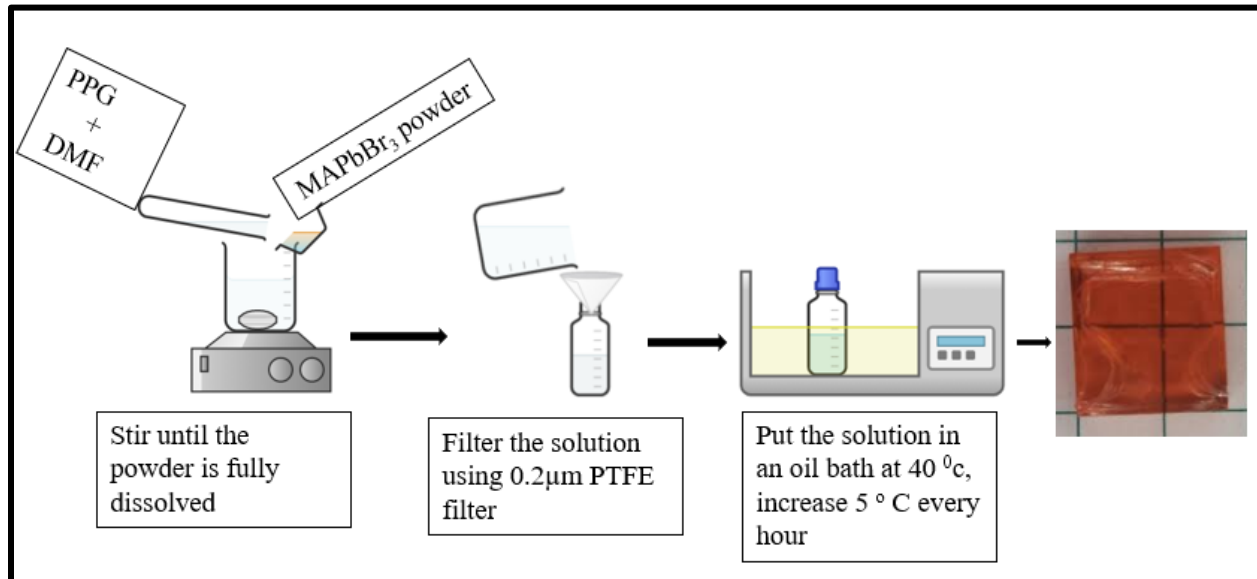


Figure 2.2. Schematic illustration of the process to grow MAPbBr₃ single crystals.

2.1.2.2 Chlorine-Doped MAPbBr₃

The Cl-doped MAPbBr₃ single crystals were obtained by employing procedures similar to those utilized for the growth of pure MAPbBr₃ with a polymer, with the exception that a portion of MAPbBr₃ was replaced with MAPbCl₃ to achieve varying degrees of Cl doping. To accomplish this, 1% - 4% of 2.5 g MAPbBr₃ was replaced with MAPbCl₃ powder, and the resulting mixture was dissolved with 6 ml of DMF solvent at room temperature. The solution was then stirred at room temperature for 4 hours to ensure complete dissolution, after which 0.01 g/ml of polypropylene glycol (PPG) was added, and the mixture was stirred for an additional 4 hours. To eliminate particulate matter and unwanted nucleation sites, the solution was subsequently filtered through a 0.2 μm PTFE filter. The filtered solution was then placed in an oil bath at 40°C, and the temperature was increased at a rate of 5°C per hour until it reached 60°C, at which point small

crystals began to form and grow over the next two days. Finally, the solution containing the single crystals was removed from the oil bath and the crystals were collected and washed with toluene to eliminate organic solvents from the crystal surface.

2.2 Material Characterization

A range of standard methods of material characterization was employed to evaluate the chemical, optical, and electrical properties of the crystals. Specifically, X-ray diffractometry (XRD), Scanning Electron Microscopy (SEM), and Energy Dispersive Spectroscopy (EDS) were utilized to assess the purity, composition, and crystallinity of the precursor powder. Additionally, room temperature and cryogenic photoluminescent (PL) studies were conducted to investigate the optical properties of the material, while I-V characterization was performed to examine the detectors' charge mobility, defect concentration, and resistivity.

2.2.1 XRD

The X-ray diffraction (XRD) patterns of pure MAPbBr₃ powders and single crystals, as well as those of MAPbCl₃ and Cl-doped MAPbBr₃ single crystals, were obtained using a Burker V8 powder XRD instrument with Cu K α emission. In the standard XRD testing process, the raw XRD data was initially acquired by surveying the as-prepared samples from 10 to 90 degrees with a scanning rate of 0.7 degrees per minute. Finally, the raw data was processed using MATCH software to determine the phase and unit cell of the samples.

2.2.2 EDS

The surface imaging and elemental composition of the MAPbBr₃ single crystals were assessed using a scanning electron microscope and an energy-dispersive X-ray spectroscope (SEM/ EDS, JSM-5610, JEOL Ltd., Tokyo, Japan).

2.2.3 Room Temperature and Cryogenic PL

The PL emission spectrum of MAPbBr₃ single crystals was obtained using a setup that included a 500 nm, 25 mm diameter high-performance long-pass filter, neutral density filters, an optical chopper monochromator, a lock-in amplifier, and a 2151 silicon femtowatt detector. A helium cryopump system was used to range the vacuum chamber temperature from room temperature to 13 K. To acquire room temperature PL spectra, the diode laser was turned on to 7.0 V with a current of approximately 1.20 A. The laser passed through the optical chopper and neutral density filters, which were placed in front of the perovskite sample. The 450-nm laser light emission was filtered by the 500 nm long-pass filter positioned in front of the monochromator, while the sample light emission was collected by the monochromator and silicon femtowatt detector. The signal was then recorded by the lock-in amplifier and processed on a computer. The same process was followed for the cryogenic PL, with the perovskite placed on a copper cold head cooled by compressed helium and held in place with Apiezon N grease.

2.2.4 I-V

2.2.4.1 Resistivity and Trap Density

In order to investigate the I-V response of the crystal, as well as to determine the resistivity and the trap density, measurements of DC current were taken under dark condition, by completely shielding the device from light. High-quality crystals among the as-grown crystals were carefully selected and prepared, with both faces being polished mechanically, and lastly, metal electrode contacts were deposited on both sides. The devices were then placed under a dark environment, and the current response was measured as the bias voltage was swept from 0 to 20 V using a Keithley 2450 source measuring unit (SMU).

Typically, the I-V curves of crystals exhibit both linear and non-linear regions. According to the space charge limited current (SCLC) theory, these regions can be further divided into multi [104], [105], [106]. In the low voltage region, the current is linearly related to the voltage, and the linear region of the I-V curves is governed by Ohm's law, which was used to calculate the resistivity of the crystals. The second region emerges after all defect sites are filled with charge carriers, and the current begins to rise rapidly at the onset voltage of the trap-field limit (V_{TFL}). Thus, defect trap density can be determined using *Equation 2-1*, where ϵ is the material's dielectric constant, ϵ_0 is the vacuum permittivity, e is the charge of an electron, and d is the thickness of the crystal [17]. To determine the relative dielectric constant of the samples, the capacitance was measured using an East Taster ET 4510 inductance capacitance resistance (LCR) meter, and the relative dielectric constants were calculated from the measured capacitance using *Equation 2-2*, where C is the capacitance, and A is the active electrode area of the devices.

$$V_{TFL} = \frac{en_{trap}d^2}{2\epsilon\epsilon_0} \quad (2-1)$$

$$\epsilon = \frac{Cd}{\epsilon_0 A} \quad (2-2)$$

2.2.4.2 Mobility Lifetime

The evaluation of the mobility lifetime product ($\mu\tau$) for the fabricated crystals was carried out by measuring the photocurrent response of MAPbBr₃ devices through exposure to blue LED light with a wavelength of 365 nm and a power output of 12 W, while simultaneously sweeping an electric field from 0 to 20 V using a Keithley source measuring unit 2450. The relationship between photocurrent and bias voltage was utilized according to the modified Hecht Equation [4], as shown in *Equation 2-3*, where I_o is the saturated current and L and V represent the device thickness and bias voltage, respectively.

$$I_o = \frac{I_0 \mu \tau V}{L^2} \frac{1 - \exp(-L^2 / \mu \tau V)}{1 + \frac{L}{V \mu}} \quad (2-3)$$

2.3 Detector Fabrication

Detectors refer to single crystals that have an electrode deposited on their surface. The process of fabricating standard detectors is depicted in *Figure 2.3*. The steps involved are as follows: first, the single crystals were mechanically polished using sandpaper of varying grit sizes, from 1 to 15000, to create a smooth and high-quality surface for the electrode deposition. The smoothness of the surface is verified by observing it under a microscope. Subsequently, the crystals were washed with toluene to remove any dust or organic materials from the surface. Finally, electrode metals with a thickness of up to 100 nanometers were deposited on both sides of the crystal using an E-Beam evaporator.



Figure 2.3. Schematic illustration of steps followed to fabricate MAPbBr₃ detectors.

2.4 Radiation Tests

2.4.1 X-Ray Detection

The fabricated devices were subjected to X-ray measurements in order to evaluate their X-ray sensitivity and capacity to absorb X-rays. To accomplish this, the detector devices were biased using a Keithley 2450 SMU and a medical diagnostic X-ray unit equipped with a Del Medical Anthem 32-500 generator, and a portable universal X-ray head was used to deliver the X-ray flux. In standard tests, the detector was placed 20 inches away from the X-ray source and biased between 5 V and 40 V, with the machine set to emit 50 KeV for one second. The DC current generated by the device was then measured by the SMU to determine the X-ray sensitivity. Additionally, the X-ray dose rate was measured using a universal X-ray instrument (UXI) all-purpose meter 324. *Figure 2.4* shows the experimental setup.

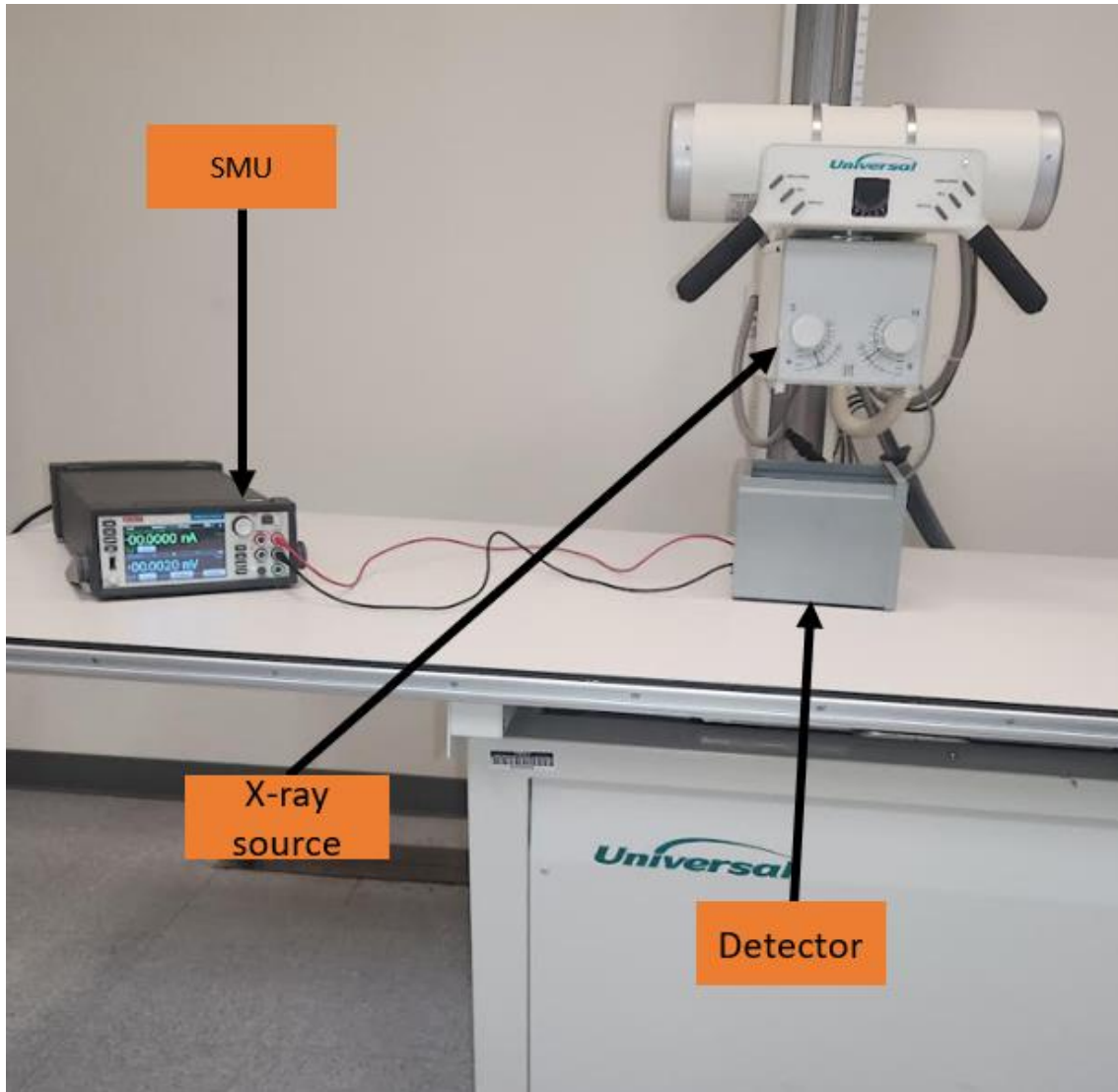


Figure 2.4. Image of the X-ray detection setup.

2.4.2 Gamma-Ray Detection

The ideal conditions for detecting gamma rays necessitate minimizing electrical noise emanating from both the detector and its surroundings. To reduce noise from the detectors, they were mounted on a custom-printed circuit board. Furthermore, a metal box as shown in *Figure 2.5* was prepared to shield against electromagnetic noise, and the box was fitted with a vacuum port to prevent surface recombination and reduce leakage current.

The importance of the electronics chain in detecting radiation-induced signals becomes particularly apparent when the number of charge carriers generated is low. Furthermore, an impedance mismatch between the electronics and the detector can lead to the failure to register the signal, hence the selection of the detector electronics chain was guided by the capacitance and noise level of the crystals. The components of the signal processing electronics chosen for the radiation test setup in gamma-ray spectroscopy are illustrated in *Figure 2.6*. In standard operation, the detector box was first evacuated to 0.1 mbar using a vacuum pump to minimize noise, and the detector was connected to a Kromek ev550 charge-sensitive preamplifier via a 6-inch BNC cable. The output of the preamplifier was then routed to an Ortec 672 amplifier, whose output was fed to a Kromek 102 multichannel analyzer (MCA). Finally, the spectrum was acquired using MultiSpect software by Kromek. Typically, the gamma source was positioned 3 centimeters above the detector, which was supplied with a bias of +200 V, with the positive terminal connected to the Cr electrode. The preamplifier gain was set at 200x, and the shaping time was set at 10 microseconds.

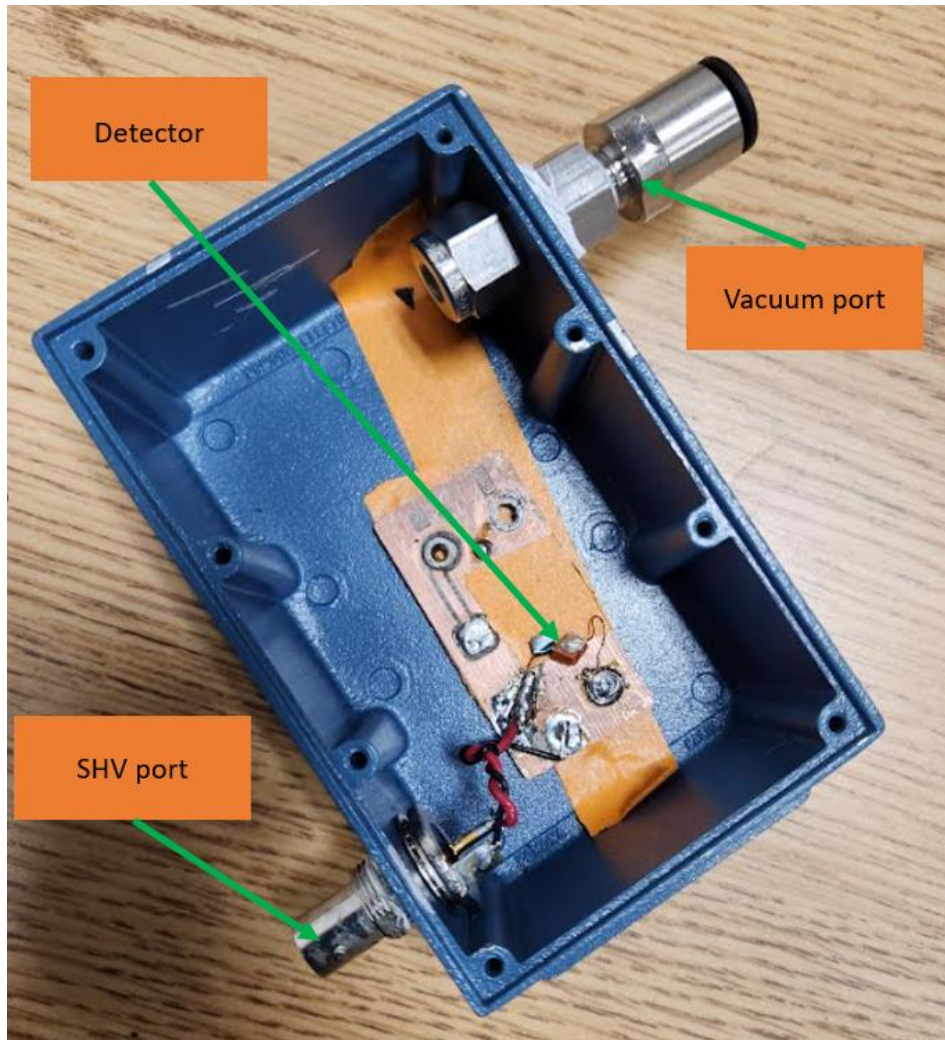


Figure 2.5. Image of the custom build detector box.

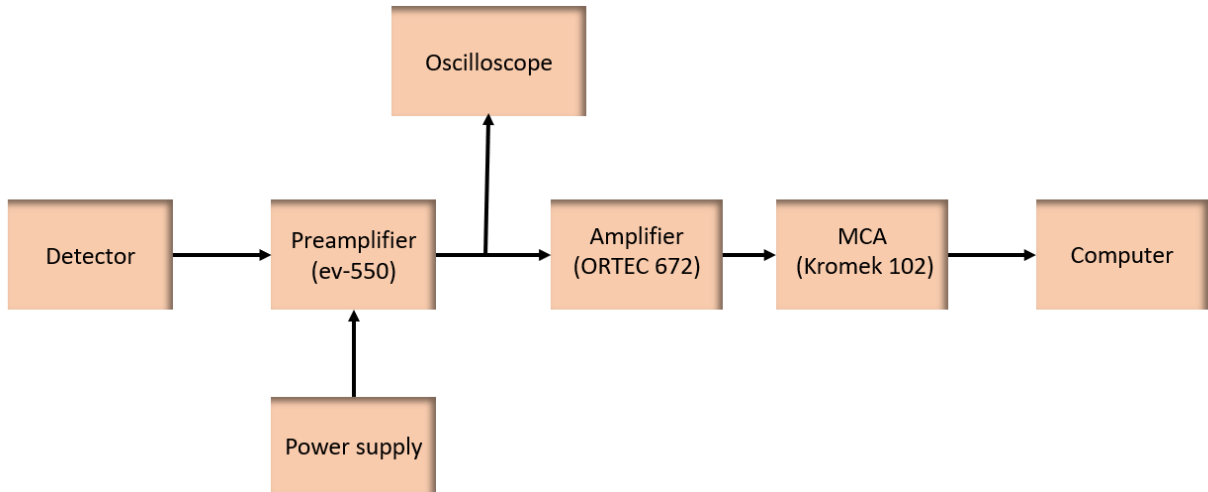


Figure 2.6. Schematic illustration of the radiation spectroscopy setup.

Chapter 3. Detection of Ionizing Radiation Using MAPbBr₃ Single Crystals Grown Through Polymer-Assisted Inverse Temperature Crystallization (PAITC) Method

3.1 Introduction

Ground zero for a good radiation detection material is a large, high-quality single crystal. Consequently, the growth of perovskite crystals with sufficient quality has attracted tremendous interest over the last decade[53]. Traditionally, radiation detectors have used crystals grown from a melt of the precursor powder[107]. These growth methods offer great control over the crystal growth process and yield high-quality crystals. However, because of the instability of the organic components of organic-inorganic hybrid perovskites at high temperatures, melt-growth methods cannot be utilized. As a result, methods explored to grow organic-inorganic hybrid perovskites have so far focused on low-temperature solution processes[108]. Despite the advantages of solution-based methods, such as increased flexibility and cost-effectiveness, the challenge of growing large and high-quality crystals using this method persists.

In solution-based crystal growth, the concentration and temperature of the solution are the main parameters that must be controlled[109]. Consequently, most of the methods developed have focused on growing high-quality crystals by efficiently controlling one or both of these parameters. Recently, several promising solution-based methods have been reported that can be categorized into four general categories: (1) inverse temperature crystallization, (2) slow cooling, (3) anti-solvent, and (4) solvent evaporation.

Inverse temperature crystallization (ITC) is a technique that exploits the inverse relationship between solubility and temperature. At low temperatures, raw perovskite powders are readily soluble in organic solvents such as butyrolactone (GBL) and N,N-dimethylformamide (DMF), but their solubility decreases with increasing temperature. In a typical ITC process, the perovskite powder is dissolved in a solvent at low temperature, and the resulting solution is placed in a heating system to gradually increase the temperature and lower the solubility equilibrium. This causes a change in the saturation state and initiates crystal nucleation, which ultimately leads to the formation of single crystals.

Slow cooling is a method that utilizes the inverse relationship between solubility and temperature. This method involves dissolving the precursor powders at high temperatures and then slowly cooling the solution to promote the nucleation and growth of single crystals.

Anti-solvent is a method that involves the gradual diffusion of organic solvents into a perovskite precursor-solvent mixture to induce solubility and concentration changes, as well as crystal formation. In a typical anti-solvent technique, a precursor powder is initially dissolved in DMF or GBL, followed by the placement of the container containing the resulting solution in an organic solvent bath, such as toluene, methanol, or ethanol. The slow diffusion of the anti-solvent into the inner container decreases the solubility of the solution, thereby promoting nucleation and crystal growth.

Solvent evaporation is the simplest technique to grow single crystals. In this method, the precursor powder is dissolved in organic solvents, such as GBL and DMF, and the resulting mixed solution is then exposed and left open at room temperature, allowing for an open exchange with the environment. This leads to the slow evaporation of the organic solvent, which in turn causes saturation of the solution and promotes nucleation and crystal growth.

Various levels of success have been attained through the implementation of the four methods[109], [110], [111]. A consistent theme that emerged from the analysis of the outcomes was that the size and quality of the crystals were influenced by the crystal growth rate and formation temperature[112]. It has been reported that the solution temperature-lowering method is effective in growing high-quality crystals because it minimizes defect inclusion due to the reduced temperature. However, this method is time-consuming and requires several weeks to grow centimeter-sized crystals. Similarly, it has been proven to be time-consuming to grow large crystals through solvent evaporation and anti-solvent methods.

However, the inverse temperature crystallization method has been reported to offer a rapid crystal growth rate owing to the high supersaturation caused by the increase in temperature. Yet, this method is faced with two main challenges[110]; first, if not controlled, the rapid supersaturation leads to many small crystals instead of one large crystal. Second, the rapid high supersaturation was shown to weaken the stability of the growth solution and cause impurity phase and defect structures. Few techniques have been developed to circumvent these challenges. Liu et al. reported MAPbBr₃ crystals of up to 25 mm in size by planting pre-prepared crystal seeds in the growth solution, which reduced the appearance of many small crystals, and seed crystals served as the only growth site [109]. The same group has also reported a slightly improved ITC, which they called the “low-temperature gradient crystallization method”[110]. In this method, the prepared seed was added to MAPbBr₃ growth solution at room temperature, the temperature was raised 2 °C/day, and single crystals up to 41 mm were grown in 20 days. The success of the method was ascribed to the small temperature gradient. While the success of such methods is impressive, similar to the solution-lowering method, they require an extended period of time. Furthermore, the utilization of seed crystals may cause impurity phases and defects. In recent times, Ma et al. [3]

have exhibited the efficacy of oxygen-containing polymer ligands in governing solution-based crystal growth processes, which do not necessitate the use of seed crystals and have yielded crystals with exceptional optoelectronic properties. However, the radiation detection capabilities of these crystals have yet to be fully explored.

3.2 Polymer-Assisted Inverse Temperature Crystallization (PAITC) Method

Building on the success of Ma et al. [108] and lessons learned from the low-temperature gradient method, a slightly improved crystal growth method that we call the PAITC method is proposed in this study. The mechanisms of such a method could be contrasted to the customary ITC method to describe their difference. As shown in *Figure 3.1*, in the regular ITC method, MAPbBr₃ precursor powder is dissolved to form a precursor solvent complex; as the temperature is gradually increased, the solubility of the precursor rapidly changes, causing a rapid formation of Pb-Br₆ nuclei sites. The uncontrolled emergence of such nuclei sites minimizes the size and quality of a single crystal that could be grown through ITC. In contrast, the PAITC method utilizes an oxygen group containing polypropylene glycol (PPG) polymer, as shown in *Figure 3.2*, PPG binds to some of the Pb²⁺ coordination sites, a gradual increase in the solution temperature will then cause the dissociation of precursor-DMF complex, and supersaturation starts to form, however, the dissociation equilibrium of Pb-PPG complex shifts slowly that rapid Pb-Br₆ nuclei site formation is effectively slowed, which in turn significantly reduces the number of nuclei sites and causes the crystal formation to happen at one or few crystallization sites [108].

This chapter discusses the characterization of MAPbBr₃ single crystals grown through the PAITC method. The performance PAITC grown crystals was compared to crystals grown through the ITC method. To investigate the effect of polymer amount on the properties of MAPbBr₃, single

crystals with varying amounts of PPG were prepared. The chemical, thermal, optical, and electrical properties of the crystals were measured and analyzed. Lastly, the chapter concludes by discussing the radiation detection performance of the prepared crystals. The detailed experimental methods are discussed in chapter two.

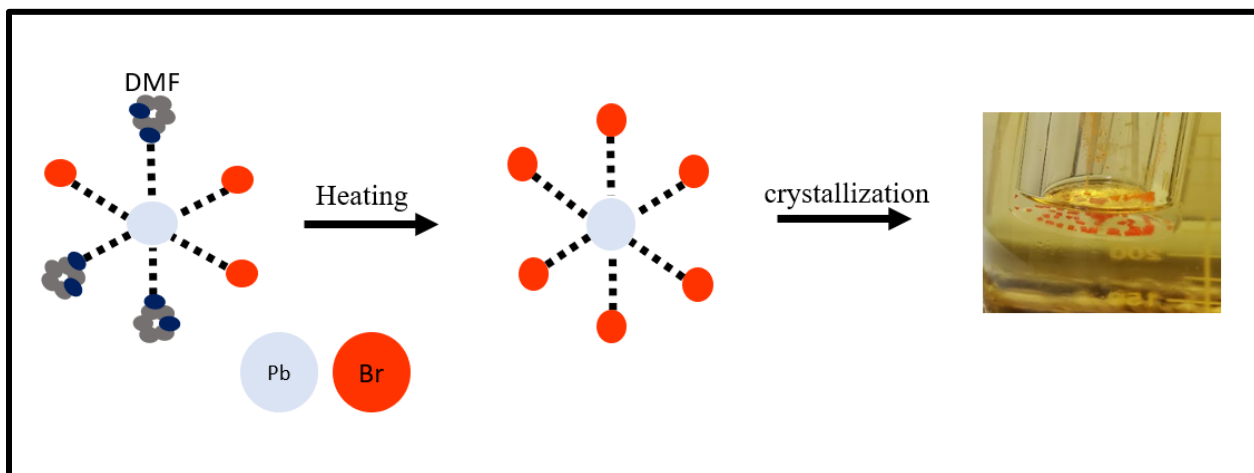


Figure 3.1. Depiction of crystal growth steps in standard inverse temperature crystallization method.

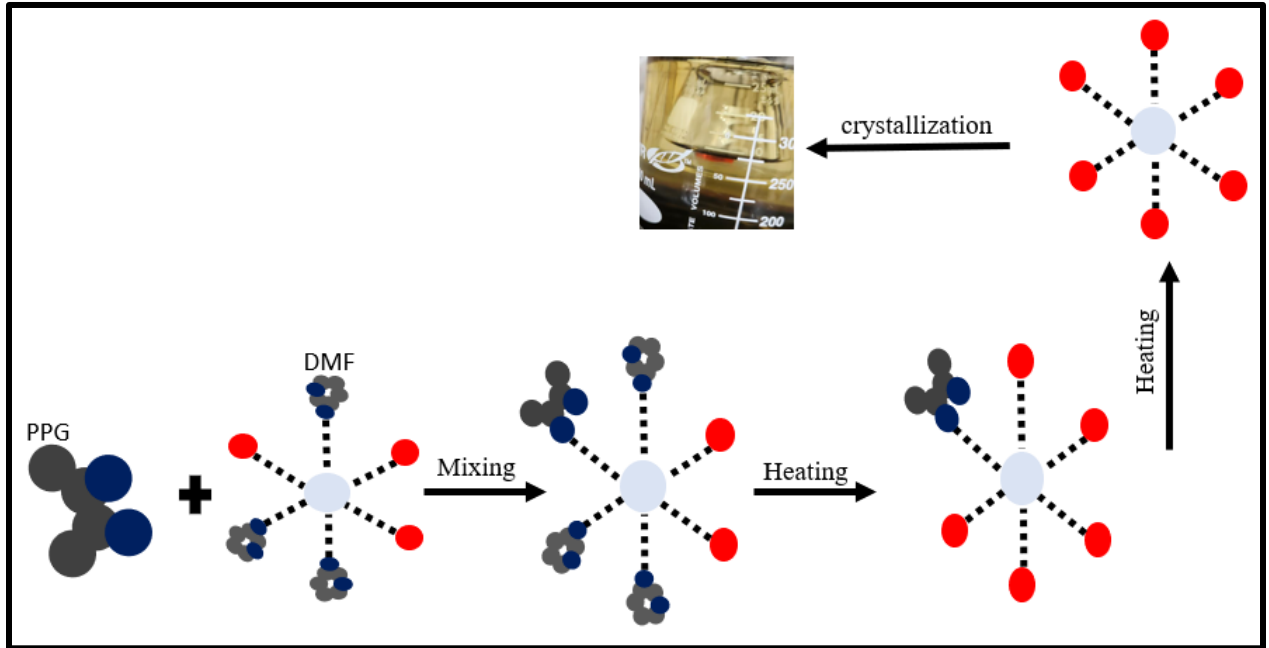


Figure 3.2. Crystal growth steps in polymer assisted inverse temperature crystallization method.

3.3 Results

High-quality MAPbBr₃ perovskite single crystals were synthesized through the utilization of a PAITC method. To optimize the quality of the single crystals obtained, a bottom-up approach was employed, which entailed the synthesis of fresh MAPbBr₃ powder followed by the growth of the crystals in a second stage. The images of the as-synthesized MAPbBr₃ powder and single crystal are shown in *Figures 3.3a* and *3.3b*. As demonstrated in *Figure 3.3c*, this method has enabled the successful growth of large, transparent, and crack-free MAPbBr₃ single crystals with a size exceeding a centimeter. While size is a critical factor for radiation detection applications, transparency and the absence of cracks are also essential. The presence of cracks can limit the utilizable volume of the crystal, thereby reducing its overall effectiveness. As shown in *Figure*

3.3d, the maximum utilizable volume of single crystals we were able to grow increased tenfold when assisted by PPG compared to the traditional method, which demonstrates the significant advantage of the polymer-assisted method.

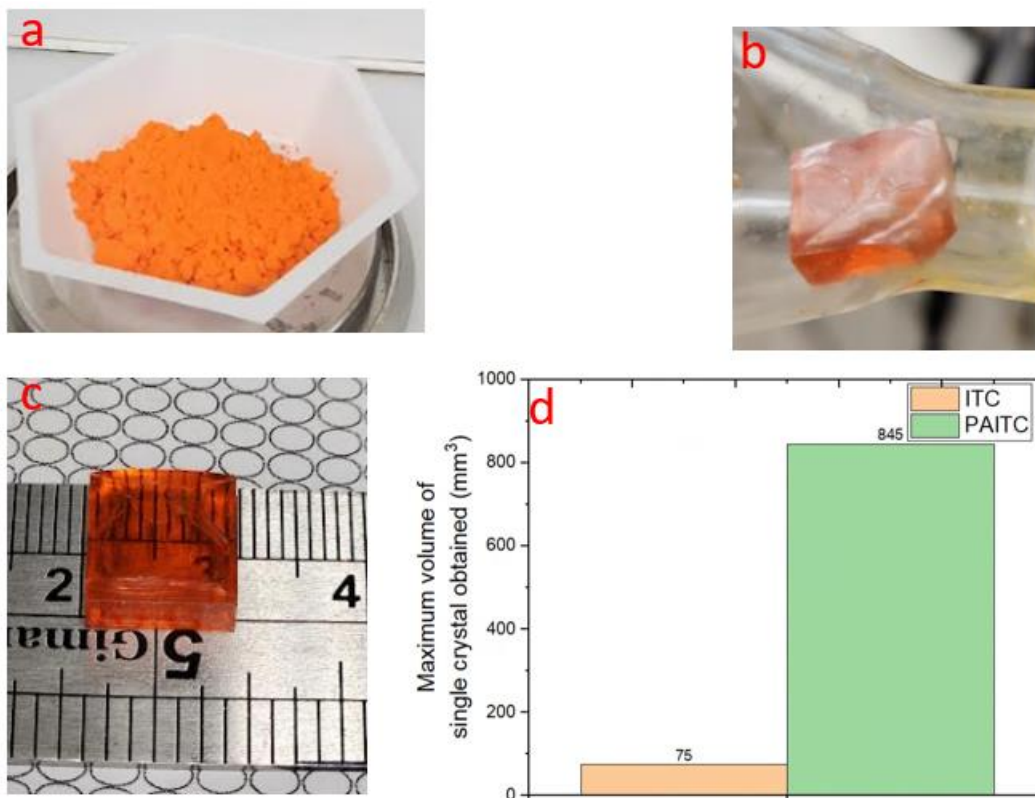


Figure 3.3. Image of the synthesized MAPbBr_3 powder(a), single crystal(b),(c) histogram plot comparing the maximum size of single crystal grown through ITC and PAITC methods(d).

3.3.1 X-ray diffractometry analysis

The crystallinity and purity of the synthesized powders and crystals were characterized utilizing X-ray diffractometry (XRD). The obtained XRD patterns showed a cubic $Pm\ 3\ m$ space group at room temperature, with a unit cell length (a) calculated as 5.93280 Å [113]. As depicted in *Figure 3.4*, the powder XRD peaks at $2\theta = 14.9, 21.1, 25.9, 29.9, 35.5, 36.8, 42.7, 45.5,$ and 48.06° were attributed to the (100), (110), (111), (200), (210), (211), (220), (300), and (310) planes of cubic MAPbBr₃, respectively. The XRD pattern of the as-grown single crystal demonstrated sharp peaks at $2\theta = 15.3, 30.5,$ and 46.2° , which were indexed to the (100), (200), and (300) faces, indicating the presence of a well-structured cubic single crystal phase [114]. Additionally, the powder and single crystal patterns exhibited no impurity peaks, which confirmed the pure crystallinity and high quality of the synthesized materials.

The thermal stability of the single crystals that were prepared was assessed using thermogravimetric analysis. The analysis was carried out between 25 and 600 °C at a heating rate of 10 °C per minute. The results, which are illustrated in *Figure 3.5* showed that the MAPbBr₃ crystals that were grown without the aid of PPG exhibited stability (mass loss less than 1%) up to 265 °C, while the crystals that were grown through the polymer-assisted method exhibited extended stability up to 320 °C. This is an improvement compared to previously reported value (268 °C) for this material [1], [6], and can be attributed to the superior quality of the crystals obtained through the polymer-assisted crystallization method. However, after 320 °C, the crystal demonstrated increased mass loss, likely due to the disintegration of the organic component MA⁺.

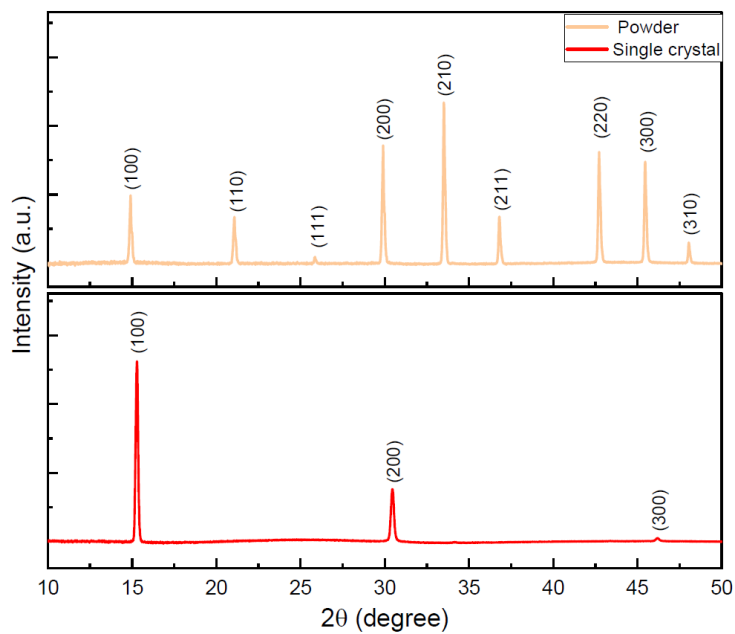


Figure 3.4. X-ray diffraction patterns of as-prepared MAPbBr_3 perovskite powder and single crystals.

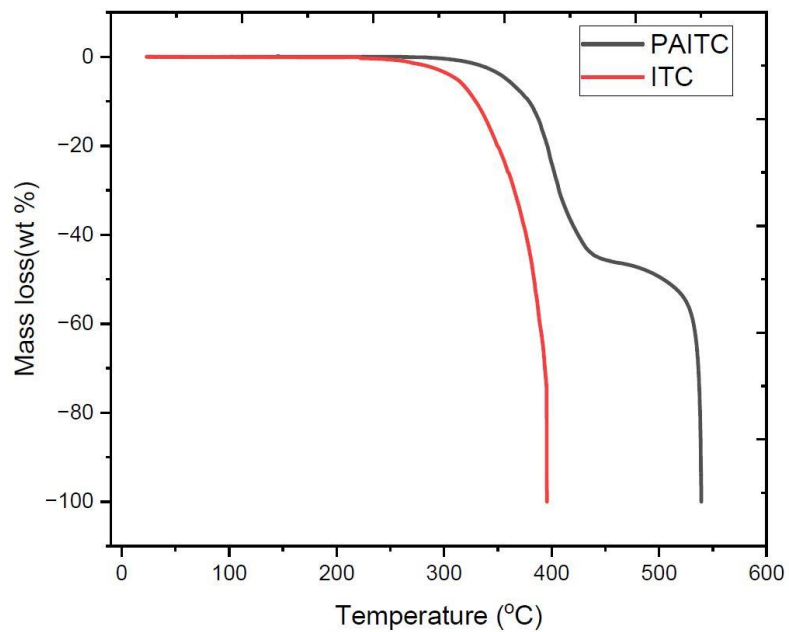


Figure 3.5. The thermogravimetric plot, loss of mass as a function of temperature change

3.3.2 Photoluminescence (PL) Study

Photoluminescence (PL) refers to the emission of light from a material following the absorption of photons. The shape and width of the PL peak provide information pertaining to the electronic structure and properties of the material. An ideal semiconductor is characterized by a sharp peak, which signifies the high purity and crystallinity of the material [115]. Conversely, a broad peak suggests a considerable distribution of energy levels, which may result from defects, impurities, or disorders in the material. *Figure 3.6a* illustrates the PL peak of MAPbBr₃ single crystals grown using the ITC and PAITC methods. The emission peak at room temperature was observed at 538 nm, which is consistent with literature[115], [116] and corresponds to a band gap of 2.30 eV. The average full width at half maximum (FWHM) of the peaks was 126 and 180 meV for crystals grown with and without polymer, respectively. The sharper peak of the crystal grown with polymer indicates the enhanced optical performance of the polymer-assisted crystal growth method [115].

The emission of photoluminescence (PL) from semiconductors is influenced by two crucial material-specific parameters: exciton-phonon scattering and exciton binding energy [117], [118]. Exciton-phonon scattering, primarily attributed to various types of defects, provides a pathway for nonradiative recombination. In contrast, higher exciton binding energy enables the formation of stable excitons that can reduce nonradiative recombination. Furthermore, the broadening of temperature-dependent photoluminescence (PL) spectra can be explained by *Equation (3-1)* [117], [119], where $\Gamma(T)$ represents the full width at half maximum (FWHM) at temperature T , Γ_0 is a temperature-independent inhomogeneous broadening term, $\Gamma_{\partial c}$ and Γ_{LO} are temperature-dependent homogeneous acoustic and optical broadening terms respectively. It should be noted that the

contribution of acoustic scattering in single crystals is negligible; therefore, it can be disregarded [119]. Consequently, the broadening of PL spectra is primarily attributed to optical phonon scattering.

$$\Gamma(T) = \Gamma_0 + \Gamma_{\partial c} + \Gamma_{LO} \quad (3-1)$$

A temperature-dependent PL study was conducted to investigate the effects of a polymer-assisted method on the optical properties of the prepared crystals. *Figure 3.6b* illustrates the FWHM of crystals grown with and without the aid of a polymer. As evident from the data, the crystal grown with the polymer exhibited a narrower FWHM across the entire temperature range compared to its counterpart. This suggests that the reduced FWHM of the crystal made through the PAITC method may be due to the reduced number of defects, which would have otherwise acted as scattering sites and caused broadening.

The normalized integrated cryogenic PL emission intensity pseudo-color map of the crystals grown without and with polymer are shown in *Figure 3.7a* and *Figure 3.7b*, respectively. Two key observations can be made from the plots. Firstly, both crystals exhibit a blue shift in their emission peak as the temperature increases, which will be further discussed in the following paragraph. Secondly, the crystal grown using the PAITC method consistently exhibited higher emission energy than ITC-grown single crystals throughout the entire cryogenic test range, which can be attributed to the higher exciton binding energy of the PAITC crystal [115]. The higher exciton energy is advantageous for reducing nonradiative recombination and lends superior optical performance to the PAITC crystals.

Figure 3.7c reveals the evolution of the PL emission peaks of the PAITC crystals. Both crystals have shown a continuous redshift, counterintuitive to traditional semiconductors that generally show a blue shift with decreasing temperature [119], [120], [121]. In principle, the band gap of a semiconductor is a consequence of electron-phonon interaction, and thermal lattice expansion [119], [120], [122], [123]. Decrease in temperature reduces electron-phonon interaction, thereby causing band gap expansion. the contribution of lattice expansion in semiconductors is reported to be weak, which is why conventional semiconductors generally show a blue shift with decreasing temperature [117]. In contrast, our crystals showed a blue shift with increasing temperature, which is occasionally observed in other semiconductors [121], [124], [125]. Several groups have attempted to explain this phenomenon through either electron-phonon interaction, such as the conduction band maximum and valence band maximum method, or through lattice expansion [119], [121], [122], [124], [125]. However, a consensus has not been reached on the subject, and further study is needed to identify and understand the origin of the blue shift.

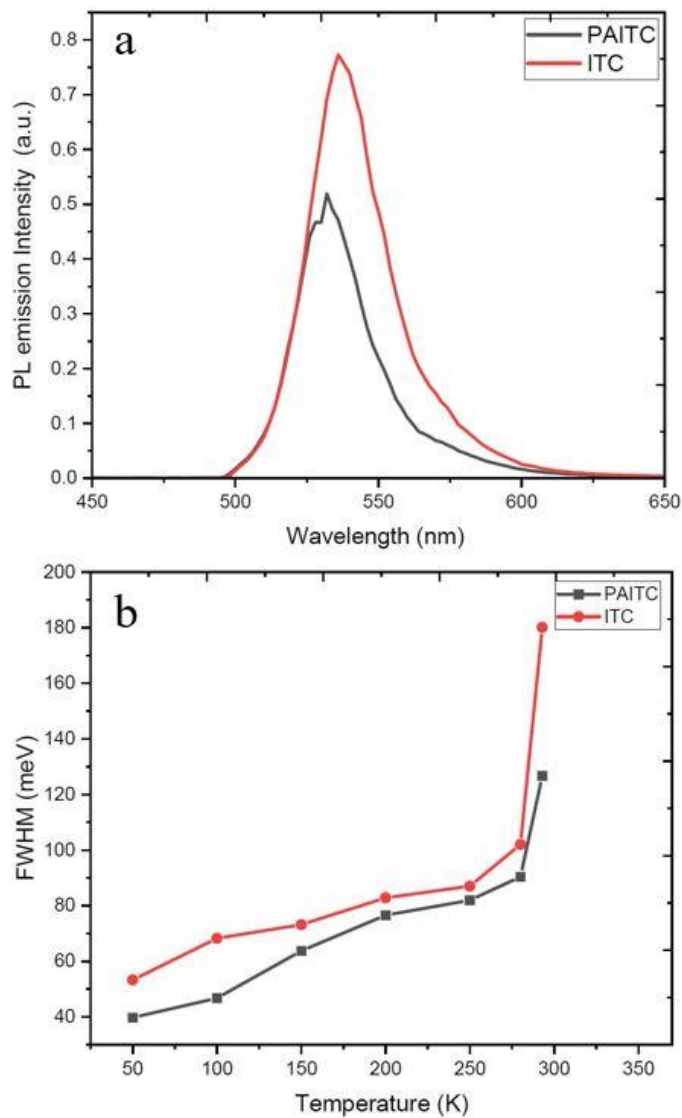


Figure 3.6. comparison of room temperature PL emission peak of MAPbBr₃ single crystal grown through PAITC and ITC methods (a), Comparison of emission peak FWHM under cryogenic PL tests (b)

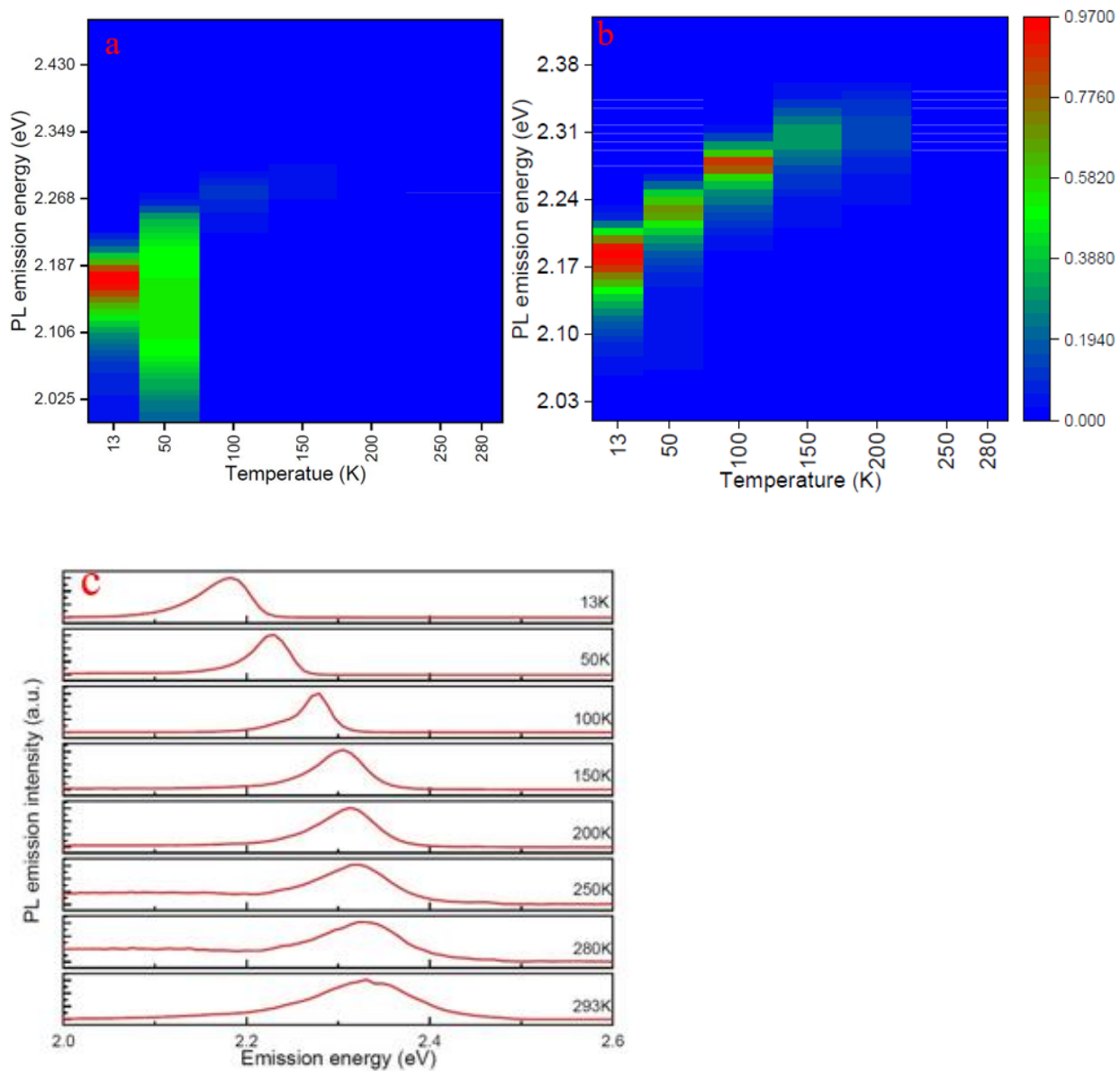


Figure 3.7. Pseudo color heatmap of temperature-dependent PL emission intensity of MAPbBr₃ single crystals, grown through ITC (a), grown with 0.1g/ml PPG PAITC (b) Temperature-dependent MAPbBr₃ PL emission peak position shift observed under cryogenic PL study (c).

3.3.3 I-V Characterization

In order to investigate the electrical properties of the crystals prepared in this study, measurements of DC current were taken under dark conditions. High-quality crystals among the as-grown crystals were carefully selected and prepared, with both faces being polished mechanically, and lastly, 100 nm Ni and Cr electrode contacts deposited on either side. The devices were then placed under a dark environment, and the current response was measured as the bias voltage was swept from 0 to 20V. As shown in *Figure 3.8*, the I-V curves of the crystals prepared with and without varying amounts of PPG showed both linear and non-linear regions. The linear region of the I-V curves obeyed Ohm's law, and the law was used to calculate the resistivity of the crystals. As summarized in *Table 3.1*, the resistivity of the crystals prepared through the polymer-assisted method was higher than that of those prepared without the use of the polymer. However, an increase in the amount of polymer did not show a direct correlation with an increase in the resistivity of the crystals.

The emergence of the non-linear region of the I-V curve is linked to changes in the number of charge-trapping sites in the bulk of the semiconductor [44]. In the linear region, the trap sites are not entirely filled; as a result, an increase in bias voltage leads to a proportional increase in the dark current. Further increases in bias cause the trap sites to be completely filled with electrons, causing the dark current to rise non-linearly. This occurs because charge carriers that would otherwise have been trapped can now flow through the circuit, resulting in a large current. The onset of this non-linear rise is referred to as the voltage at trap-filled limit (V_{TFL}) and is used to determine the trap density of crystals according to the *Equation. 3-2*. Here, ϵ is the material's dielectric constant, ϵ_0 is the vacuum permittivity, e is the charge of an electron, and d is the thickness of the crystal [17]. In order to determine the trap densities in the crystals, the relative

dielectric constants of the MAPbBr₃ crystals were estimated through capacitance-frequency measurements. Capacitance-frequency curves *Figure 3.9* were obtained using an impedance capacitance resistance (LCR) meter, and the relative dielectric constants were calculated from the measured capacitance using the *Equation. 3-3*, where C is capacitance, and A is the active electrode area of the devices.

$$V_{TFL} = \frac{en_{trap}d^2}{2\epsilon\epsilon_0} \quad (3-2)$$

$$\epsilon = \frac{Cd}{\epsilon_0 A} \quad (3-3)$$

The calculated trap density of MAPbBr₃ single crystals is summarized in *Table. 3.1*. As demonstrated in the table, the greatest trap density was observed in crystals grown without polymer, while the crystal prepared with the most amount of PPG showed the least amount of trap sites. Through the process of growing multiple rounds of crystals for this research, it was observed that the time it takes to grow the crystals was directly related to the amount of PPG utilized, the quickest being when the smallest amount was used and the slowest being when the most amount was used. Meanwhile, the trap density results demonstrated that the crystal with the slower growth rate had better quality, confirming our theory that the action of PPG polymer by regulating the crystal growth speed results in better quality crystals. The best observed trap density $1 \times 10^9 \text{ cm}^{-3}$ is better than similar class of materials [126] and significantly lower than ($>10^{10} \text{ cm}^{-3}$) that of the well-known semiconductor CdTe [127].

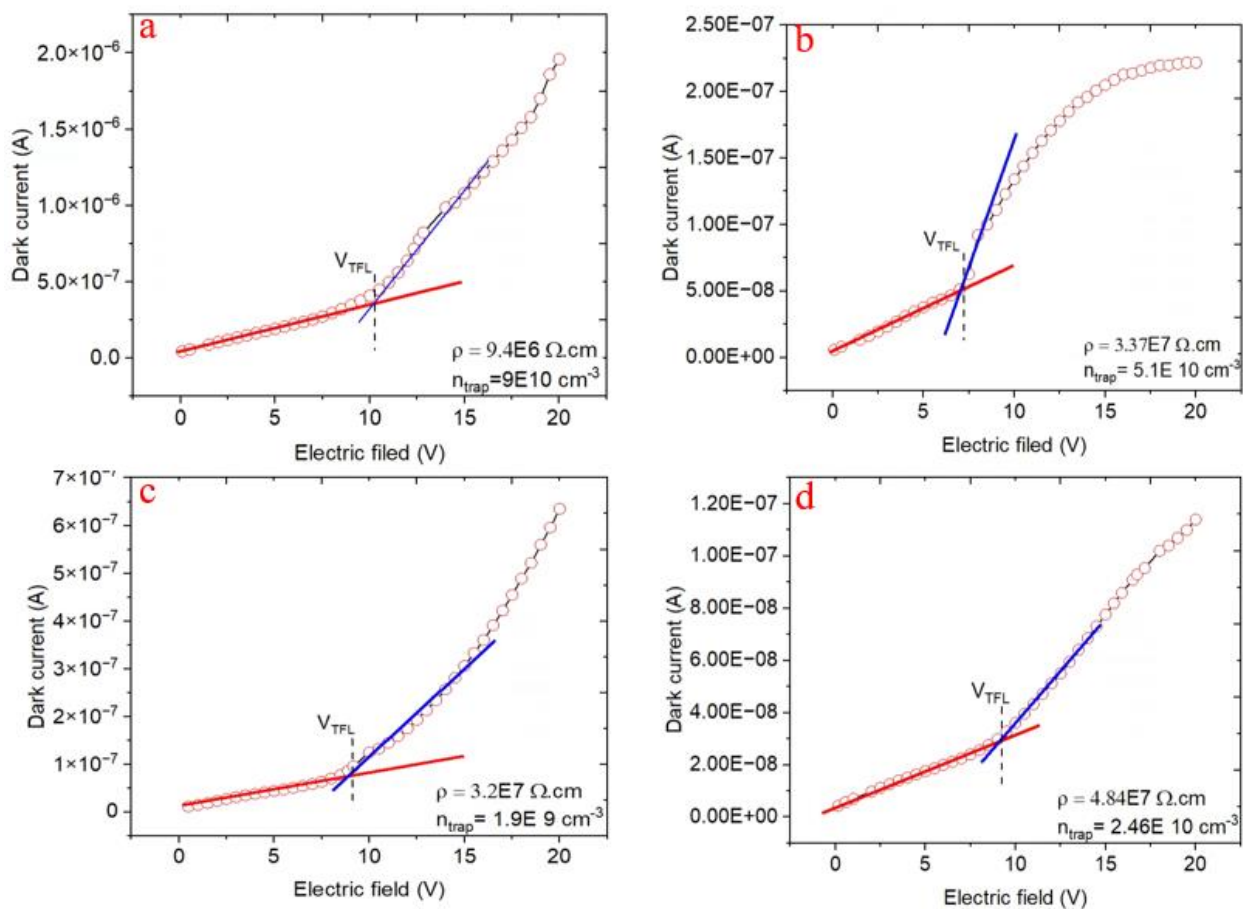


Figure 3.8. Current-voltage (I - V) curve of MAPbBr_3 crystals grown with ITC (a), PAITC methods with PPG amount of 0.01 g/ml (b), 0.02 g/ml (c), and 0.03 g/ml (d).

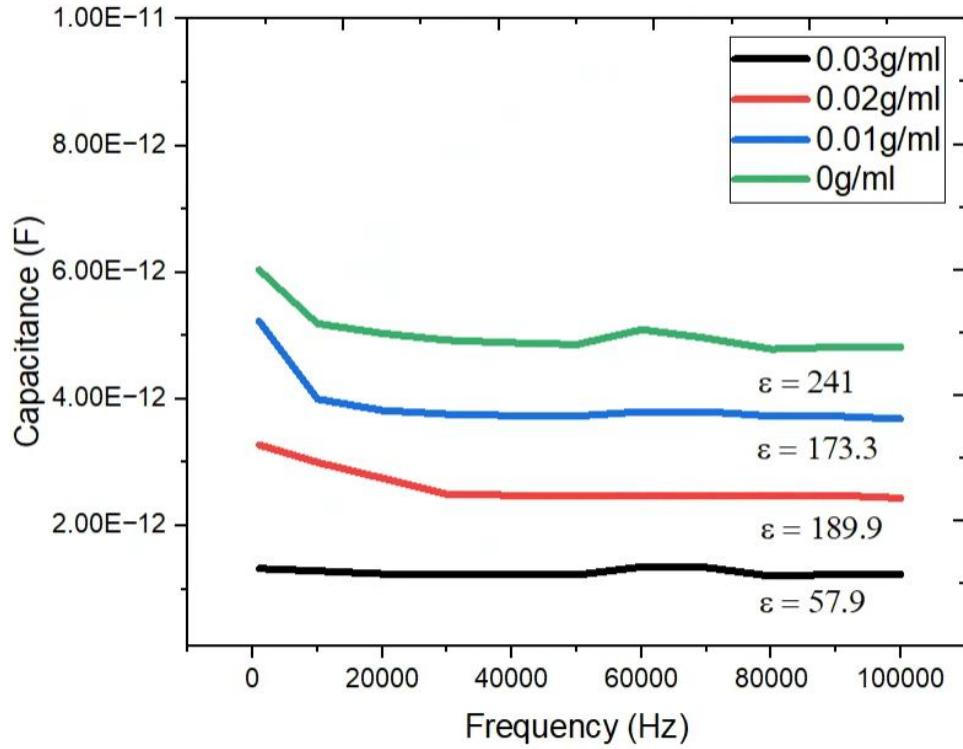


Figure 3.9. Capacitance-frequency curves of MAPbBr₃ crystals grown with ITC, (0 g/ml), and PAITC methods with PPG amount of 0.01 g/ml, 0.02 g/ml, and 0.03 g/ml.

Table 3.1. Summary of electrical resistivity and trap density of MAPbBr₃ single crystals.

PPG amount utilized to grow the crystal (mg/l)	Resistivity ($\Omega\cdot\text{cm}$)	Trap density (cm^{-3})
0	9.4×10^6	9×10^{10}
0.01	3.37×10^7	5.1×10^{10}
0.02	4.8×10^7	2.46×10^{10}
0.03	3.2×10^7	1.9×10^9

The characterization of the mobility lifetime product ($\mu\tau$) of the prepared crystals was accomplished using the relationship between photocurrent and bias voltage according to the modified Hecht Equation [128], shown in *Equation. 3-4*, where μ is the mobility of charge carriers, τ is the life-time of charge carriers, I_0 is the saturated current, and L and V are the device thickness and bias voltage, respectively. The MAPbBr₃ devices photocurrent response was measured by exposing the crystals to a 365 nm, 12 W, blue LED light, as shown in the inset of *Figure 3.10*, and by sweeping an electric field from 0 V to 20 V using a Keithley source measuring unit 2450. *Figure 3.10* shows the plot of the electric field against the measured photocurrent; the calculated $\mu\tau$ values from the fitting of the modified Hecht equation are 4.1×10^{-2} , 1.04×10^{-2} , 1.16×10^{-2} , and $4.63 \times 10^{-3} \text{ cm}^2\text{V}^{-1}$ for crystals grown with 0.03, 0.02, 0.01, and 0 g/ml of PPG, respectively. The results indicate that crystals prepared through the PAITC method have improved $\mu\tau$ values compared to those prepared without polymer assistance. The trap density analysis confirms that crystals prepared through the PAITC route have a lower trap density, which may be the reason for the improvement in the charge mobility of the crystals due to the reduced number of obstacles that charge carriers will face while drifting toward the electrode.

$$I = \frac{I_0 \mu \tau V}{L^2} \frac{1 - \exp(-L^2 / \mu \tau V)}{1 + \frac{L}{V \mu}} \quad (3-4)$$

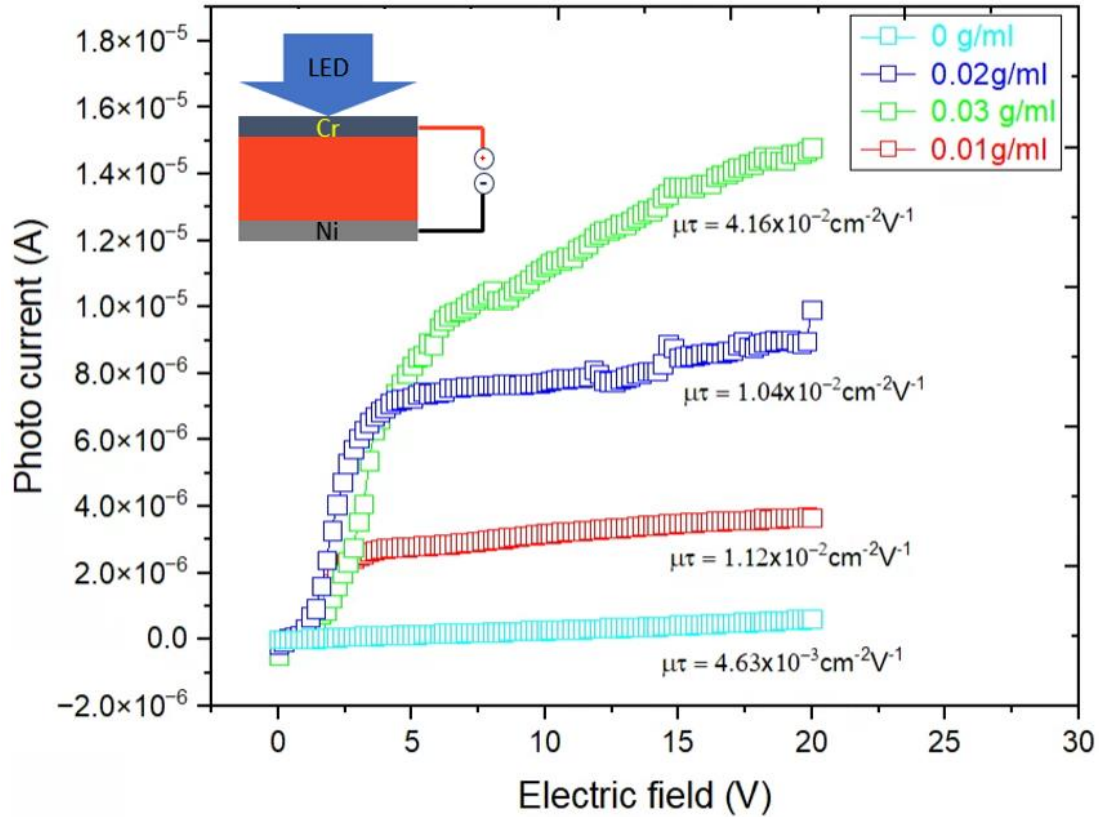


Figure 3.10. Current-voltage (I - V) curve of MAPbBr_3 crystals grown with ITC (a), PAITC methods with PPG amount of 0.01 g/ml (b), 0.02 g/ml (c), and 0.03 g/ml (d).

3.3. 4. X-Ray Detection Using MAPbBr_3 Single Crystals Grown with PAITC Method.

In conventional digital X-ray imaging techniques, the imaging process involves positioning a subject between an X-ray source and a detector, and then directly measuring the direct current (DC) produced by the pixels of the detector [128]. The intensity of the DC current is directly proportional to the intensity of the radiation received by the various areas of the detector. The amount of radiation received by the pixels of the detector is also influenced by the density of the material in front of them. Areas with denser material in front of them receive less radiation, while those with less dense material receive more. Consequently, the contrast of the intensity of the

measured radiation can be used to form the X-ray image. A critical aspect of the procedure is the detector material's sensitivity to X-rays. Therefore, in this work, the X-ray sensitivity of the MAPbBr₃ single crystals prepared was evaluated to determine their suitability for X-ray detection.

In order to assess the sensitivity of MAPbBr₃ devices, the on and off current responses of the devices were measured under various electric fields at an X-ray dose rate of 69.1 μGyair s⁻¹. The net current, which is the difference between on and off current, was plotted in *Figure 3.11*. The results indicate that crystals fabricated using the PAITC method exhibited higher current responses, which could be due to the increased charge collection efficiency afforded by their improved μτ values.

The sensitivity of an X-ray detector is expressed in *Equation 3-5* [129], where ΔI denotes the net current, D is the X-ray dose rate, and A represents the active area of the detector (2 mm×2 mm). The sensitivity of the device against the electric bias field is plotted as shown in *Figure 3.12*. Similar to the current response, the crystals produced through the PAITC method exhibited superior sensitivity. The sensitivity of the devices fabricated in this study at a bias of 40 V is compared against the best reported values for new materials and currently available commercial detectors in *Table 3.2*. As depicted in the table, the sensitivity of MAPbBr₃ devices produced in this work is 43.5 times higher than the commercially available α-Se detectors, and comparable to the best in the class sensitivity of Si integrated MAPbBr₃ devices.

$$S = \frac{\Delta I}{DA} \quad (3-5)$$

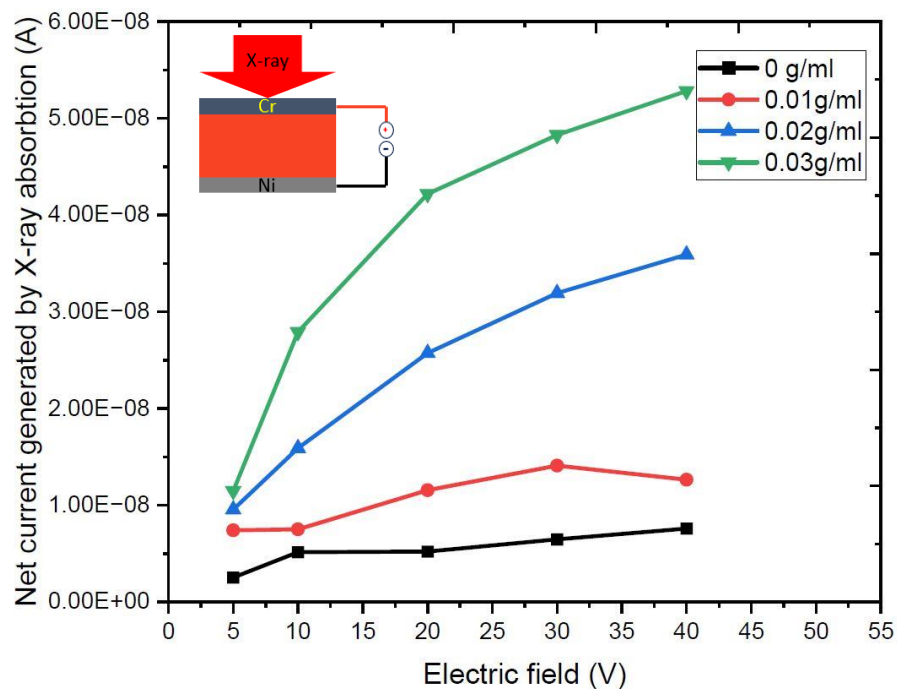


Figure 3.11. Net X-ray photo current-voltage (I - V) curve of MAPbBr_3 crystals grown with ITC, and PAITC methods with PPG amount of 0.01 g/ml, 0.02 g/ml, and 0.03 g/ml.

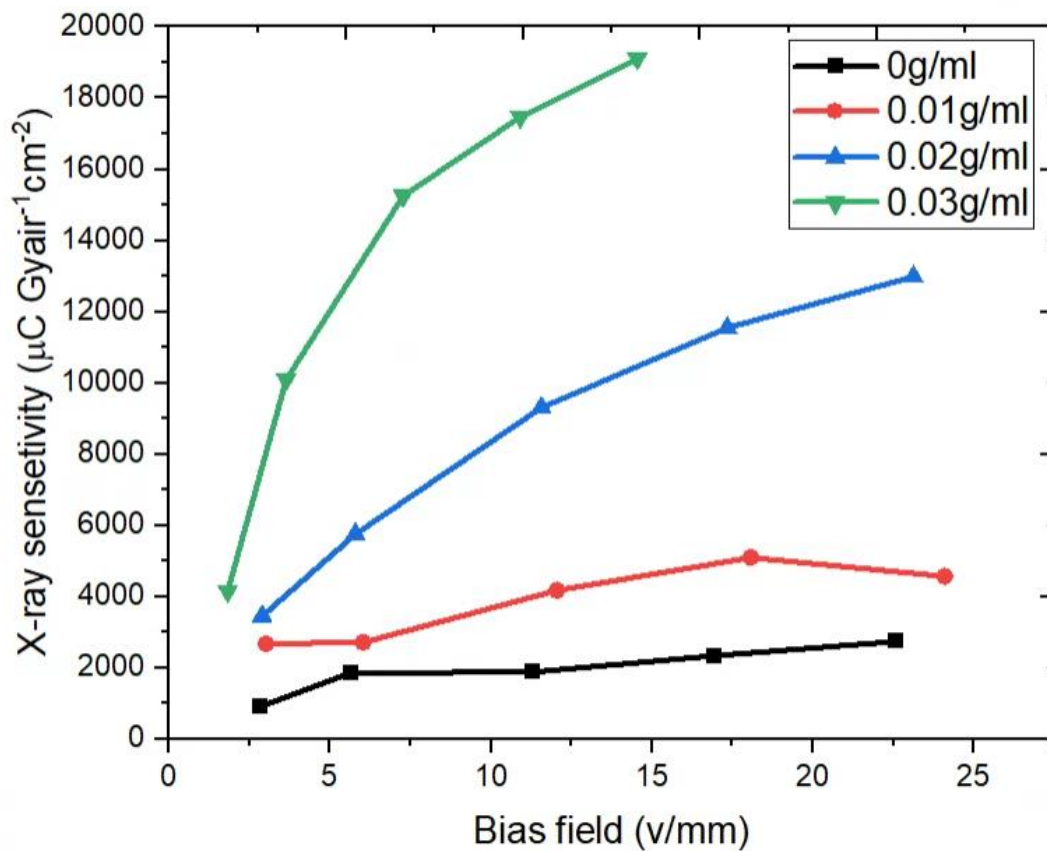


Figure 3.12. X-ray sensitivity of MAPbBr₃ crystals grown with ITC, and PAITC methods with PPG amount of 0.01 g/ml, 0.02 g/ml, and 0.03 g/ml.

Table 3.2. Summary of selected representative X-ray sensitivity of new and commercially available detector materials.

Material	X-ray sensitivity ($\mu\text{C Gyair cm}^{-2}$)	Applied bias (V/mm)	Reference
MAPbBr ₃ (0.03g/ml PPG)	19140	14	This work
MAPbBr ₃ (0.02g/ml PPG)	12988	14	This work
MAPbBr ₃ (0.02g/ml PPG)	4572	14	This work
MAPbBr ₃ (0.0g/ml PPG)	2745	14	This work
MAPbBr ₃	2552	4.5	[129]
Cs ₃ Bi ₂ I ₉	1652	50	[128]
CsPbBr ₃	619	45	[129]
Si-integrated MAPbBr ₃	21000	7	[130]
α -Se	440	15000	[128]

3.4 Conclusion

In conclusion, the results demonstrate that MAPbBr₃ single crystals can be successfully grown using the PAITC method. This method has proven to be effective in improving the quality, size, and growth speed of the crystals by reducing nucleation sites and regulating the nucleation rate. The method has resulted in MAPbBr₃ single crystals with low trap site density and improved performance. The crystals were characterized for purity, thermal stability, optical, and electrical properties, and it was found that those grown using the PAITC method exhibited superior properties compared to those grown without the aid of the polymer. The X-ray detection performance of the crystals was evaluated and the best sensitivity reported in this study is higher than previously reported values for the same class of material and is significantly better than currently commercially available X-ray detection materials. Furthermore, the simplicity of growing MAPbBr₃ crystals and their low cost make them an attractive option. Overall, it can be concluded that MAPbBr₃ has excellent potential as a material for detecting ionizing radiation.

Chapter 4. Radiation Detection Using Cl-doped MAPbBr₃ Single Crystals Grown Through the Polymer-Assisted Inverse Temperature Crystallization Method.

4.1 Introduction

Gamma spectroscopy, which measures the energy of ionizing radiation, is a crucial tool for identifying radioactive nuclides [107]. Unlike the direct current mode used for intensity measurements such as X-ray imaging, gamma-spectroscopy requires the detector to operate in the pulse mode [107], [131], and often, this occurs in a very low radiation field, which requires the detector to be ultra-sensitive to small changes. Despite this, the detector is expected to perform the event-by-event analysis to accurately generate the gamma energy spectrum. As a result, achieving the objective of gamma spectroscopy with pure MAPbBr₃ grown with the PAITC method requires further work to meet the strict requirement imposed by pulse mode operation.

The stringent requirements of gamma-spectroscopy applications necessitate the use of large-volume and high-quality crystals to ensure the interception and interaction of radiation with the detector material [78]. Additionally, a large charge carrier mobility (μ) lifetime (τ) product is necessary to efficiently collect charge carriers created by the radiation interaction. Lastly, a detector with low trap density and high resistance is required to minimize charge trapping and low noise operation, which could severely impact the single-event analysis mode [78].

The influence of noise and low resistivity on the pulse mode of operation can be understood by examining their impact on relevant performance parameters, as demonstrated by *Equations 4-1 to 4-3*. The charge collection efficiency (CCE) measures the detector's ability to convert generated carriers into a signal, while the charge drift length (λ) determines the maximum distance that carriers can travel before being lost to recombination. Finally, the drift velocity (v_d) determines how quickly carriers can reach the collection electrodes. As shown in the equations, all three parameters are directly related to the material's mobility properties and the externally applied electric field (V). However, the mobility properties of the material cannot be controlled operationally. Therefore, experts often attempt to optimize detector performance by applying high electric fields [132]. However, the use of high electric fields is a double-edged sword, as it increases charge collection as well as detector noise and can mask the signal with noise. Therefore, a resistivity in excess of $10^9 \Omega\cdot\text{cm}$ is required to take advantage of the benefit of applying high electric field [44].

$$CCE = \frac{Q}{Q_o} = \frac{\mu_e \tau_e V}{d^2} \left[1 - e^{-\left(\frac{d^2}{\mu_e \tau_e V}\right)} \right] + \frac{\mu_h \tau_h V}{d^2} \quad (4-1)$$

$$\lambda = \mu \tau V \quad (4-2)$$

$$v_d = \mu V \quad (4-3)$$

The low resistivity and high dark current in MAPbBr₃ are reportedly attributed to its high density of charge carriers [44], [92]. One feasible method of decreasing the charge carrier density is to increase the material's band gap. As demonstrated in *Figure 4.1*, by increasing the band gap of MAPbBr₃ by 13% and 43%, for instance, the intrinsic charge carrier concentration at room temperature would decrease by three and six orders of magnitude, respectively. Fortunately, the excellent chemical tunability of MAPbX₃ (X = Cl, Br, I) halide perovskites allow for simple manipulation of the band gap. Research has shown that the band gap of MAPbX₃ is influenced by two key factors of the halide variant [133]. Firstly, the band gap is inversely proportional to the atomic size of the halide. Chloride, the smallest halide, has the widest band gap (3.1 eV), while iodide, the largest halide, has the narrowest band gap (1.54 eV). Bromide is in between (2.3 eV) [134], [135], [136]. Secondly, the band gap of the hybrid perovskite is positively correlated with the valence band composition of the halide component. For example, the 3p composition of chloride requires a higher ionization potential than the 4p composition associated with bromide [5], [6]. Therefore, it is theorized that partial substitution of bromide with chloride in MAPbBr₃ could lead to a material with lower carrier density and a slightly wider bandgap, resulting in higher resistivity and lower dark current.

As previously discussed, the utilization of the PAITC method has resulted in the successful growth of large and high-quality crystals with significantly improved $\mu\tau$ and trap density properties. Nonetheless, spectroscopy with pure MAPbBr₃ single could not be achieved due to the very high noise associated with their low resistivity. This chapter discusses the attempt made to address the resistivity and noise challenges associated with MAPbBr₃. The chapter details the synthesis of MAPbBr₃ single crystals with varying levels of Cl-doping, utilizing the PAITC method. The chemical, optical, and electrical properties of

the grown crystals were analyzed using XRD, EDS, room temperature and cryogenic PL, and I-V characterizations. Lastly, the chapter discusses the gamma-ray, X-ray , detection experiment results of the Cl-doped MAPbBr₃ single crystals.

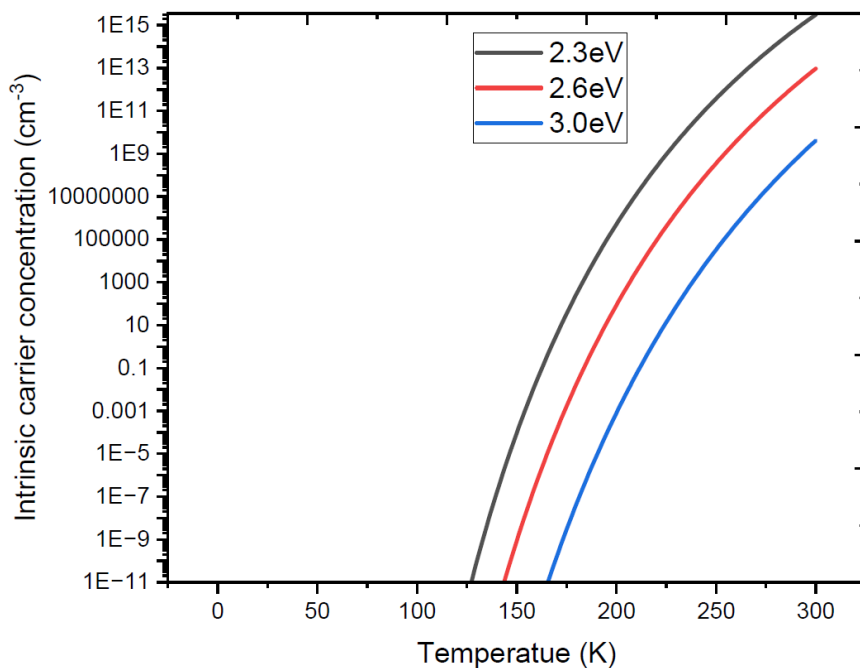


Figure 4.1. Plot of temperature and intrinsic carrier concentration, plot shows intrinsic charged carrier concentration decreases because of band gap widening.

4.2 Results

4.2.1 XRD

MAPbBr₃ and MAPbCl₃ powders were synthesized as a precursor to grow pure and Cl-doped MAPbBr₃ single crystals. The crystallinity and purity of the synthesized materials were characterized using X-ray diffractometry (XRD). The XRD patterns of the MAPbBr₃ and MAPbCl₃ crystals, *Figure 4.2a*, showed that they both have a cubic structure, with a unit cell length of 5.93280 Å and 5.68546 Å, respectively [113], [137]. The diffraction peaks of the MAPbBr₃ at $2\theta = 14.9, 21.1, 25.9, 29.9, 35.5, 36.8, 42.7, 45.5,$ and 48.06° were attributed to the (100), (110), (111), (200), (210), (211), (220), (300), and (310) planes of the cubic structure, while the MAPbCl₃ peaks at $2\theta = 14.6, 19.6, 25.4, 29.4, 34.1, 38.0, 41.6,$ and 45.4° were attributed to the (100), (110), (111), (200), (210), (211), (220), and (221) planes of the cubic structure [137]. The XRD pattern of the as-grown MAPbBr₃ single crystal demonstrated sharp peaks at $2\theta = 15.3, 30.5,$ and 46.2° [137], which were indexed to the (100), (200), and (300) faces, indicating the presence of a well-structured cubic single crystal phase. No impurity peaks were observed. As confirmed by the similarity of the XRD patterns of the pure MAPbBr₃ and Cl-doped MAPbBr₃ showed in *Figure 4.2b*, Cl doping did not change the phase of the single crystal [138]. The Cl-doped crystal showed higher peak intensity, which may be due to improved crystal quality [138]. As shown in *Figure 4.2c*, the Cl-doped crystal pattern was slightly shifted to the left, which is due to the inclusion of Cl[139]. Lastly, both powder and single crystal patterns exhibited no impurity peaks, which confirmed the pure crystallinity and high quality of the synthesized materials.

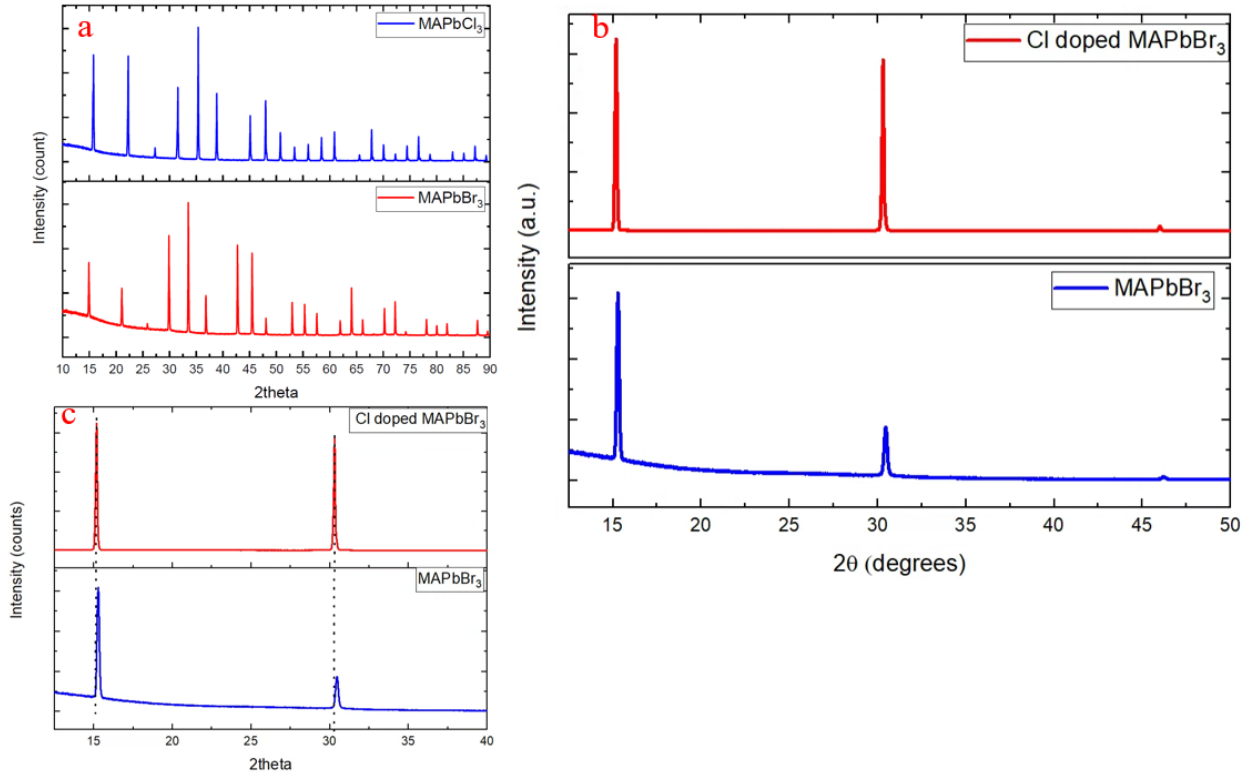


Figure 4.2. X-ray diffraction patterns of the as-prepared precursor perovskite powders (a), MAPbBr₃ single crystals with and without Cl doping (b), closeup view of the 100face peak of the as grown crystals (c).

4.2.2 EDS

MAPbBr₃ single crystals with 1% - 4% Cl doping were prepared to investigate the effect of Cl doping on the optical and electrical properties of the material. Energy Dispersive X-ray Spectroscopy (EDS) study was conducted to confirm the presence and relative increase in Cl content resulting from doping, EDS elemental mapping technique was employed to generate the images displayed in *Figure 4.3* which correspond to the Cl doping content of 1%, 2%, 3%, and 4%, respectively. As depicted in the images and *Table 4.1.*, Cl was detected in all the doped single crystals, thereby confirming its presence. However, EDS is incapable of detecting small atoms, such as hydrogen, which is present in MAPbBr₃ (CH₃NH₃PbBr₃); therefore, a 100% mass ratio could not be calculated. Nonetheless, EDS is capable of accurately determining Cl and Br amounts, and thus the ratio of Cl to the sum of Cl and Br atoms was calculated to assess the increase in Cl content of the crystals due to the increase in MAPbCl₃ in the precursor. *Figure 4.4* shows the calculated Cl/(Cl+Br) ratio, which indicates that the concentration of Cl changed linearly with the increase in MAPbCl₃, confirming the success of the method used to grow MAPbBr₃ single crystals with varying amounts of Cl doping.

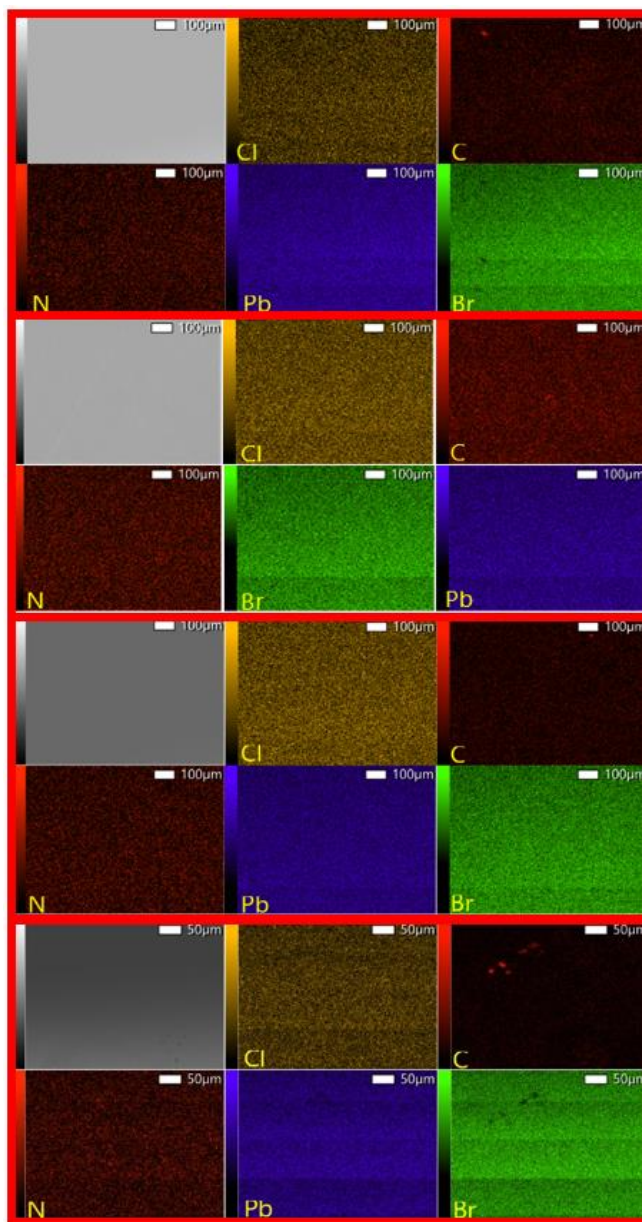


Figure 4.3. EDS elemental map of Cl-doped MAPbBr₃ single crystals, 1%, 2%, 3% and 4% Cl doped from top to bottom, respectively.

Table 4.1. Summary of EDS measured elemental atomic percentage of MAPbBr₃ single crystals, prepared with 1% - 4% substitution of MAPbBr₃ with MAPbCl₃.

Cl doping amount (%)	C	N	Pb	Br	Cl	Total
1	42.75	13.46	10.25	33.27	0.27	100
2	40.74	13.61	10.45	34.53	0.67	100
3	40.24	13.56	10.63	34.56	1.01	100
4	40.68	14.6	10.34	33.17	1.21	100

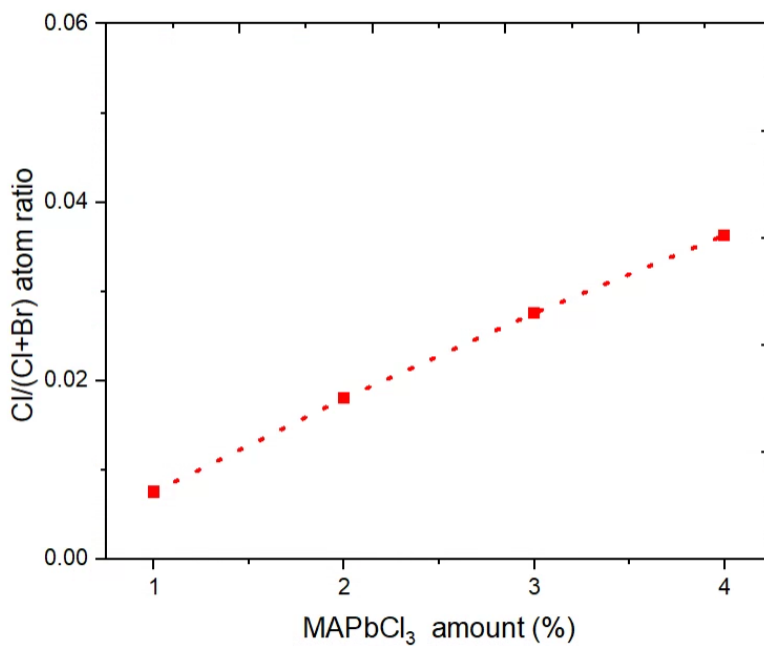


Figure 4.4. Cl to Br atom ratio of Cl-doped MAPbBr₃ single crystals, prepared with 1% - 4% substitution of MAPbBr₃ with MAPbCl₃.

4.2.3 Photoluminescence (PL) Study

Figure 4.5a presents the PL spectra of MAPbBr₃ single crystals grown with varying levels of chlorine substitution for bromine. The emission peak for pure MAPbBr₃ at room temperature is observed at 538 nm, which is consistent with literature [4], [5] and corresponds to a band gap of 2.30 eV. Additionally, the plot reveals that the emission peaks of the crystal are progressively shifted towards shorter wavelengths; it decreased from 538 nm for pure MAPbBr₃ to 526 nm when 4% Cl doping is used, which is consistent with an increase in energy band gap width.

The calculation of the band gap in single crystals of MAPbBr₃ can be performed using *Equation 4-4* [140], where E_g is the band gap in eV, and λ is the main emission peak in nm. As shown in *Figure 4.5b*, the calculated E_g values for MAPbBr₃ single crystals with varying amounts of Cl doping are plotted. The figure indicates that the band gap increased from 2.30 eV to 2.35 eV with 4% Cl doping. This expansion of the band gap can be attributed to two main reasons. Firstly, the band gap of hybrid perovskite is positively correlated with the amount of Cl [133], [141] as the valence band composition of Cl is 3p which requires a higher ionization potential than the 4p composition associated with bromine [133], [141]. Hence, an increase in Cl amount leads to an increase in the band gap due to the increased ionization energy requirement. Secondly, the size of the cations also affects the band gap of hybrid perovskites by impacting the crystal lattice structure [142], [143]. In the case of Br substitution with Cl atom, it causes contraction of the lattice, thereby causing a widening of the band gap.

$$E_g = \frac{1240}{\lambda} \quad (4-4)$$

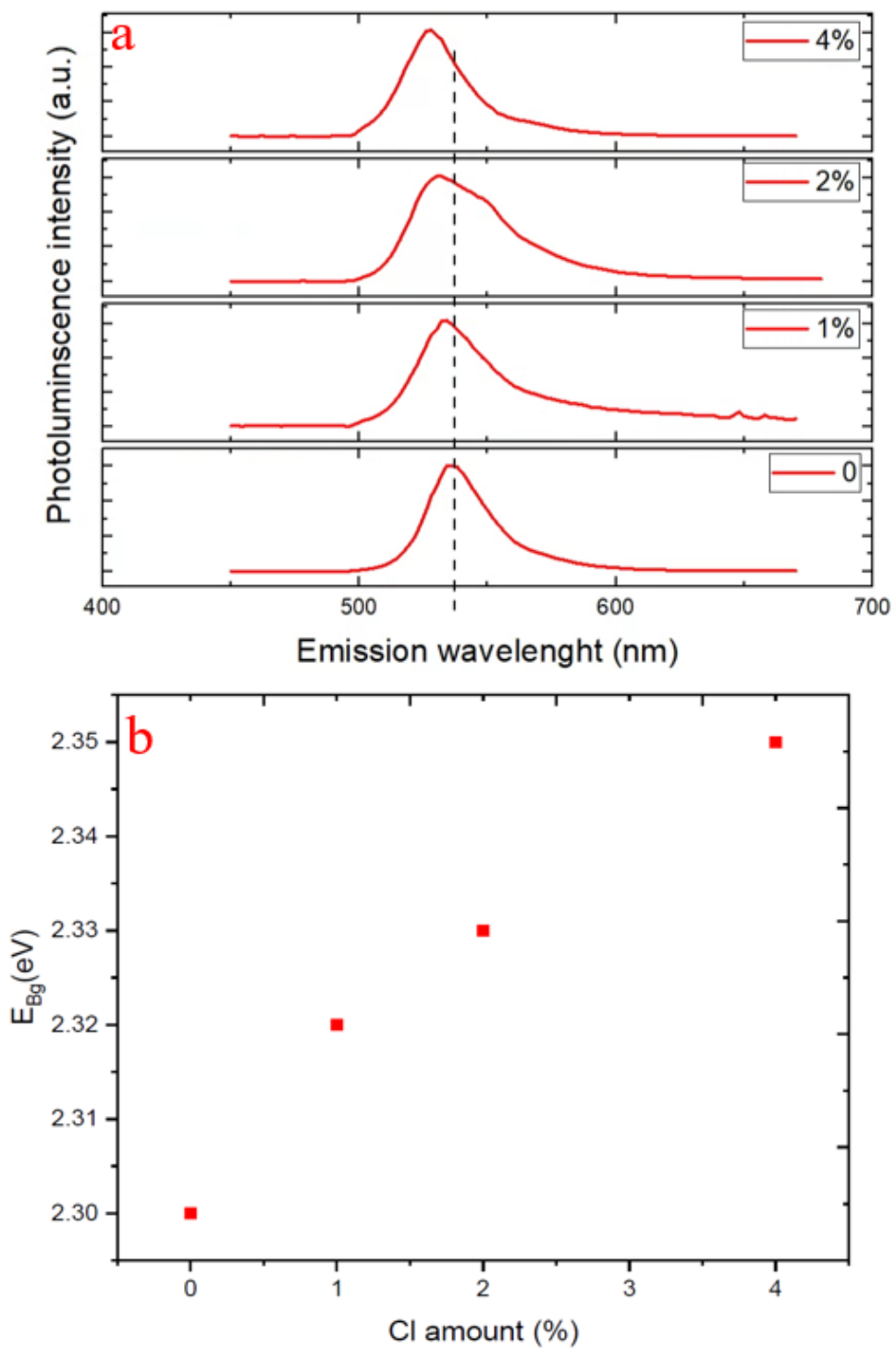


Figure 4.5. Photoluminescence peaks of MAPbBr₃ single crystal with 0% - 4% Cl doping (a), and the measured band gap of the crystals (b).

A study was conducted to evaluate the effects of chlorine (Cl) doping on the optical properties of MAPbBr₃ crystals using a temperature-dependent photoluminescence (PL) technique. *Figure 4.6* depicts the normalized cryogenic PL emission intensity of the prepared crystals in the form of a pseudo-color map. As shown in the plot, the cryogenic PL patterns of Cl-doped crystals were observed to be broader and less intense compared to the pure MAPbBr₃.

As discussed in the preceding chapter, the emission of photoluminescence (PL) from semiconductors is influenced by two crucial material-specific parameters: exciton-phonon scattering and exciton binding energy [117], [118]. Exciton-phonon scattering, primarily attributed to various types of defects, intentional, and unintentional inclusion of impurities, such as doping, provides a pathway for nonradiative recombination. On the other hand, the exciton binding energy is largely dependent on the band composition of the material, and if this energy is higher, it can provide pathways to increase radiative recombination, because the high energy reduces non radiative recombination [115].

The effect of both parameters is evident in the pseudo plot, which demonstrated peak broadening, attributed to increased exciton-phonon scattering as a result of an increase in Cl doping concentration, which by definition is an impurity. On the other hand, the observed increase in the emission energy of Cl-doped crystals with increasing Cl concentration could serve as an avenue to decrease nonradiative recombination. Therefore, the net effect of Cl doping on the optical performance is a compromise between these two factors.

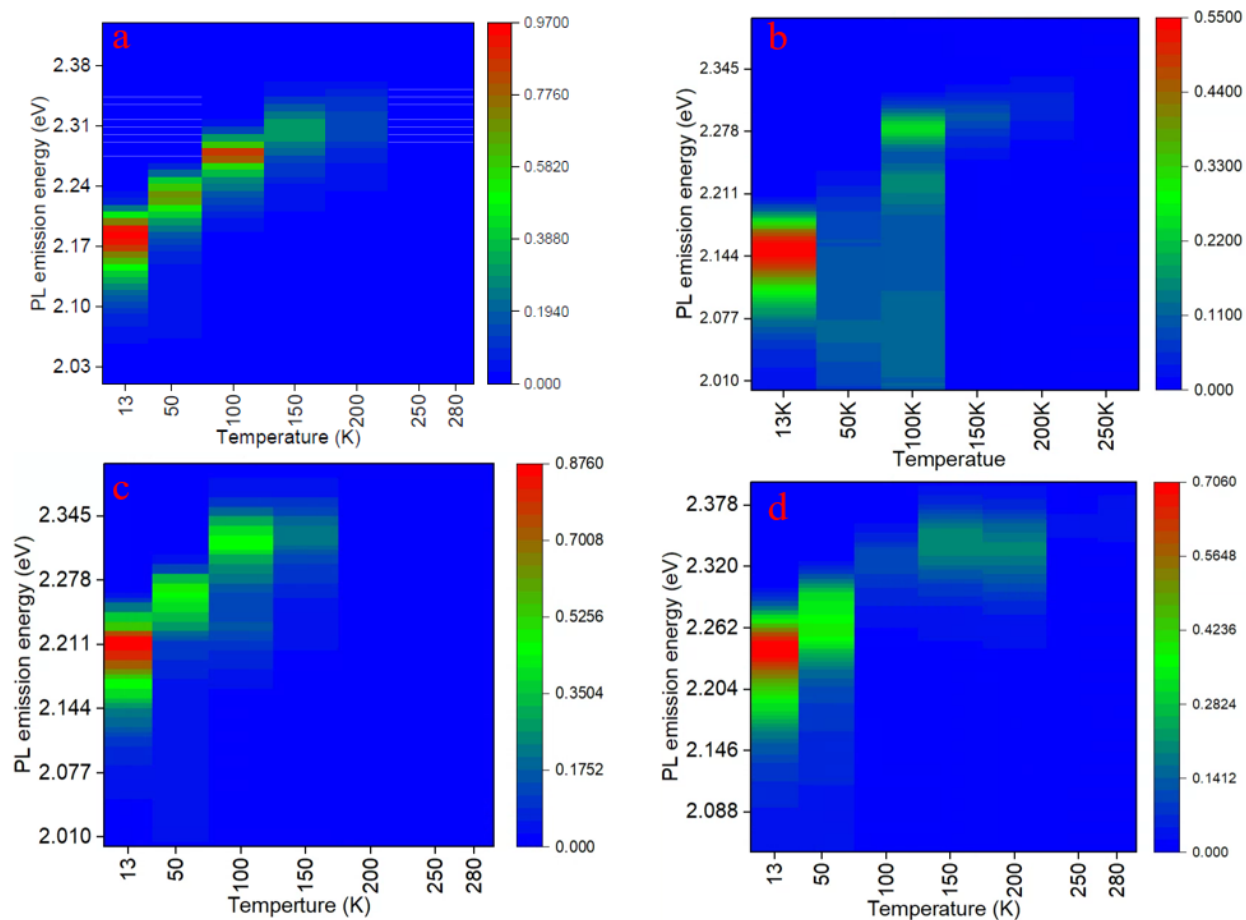


Figure 4.6. Pseudo-color maps of temperature dependent PL emission spectra of pure MAPbBr₃ (a) 1%, 2% and 4% Cl doped MAPbBr₃ single crystals (b),(c), and (d), respectively.

Figures 4.7a and 4.7b display the cryogenic photoluminescence (PL) emission spectra for both pure and 4% Cl-doped MAPbBr₃ single crystals. Both samples exhibit the atypical [12]–[14] blue shift, which has been previously discussed and will not be expanded upon in this context. Crystal phase changes can also cause emission shifts, and it is known that MAPbBr₃ undergoes several phase transitions, including alpha to beta, gamma, and delta phases, at temperatures of 230 K, 160 K, and 150 K, respectively, as illustrated in Figure 4.7, while the pure crystal consistently displays

a shift towards longer wavelengths, the 4% chloride-doped crystal reveals a deviation from this pattern, exhibiting a shift towards longer wavelengths up to 200 K, followed by a reversal and a return to the regular trend between 200 K and 150 K. This suggests that the phase changes occurring in this temperature range may be responsible for the observed deviation, and absence of it could suggest the better stability of the pure crystal.

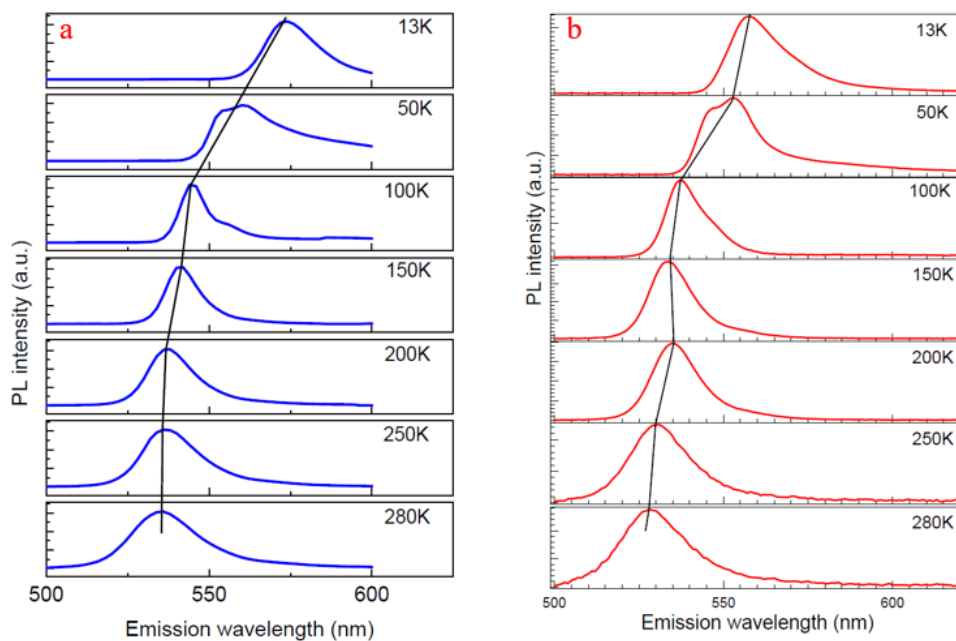


Figure 4.7. Temperature dependent PL emission spectra of pure (a) and 4% Cl- doped (b)MAPBBr₃ single crystals.

4.2.4 I-V Characterization

To investigate the changes in electrical properties of MAPbBr₃ crystals resulting from Cl doping, direct current (DC) measurements were conducted under dark conditions. This was achieved by selecting crack and surface defect-free crystals from the as-grown samples and preparing devices by polishing the surfaces mechanically and depositing 100 nm Ni and Cr electrode contacts on opposite sides. The devices were then placed in a dark environment, and the current response was measured as the bias voltage was swept from 0 to 20V. As depicted in *Figure 4.8*, the current-voltage (I-V) curves of the pure and Cl-doped MAPbBr₃ single crystals exhibited both linear and non-linear regions. Two key observations were made from these plots: first, a declining dark current trend was observed with an increase in the Cl doping amount, and second, as summarized in *Table 4.2*, a trend of increasing resistivity with an increase in Cl doping amount was observed. Additionally, the voltage at the trap-filled limit (V_{TFL}) values obtained from the I-V curve was used to determine the trap density of crystals using *Equation 3-2* and *Equation 3-3* elaborated in the preceding chapter.

The findings corroborate the hypothesis that Cl doping has a dual positive effect on the electrical properties of MAPbBr₃ single crystals. Initially, as depicted in the figure, the dark current of the Cl-doped single crystals exhibited a reduction of over 8%, attributable to the reduction in the number of free electrons and holes that contribute to the dark current. Furthermore, the resistivity of the single crystals was increased by more than an order of magnitude, from 3.4×10^7 to $1.7 \times 10^9 \Omega \cdot \text{cm}$, with the addition of 4% Cl. This enhancement can be attributed to the expansion of the band gap, which increased the energy required for electrons to transition from the valence band to the conduction band, thereby limiting the number of carriers that could be activated. Lastly, while doping, which involves introducing impurities into a material, caused raised concerns about

the potential increase in trap density, it is reassuring to find that doping did not actually result in an increase in trap sites but rather slightly decreased the trap density. This improved trap density may be attributed to the strong attraction force between the cations and Cl^- anions compared to the Br^- anions. That better strength reduces the mobility or migration of ions and, in effect minimizes the number of trap sites.

Table 4.2. Summary of electrical resistivity and trap density of Cl doped-MAPbBr₃ single crystals.

Cl amount (%)	Resistivity ($\Omega\cdot\text{cm}$)	Trap density (cm^{-3})
0	3.4×10^7	5.1×10^{10}
1	2.7×10^8	3.9×10^{10}
2	5.1×10^8	3.1×10^{10}
3	7.2×10^8	4.6×10^{10}
4	1.7×10^9	1.0×10^{10}

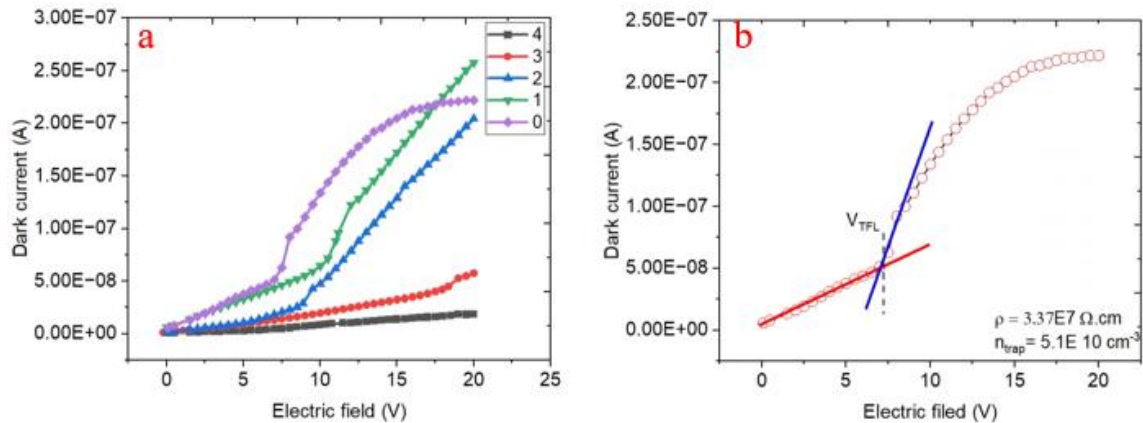


Figure 4.8. Dark current response of MAPbBr₃ single crystals with 0% up to 4% Cl doping

(a), Dark current response of a pure MAPbBr₃ single crystal (b).

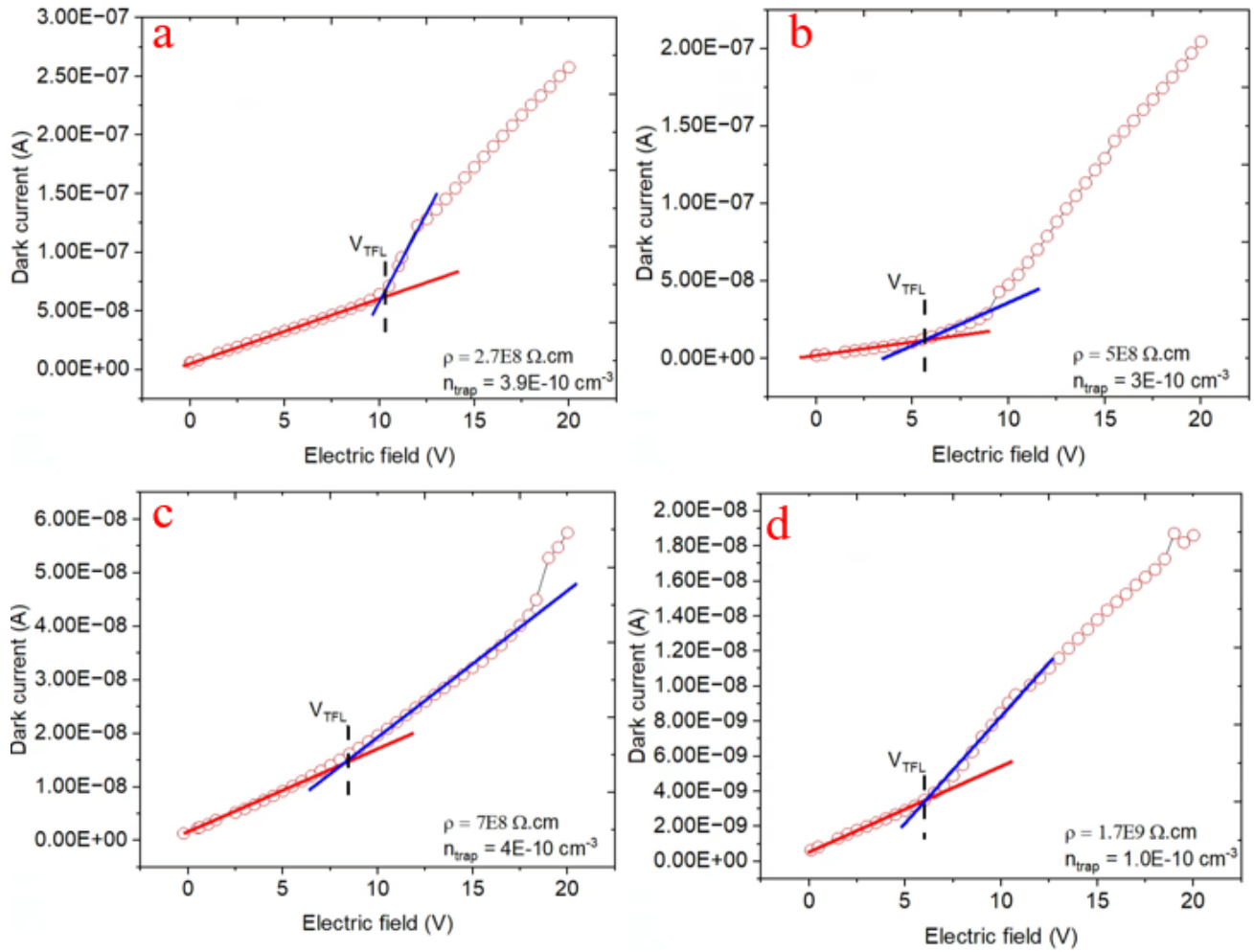


Figure 4.9. I-V curves of Cl-doped MAPbBr₃ single crystals under dark condition with varying amount of Cl doping level 1% (a), 2% (b), 3% (c), and 4% (d).

4.2.4.1 Charge Carriers Mobility lifetime product

The evaluation of the mobility lifetime product ($\mu\tau$) for the prepared crystals was carried out using the modified Hecht Equation [20], as previously described. The photocurrent response of the MAPbBr₃ devices was measured by exposing the crystals to a 365 nm, 12 W, blue LED light, and by applying an electric field ranging from 0 V to 20 V using a Keithley source measuring unit 2450. The plot of the electric field against the measured photocurrent is shown in *Figure 4.10 a-e*. The calculated $\mu\tau$ values *Figure. 4.10f* from the fitting of the modified Hecht equation are 1.12×10^{-2} , 8×10^{-3} , 1.15×10^{-2} , 1.79×10^{-2} , and 2.5×10^{-2} cm²V⁻¹ for crystals grown with 0%, 1%, 2%, 3%, and 4% substitution of MAPbBr₃ with MAPbCl₃, respectively.

The results indicate that crystals prepared with Cl doping exhibited improved $\mu\tau$ values, except for the crystal prepared with 1% substitution. The increase in $\mu\tau$ values suggests that at Cl doping concentrations greater than 2%, did not impact the mobility of carriers by acting as scattering sites. However, at a 1% doping level, a reduction in mobility was observed. This could be attributed to an imbalance in the PbBr₆⁴⁻ octahedra caused by the limited substitution of Br⁻ with Cl⁻ [144], which may have caused several defect states that acted as scattering sites, as demonstrated by the lower energy and broader peak in the cryogenic PL spectra of such crystals.

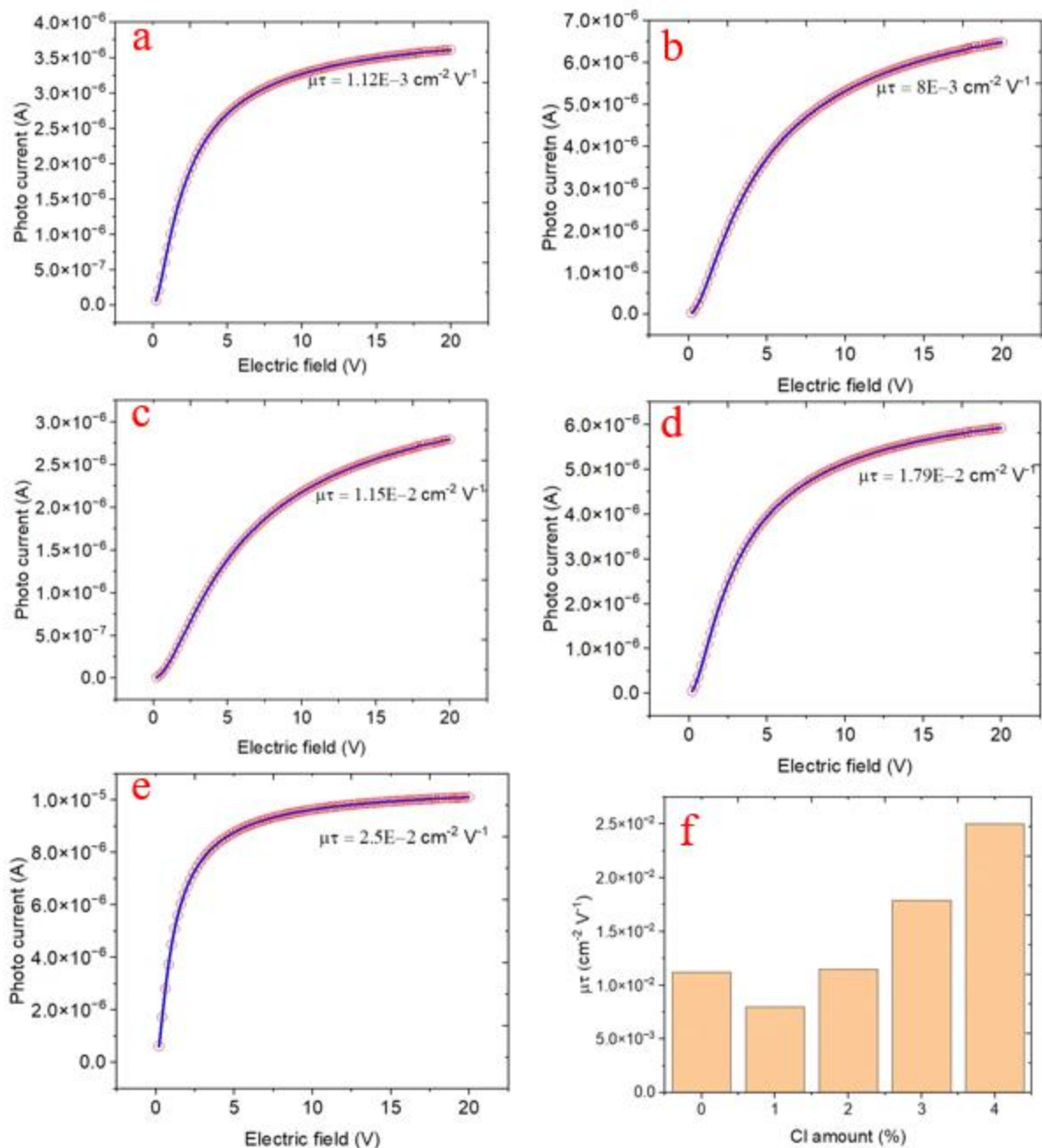


Figure 4.10. photocurrent- electric field curves and fitted modified Hect function (a), (b), (c), (d), and (e), and for 0%, 1%, 2%, 3%, 4% Cl-doped MAPbBr₃ single crystals, respectively. bar plot of calculated mobility life time product (f)

4.2.5 Radiation detection using Cl-doped MAPbBr₃ single crystals.

4.2.5.1 X-ray detection

Based on the outcomes of the preceding material characterization studies, it can be inferred that the process of Cl-doping has enhanced the electrical properties of MAPbBr₃ single crystals. The low dark current and high resistivity of Cl-doped crystals have the potential to improve X-ray sensitivity, which is a crucial parameter in X-ray detection. To assess the impact of Cl-doping on the sensitivity of MAPbBr₃ devices, the on and off current responses of the devices were measured under various electric fields at an X-ray dose rate of 69.1 $\mu\text{Gyair s}^{-1}$. The net current, which is the difference between the on and off current, was plotted in *Figure 4.11a*. The results demonstrate that crystals fabricated using Cl-doping generally exhibited higher current responses, which may be attributed to the combined effect of increased resistivity, reduced dark current, and enhanced charge mobility properties.

Moreover, the X-ray sensitivity of the Cl-doped MAPbBr₃ detectors was calculated using *Equation 3-5* [21], as described in the preceding chapter, and the sensitivity of the devices against the electric bias field is illustrated in *Figure 4.11b*. Similarly, to the current response, the crystals produced with Cl- doping exhibited superior sensitivity. The plot indicates that the maximum obtained X-ray sensitivity using a 4% Cl-doped single crystal is 15, 21.3, and 3.8 times better than the MAPbBr₃ single crystals with 0%, 1%, and 3% Cl-doping. The sensitivity of the devices fabricated in this study at a bias of 40 V is compared against the best-reported values for new materials and currently available commercial detectors in *Table 4.3*. As depicted in the table, the sensitivity of MAPbBr₃ devices produced in this work is 155.9 times higher than the commercially

available α -Se detectors [145], and 3.3 times better than the best-in-class sensitivity of Si integrated MAPbBr₃ devices [145].

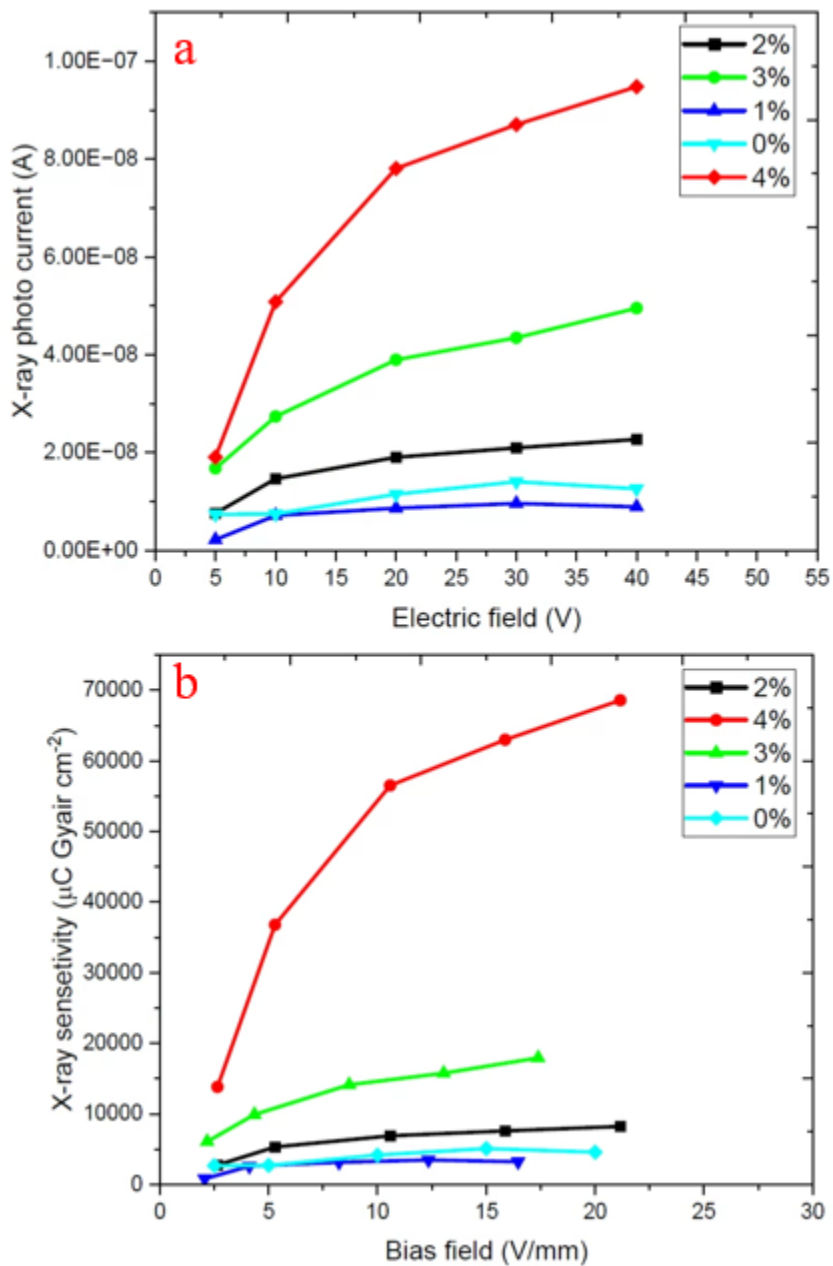


Figure 4.11. X-ray photo current-voltage (*I-V*) curve of 0% - 4% Cl-doped MAPbBr₃ crystals

(a), X-ray sensitivity of MAPbBr₃ crystals grown 0% - 4% Cl-doping (b).

Table 4.3. Summary of selected representative X-ray sensitivity of new and commercially available detector materials.

Material	Sensitivity ($\mu\text{C Gyair cm}^{-2}$)	Applied bias field (V/mm)	Reference
4%Cl MAPbBr ₃	68593	17	This work
3%Cl MAPbBr ₃	17954	16	This work
2%Cl MAPbBr ₃	8228	21	This work
1%Cl MAPbBr ₃	3242	20	This work
MAPbBr ₃	4579	24	This work
MAPbBr ₃	2552	4.5	[129]
Cs ₃ Bi ₂ I ₉	1652	50	[128]
CsPbBr ₃	619	45	[129]
Si-integrated MAPbBr ₃	21000	7	[145]
α -Se	440	15000	[128]

4.2.5.2 γ -ray detection

The doping of MAPbBr₃ with Cl⁻ has resulted in a material with high photon stopping power and excellent electrical properties, making it an attractive candidate for gamma-spectroscopy applications. However, the successful application of gamma-spectroscopy depends on the ability to analyze time and energy-dependent signals with pulse analysis electronics [107]. To achieve this, it is essential to minimize the time it takes for charge carriers to reach the electrode, which requires high drift velocity and drift length. While applying a higher bias voltage across the detector can help achieve this, it may be restricted by the detector noise level.

To evaluate the gamma detection performance of Cl-doped and pure MAPbBr₃ single crystals, MAPbBr₃ radiation detector devices were fabricated using 4% Cl-doped and pure MAPbBr₃ single crystals. Similar to the devices employed in X-ray measurements, the detector devices featured 100nm Ni and Cr electrodes, and the crystals were mounted on a custom-prepared circuit board and placed in a radio frequency shielding box. To minimize noise, the box was evacuated to 0.1 mbar using a vacuum pump, and the detector was connected to a Kromek ev550 charge-sensitive preamplifier via a 6-inch BNC cable. The output of the preamplifier was then routed to an Ortec 672 amplifier, whose output was fed to a Kromek 102 multichannel analyzer. Finally, the spectrum was acquired using MultiSpec software by Kromek.

In a typical gamma detection routine in this work, the source was placed 3 centimeters above the detector, which was supplied with a bias of +200 V, with the positive terminal connected to the Cr electrode. The preamplifier gain was set at 200x, and the shaping time was fixed at 10 microseconds. The energy resolution (ER) [107], which is a critical measure of a detector's ability

to discern the fine energy spectrum of a nuclear decay, was calculated using *Equation 4-5* where, E_γ is energy of the gamma, FWHM is the full width at half maximum of the photopeak. To evaluate the performance of the MAPbBr₃ single crystals in comparison to state-of-the-art CZT detectors, the ²⁴¹Am and ¹³⁷Cs gamma spectra were acquired using the MAPbBr₃ single crystals and the GR1 CZT detector manufactured by Kromek.

$$ER = \frac{FWHM}{E_\gamma} \quad (4-5)$$

Figure 4.12a displays the gamma spectrum obtained using 4% Cl-doped MAPbBr₃ and CZT detectors. As demonstrated in the close-up view of *Figure 4.12b*, the ²⁴¹Am 56KeV gamma peak was resolved, and the corresponding energy resolution of 0.13 and 4.8 was determined for MAPbBr₃ and CZT, respectively. Additionally, *Figure 4.13a* shows the ¹³⁷Cs gamma spectrum acquired using pure MAPbBr₃, 4% Cl-doped MAPbBr₃, and a CZT detector. As depicted in the close-up view of *Figure 4.13b*, the detector made with Cl-doping was able to show a small 662 keV peak, while the detector made with pure MAPbBr₃ was not able to show a properly defined peak. Several attempts were made to obtain a spectrum with pure MAPbBr₃, however, the attempts remained futile due to the higher noise the detector demonstrated when biased at 200 V. An attempt was also by lowering the bias voltage, but when the bias was lowered, the pulse was completely lost due to the reduced charge collection efficiency.

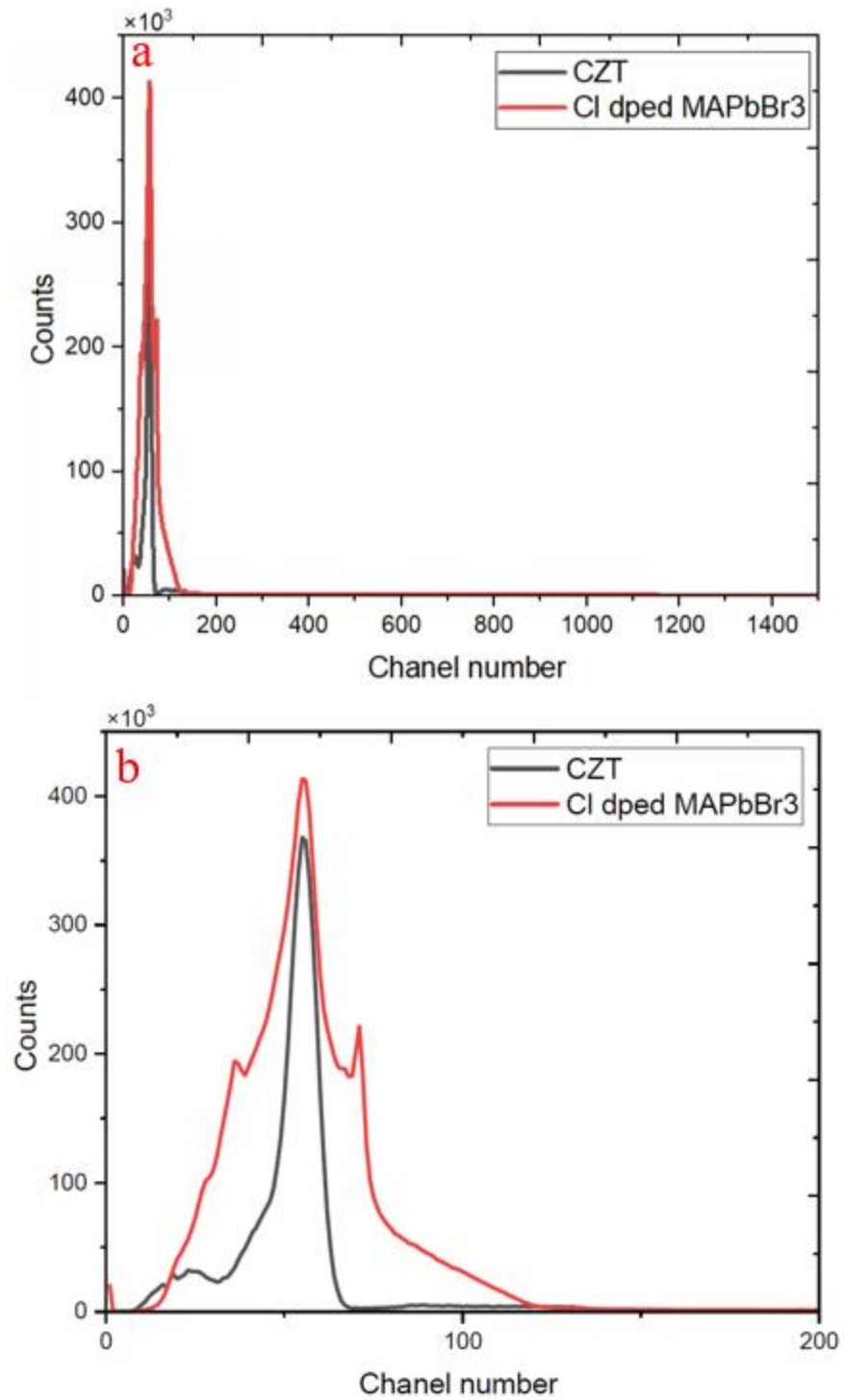


Figure 4.12. ^{241}Am 56 keV gamma spectrum acquired using 4% Cl- doped MAPbBr₃ crystal and Kromek GRI CZT detector (a), a close-up view of the ^{241}Am spectrums (b).

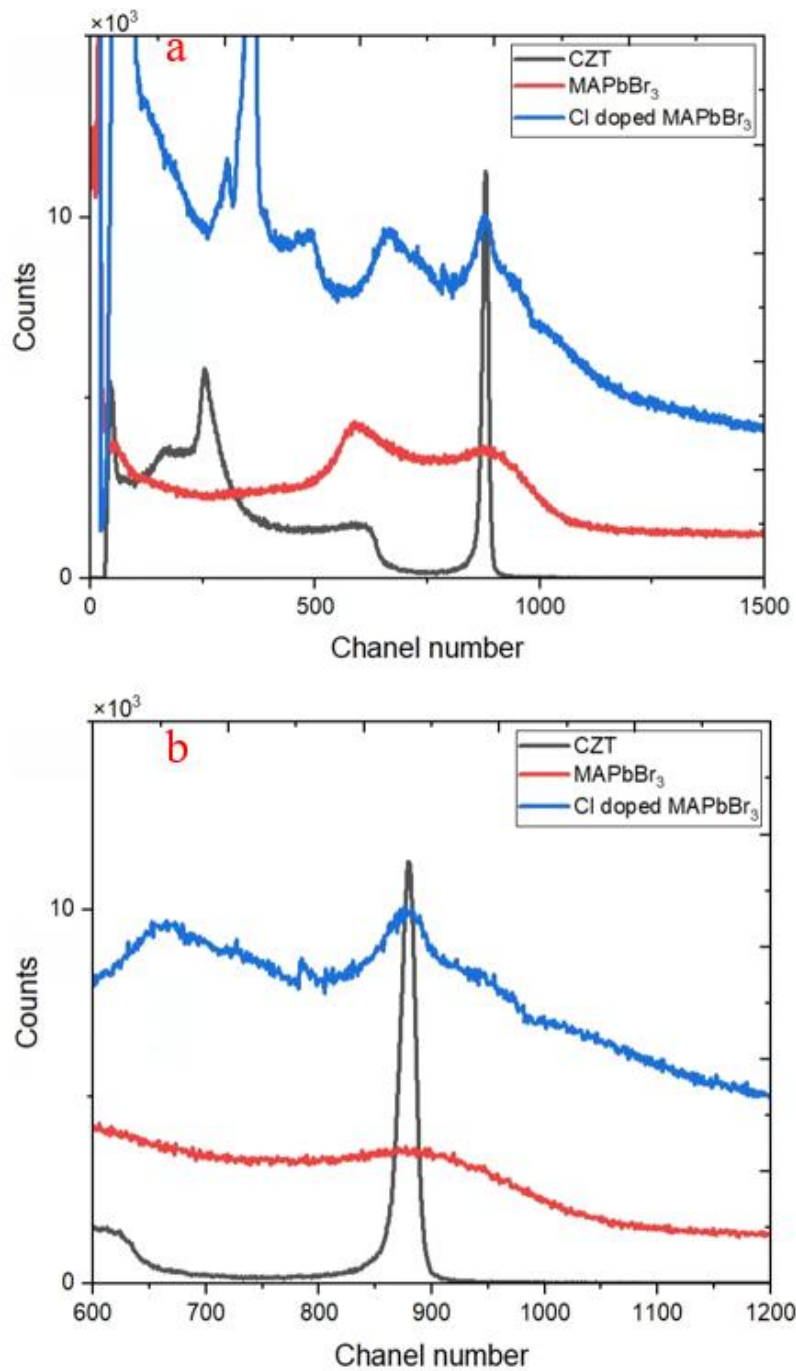


Figure 4.13. X-ray photo current-voltage (I-V) curve of 0%-4% Cl-doped MAPbBr₃ crystals

(a), X-ray sensitivity of MAPbBr₃ crystals grown 0%-4% Cl-doping (b).

4.3 Conclusion

The MAPbBr₃ single crystals with varying amounts of Cl doping were successfully grown using the PAITC method. The chemical, optical, electrical, and radiation detector performance of the prepared crystals was evaluated. The results demonstrated that the Cl doping was able to successfully improve the electrical properties of the crystal. Furthermore, the crystal showed improved charge mobility lifetime product. The gamma-ray detection performance was evaluated by resolving ²⁴¹Am and ¹³⁷Cs gamma spectrums using MAPbBr₃ detectors. It was also demonstrated that the X-ray sensitivity of 4% Cl- doped MAPbBr₃ single crystal is 68593 $\mu\text{C Gyair Cm}^{-2}$ which is 155 better than the sensitivity of currently widely utilized X-ray detector material α -Se. To the best of our knowledge, this is the is the best value reported for this class of material. Overall, the significantly improved detector performance of Cl-doped MAPbBr₃ was attributed to the enhanced electrical properties achieved through Cl doping, and it is confirmed that MAPbBr₃ has excellent potential as a material for detecting ionizing radiation.

Chapter 5. Electrode Engineering for Improved Sensitivity of

MAPbBr₃ X-Ray Detectors

5.1 Introduction

Halide perovskites have drawn significant attention due to their exceptional potential as next-generation materials for various electronic applications [104], [146], [147], [148], [149], [150], [151]. Applications such as photovoltaics, LEDs, lasers, transistors, and radiation detectors can benefit from improved performance achieved by using perovskite materials [151]. However, the efficient and reliable electrode contact required for each of these applications is challenged by the instability of perovskite-metal contacts, which is attributed to intricate interfacial effects and high reactivity due to the ionic nature of perovskite materials [152]. Additionally, the stability of these materials is compromised by their vulnerability to moisture and oxygen. Therefore, designing efficient contact is crucial to effectively harness the promising attributes of halide perovskites and leverage their full potential in electronic applications.

The development of MAPbBr₃ as an affordable radiation detector necessitates the development of efficient electrode contacts through electrode engineering[152]. Although the utilization of MAPbBr₃ for radiation detectors is a relatively new endeavor, extensive research has been conducted on the impact of electrode material selection on interfacial engineering in MAPbBr₃ thin film devices[153], [154], [155], [156], [157], [158]. As a result, most thin film devices use hole and/or electron transport layers between the electrode metal and the film to create efficient charge transfer. However, recent reports have shown that single-crystal devices without carrier

transport layers are better suited for radiation detectors[152], making it essential to investigate how metal contact selection affects overall radiation detection performance.

One of the primary goals of electrode engineering in perovskite single crystals is to efficiently extract and transport charges from the perovskite layer to the external circuit[152]. This requires proper alignment of the energy levels between the perovskite and electrode materials, as well as a low-resistance contact. The work function difference between the metal and the semiconductor is a crucial parameter in determining the Schottky barrier height, which is essential for controlling the carrier flow rate and direction. The work function of a semiconductor lies between the conduction and valance band, as shown in Figure 5.1, where the work function of commonly used metal electrode materials and the conduction and valance band of MAPbBr₃ are plotted. As indicated by the plot, all of these metals could potentially be used as electrode material for MAPbBr₃.

The other objective of electrode engineering for MAPbBr₃ devices is to ensure the long-term stability and reliability of the contact interfaces[158]. This is crucial due to the ionic nature of perovskite materials, which readily interact with metal contacts, causing gradual degradation through metal diffusion into the perovskite matrix, redox reactions, and surface polarization[152]. These issues can result in the formation of impurities or defects, distortion of the electric field, or device destabilization. For example, gold has been demonstrated to create interfacial polarization with methylammonium lead halide perovskites. Silver contacts can lead to iodine and methylammonium ion diffusion and the formation of an AgI barrier[159], while fullerene-based contacts can allow moisture ingress towards the hygroscopic perovskite[160]. Therefore, a careful selection of materials must be accomplished to avoid surface polarization as well as diffusion.

The phenomenon of interfacial polarization, resulting from electrochemical interactions between the perovskite material and the contact electrode[152], leads to the formation of interfacial dipole moments and local electric fields. This, in turn, can have detrimental effects such as device hysteresis, nonradiative recombination, and interface decomposition. To mitigate this phenomenon, it is recommended to select contact materials that prevent its formation. Lin et al. demonstrated the interfacial stability between MAPbI₃ perovskite and a series of noble and transition metals was analyzed by employing first-principles calculations, As illustrated in Figure 5.2, the results indicated that Au, Ag, Cu, and Pd tend to form charged metal complexes with low formation energies, while Cr, Ni, Co, and Mo form metal complexes with higher formation energies. Hence, the utilization of metals with higher formation energies can help avoid this detrimental effect.

In an effort to develop MAPbBr₃ as a radiation detector, and given the critical role that electrode materials play in device performance, it is worth exploring the impact of various contact materials on the overall performance. Chromium and nickel were selected for this study due to their favorable work function and limited reactivity with the crystal surface. Additionally, gold was chosen as it is one of the most commonly used materials for electrodes. In this chapter, a comparison of the electric properties and device performance of various MAPbBr₃ devices with similar and dissimilar metal contact is discussed. The I-V properties were examined, and finally, the effect of electrode material on X-ray detection performance was analyzed.

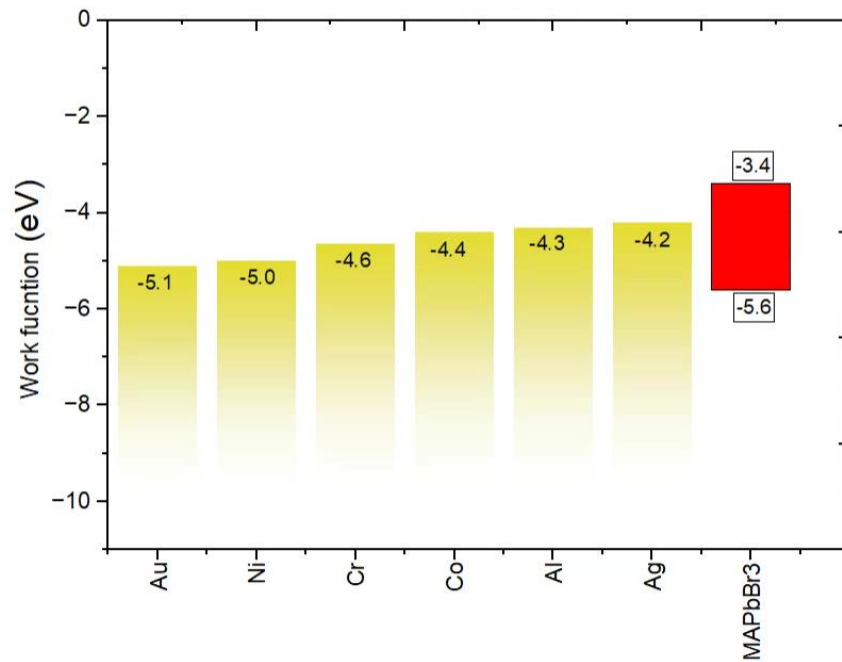


Figure 5.1. Work function of commonly used electrode materials and the energy level of MAPbBr3 perovskite.

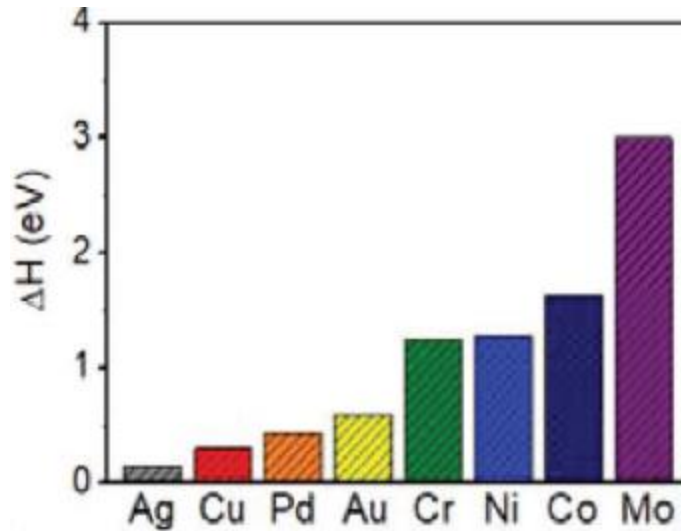


Figure 5.2. Formation energy of metal complex with N type perovskite [152].

5.2 I-V characterization

In order to investigate the I-V response of MAPbBr₃ devices fabricated with various electrode contact material combinations, high-quality crystals were carefully selected and prepared with both faces mechanically polished. Four different types of electrode combinations, Au-Sc-Au, Cr-Sc-Au, Cr-Sc-Cr, and Cr-Sc-Ni, each with a thickness of 100 nm, were deposited using an E-beam evaporator. The devices were then placed in a dark environment, and the current response was measured as the bias voltage was swept from -20 V to 20 V. As shown in *Figure 5.3*, the I-V curves of the crystals prepared with various metal combinations exhibited different responses. Devices made with similar contact materials, Au-SC-Au and Cr-Sc-Cr, showed ohmic responses, confirming the formation of ohmic contacts. However, devices made with dissimilar metal contacts showed rectifying (Schottky) characteristics.

An ohmic contact is a type of electrical junction that facilitates the unimpeded flow of current in both directions between two conductors without any appreciable rectification or power

dissipation. In contrast, a Schottky contact exhibits rectifying behavior, allowing current to flow more readily in one direction than the other. As illustrated in the plots, Schottky devices typically exhibit lower dark current compared to ohmic contacts. Both types of contacts have their own unique advantages and disadvantages. In radiation detection, ohmic contacts are often operated at low bias voltages due to the challenge of increased dark current when the bias is increased. However, low bias can often lead to inefficient charge collection. Therefore, a MAPbBr₃ crystal with a dissimilar contact could potentially be more efficient for radiation detection.

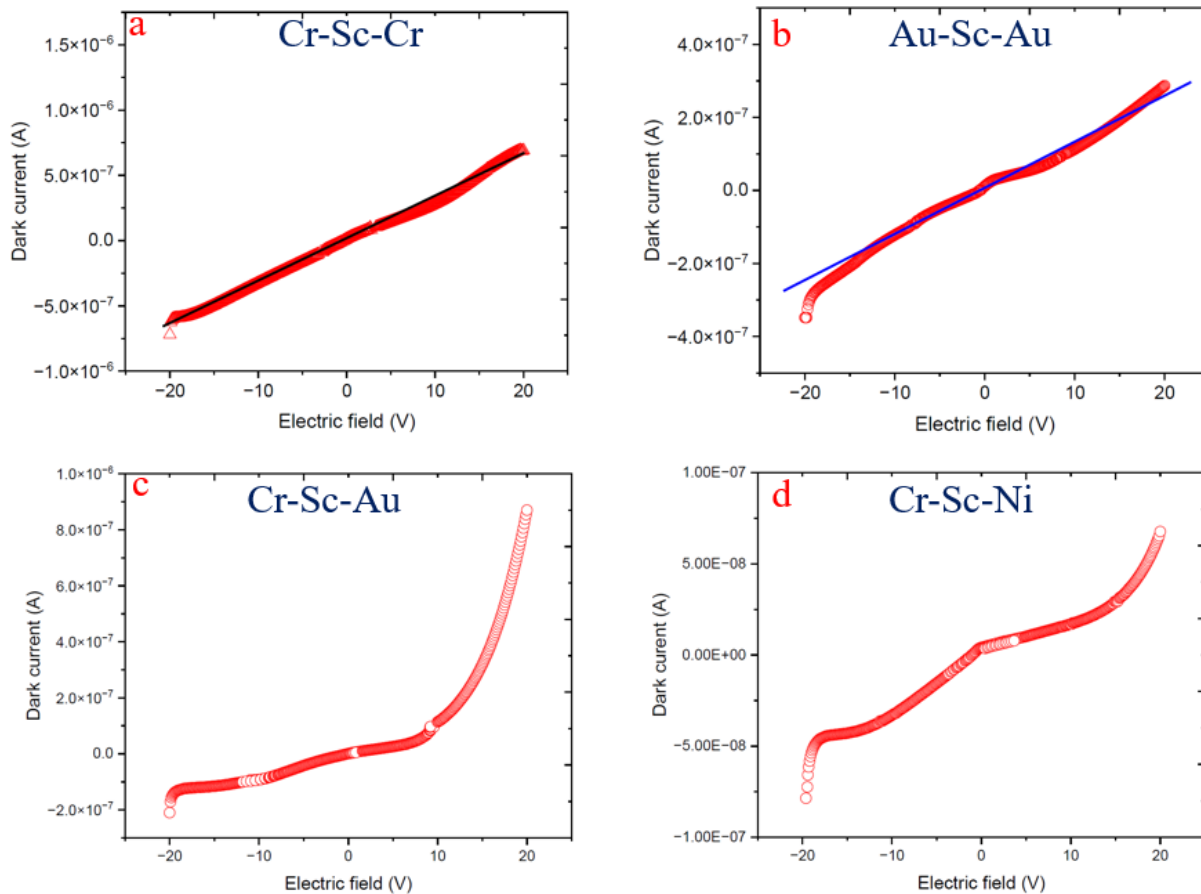


Figure 5.3. *I*-curves of MAPbBr₃ devices fabricated with Cr-Sc-Cr (a), Au-Sc-Au(b) Cr-Sc-Au(c), and Cr-Sc-Ni (d) electrode metal contact.

5.3 X-Ray Detection Performance

In order to evaluate the influence of electrode selection on the X-ray sensitivity of MAPbBr₃ devices, the current responses of the devices were measured under different electric fields at a constant X-ray dose rate of $69.1 \mu\text{Gyair s}^{-1}$. The net current, which represents the difference between the on and off current, was graphed in Figure 5.4. The data reveals that devices with

dissimilar metal contacts typically displayed higher current responses, which may be attributed to the low dark current associated with the Schottky devices.

The sensitivity of the detector was determined using *Equation 3-5*, as described in the preceding chapter, and the calculated values are depicted in *Figure 5.5*. The results demonstrate that the MAPbBr₃ devices with different contacts exhibited superior sensitivity. Specifically, the sensitivity of the best performing device, Cr-SC-Ni, was 5.76, 3.8, and 1.4 times greater than that of Au-SC-Au, Cr-Sc-Cr, and Cr-SC-Au devices, respectively.

Furthermore, the signal-to-noise ratio (SNR) of the detector was calculated to assess the stability of the signal, as shown in *Equation 5-1*, where I_{noise} is the standard deviation of the photocurrent and I_{signal} is the difference between the dark and photocurrent. *Figure 5.6* depicts the contrast between the on and off current of the MAPbBr₃ devices at a bias voltage of 20V. As indicated in the plots, the SNR values for the devices were 27.1, 14.1, 9.43, and 5.3 for Cr-SC-Ni, Cr-SC-Au, Cr-Sc-Cr, and Au-SC-Au, respectively. These results confirm the superiority of the Cr-SC-Ni device for radiation detection.

$$SNR = \frac{I_{signal}}{I_{noise}} \quad (5-1)$$

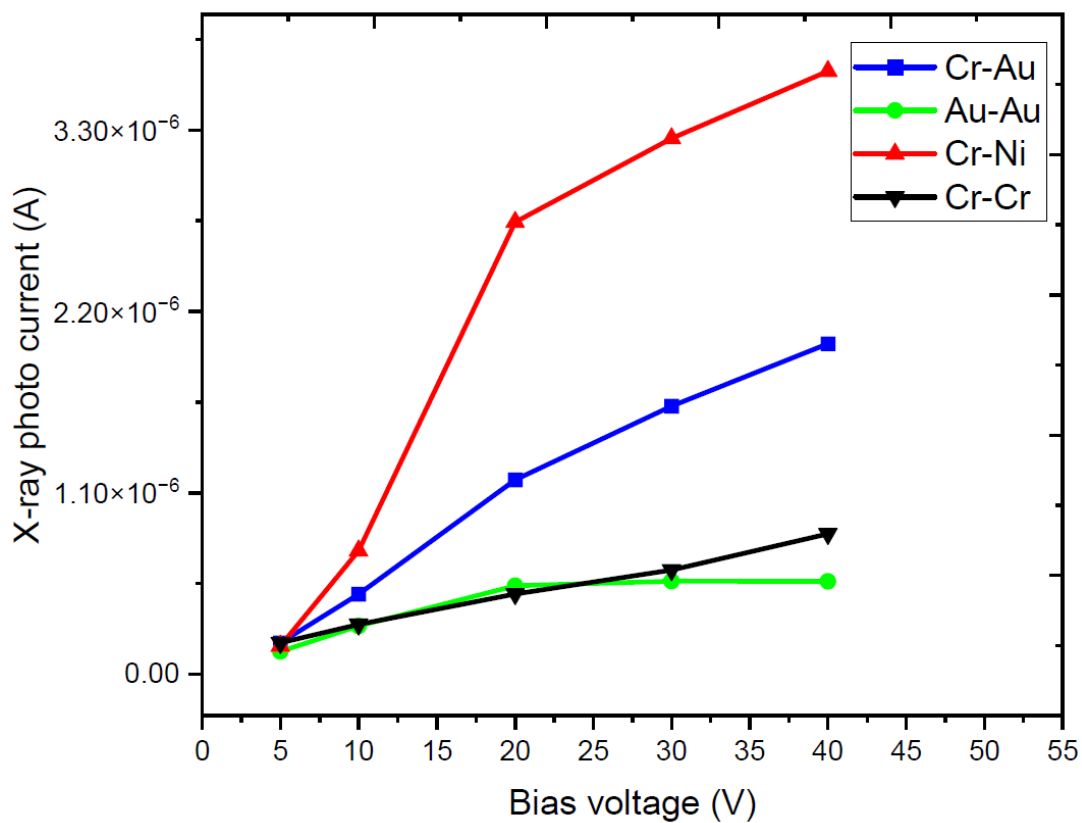


Figure 5.4. X-ray photo current-voltage (I-V) curve of MAPbBr₃ devices made with various electrode metal combination.

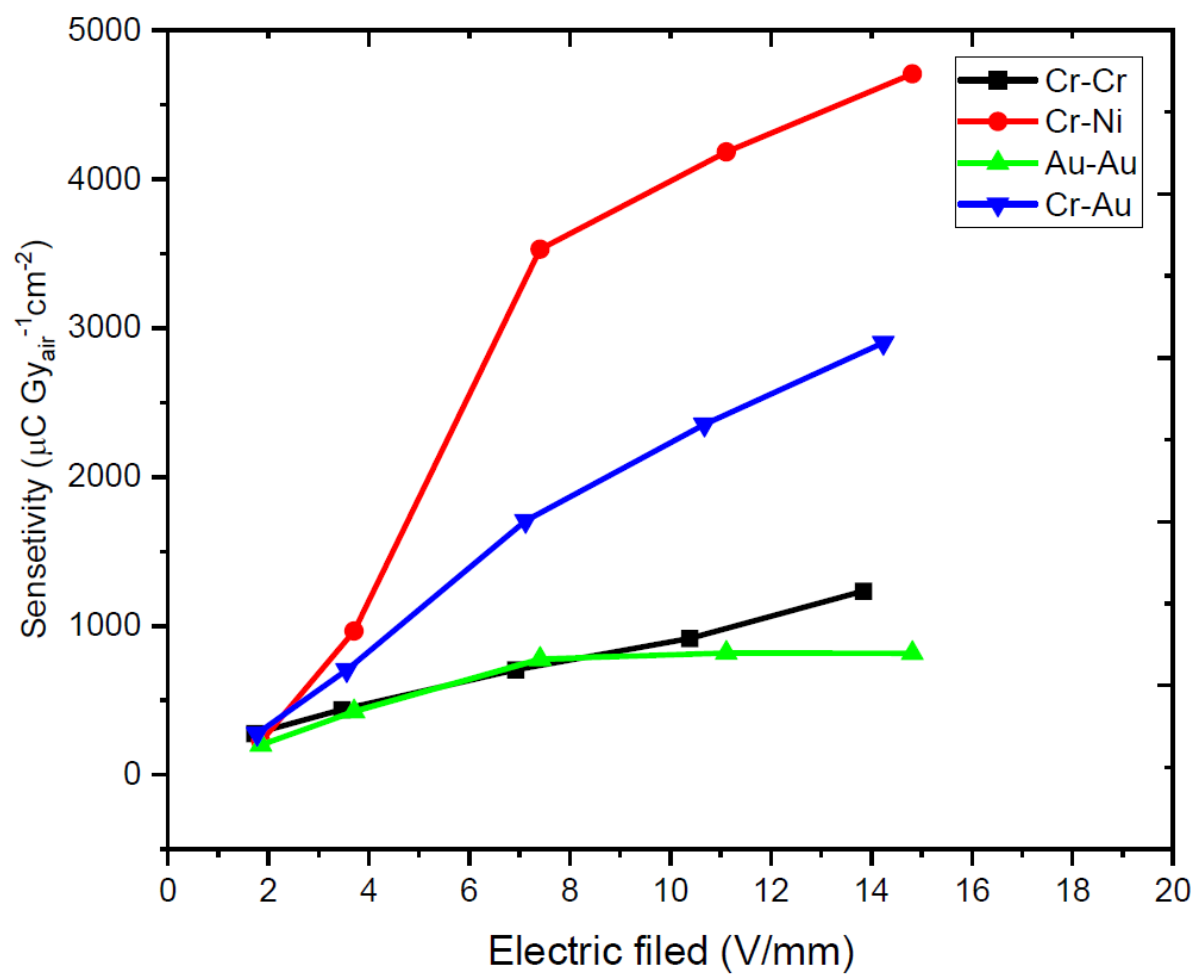


Figure 5.5, X-ray sensitivity of MAPbBr₃ devices made with various electrode metal combination,

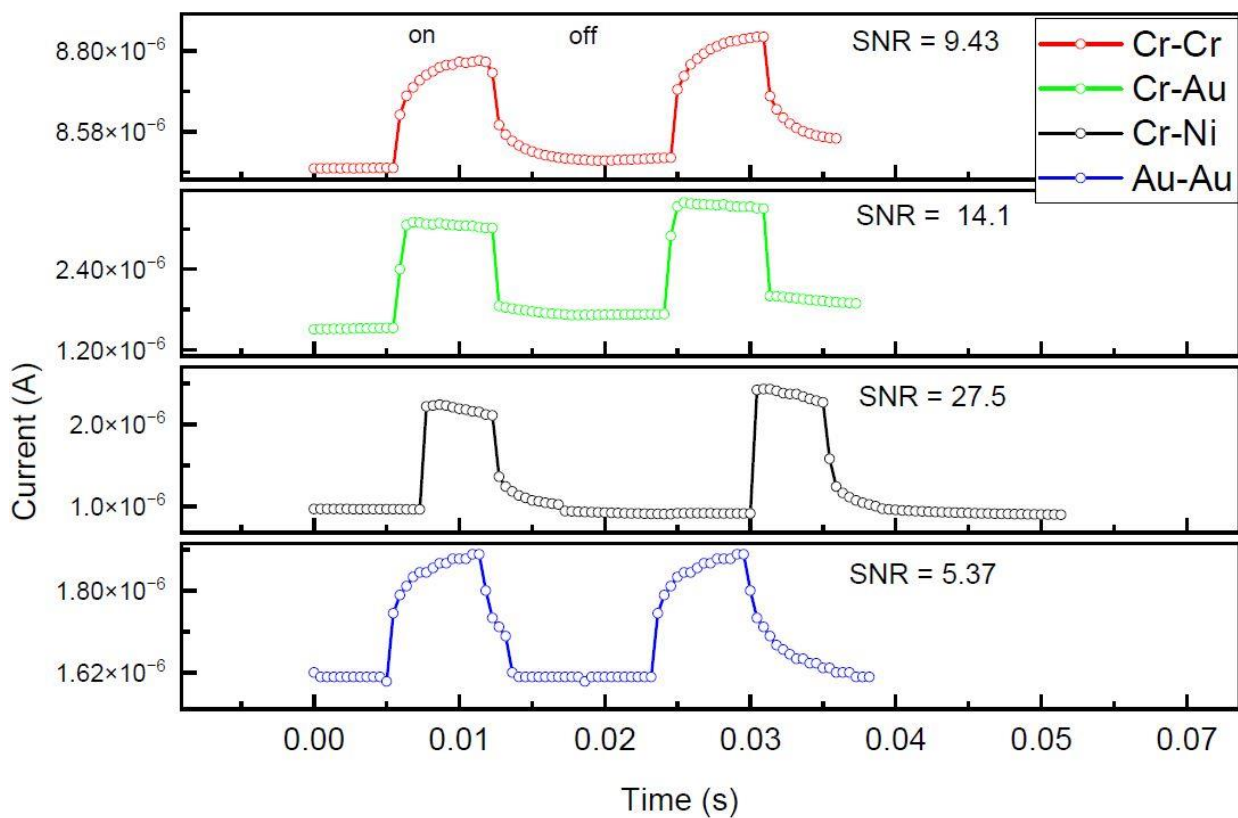


Figure 5.6. X-ray on and off current of MAPbBr₃ devices made with various electrode metal combination.

5.4 Impedance Spectroscopy

In order to gain a more profound understanding of the dynamic processes at the interface between MAPbBr₃ single crystals and metal electrodes, the impedance spectroscopy technique was employed to measure the capacitance of the devices at various frequencies. Specifically, the capacitance reading of a semiconductor sample is influenced by the applied frequency, with mid to high frequencies revealing bulk properties away from the interface and low frequencies highlighting interface properties[160]. Therefore, the capacitance measurement at low frequency can be utilized to scan for indications of surface polarization. To obtain the capacitance measurements, BP-300 potential stat was employed, and the capacitance was measured from 1Hz to 100kHz. *Figure 5.7* illustrates the frequency-dependent capacitance of MAPbBr₃ devices prepared with various electrode material combinations. As depicted in the plot, at low frequency, the device fabricated with similar Au contacts on both sides exhibited higher capacitance, indicating a higher accumulation of ionic and electronic charges. However, the devices made with Cr-Cr and Cr-Au combinations showed some accumulation, while the devices made with the Cr-Ni combination did not display increased capacitance at low frequency, suggesting that the device was not being polarized. Consequently, in light of the impedance spectroscopy results, the superior performance of the Cr-Ni device is attributed to the combination of a Schottky barrier device and reduced polarization of the surface due to the more inert properties of nickel and chromium electrodes.

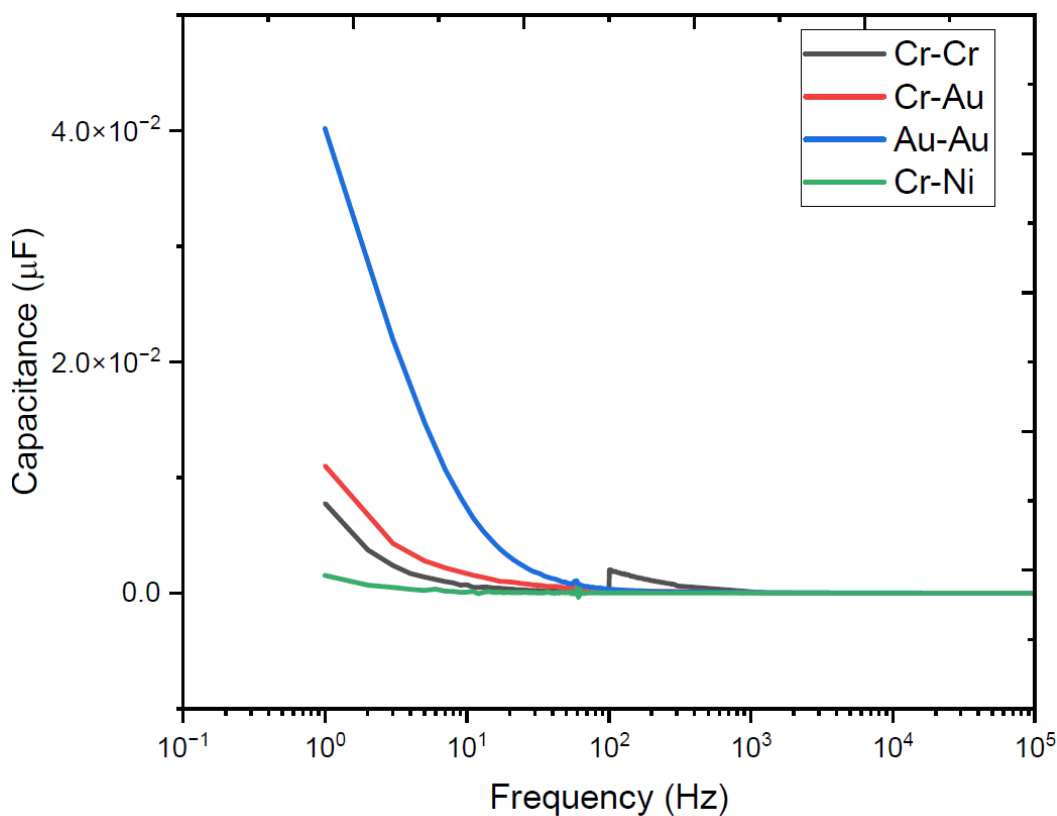


Figure 5.7. Frequency-dependent capacitance of MAPbBr₃ devices prepared with Au-Sc-Au, Cr-Sc-Au, Cr-Sc-Cr, and Cr-Sc-Ni electrode combination.

5.5 Conclusion

In summary, the effect of electrode metal selection on the performance of MAPbBr₃ detector devices was investigated. Devices with Au-Sc-Au, Cr-Sc-Cr, Cr-Sc-Cr, and Cr-Sc-Ni electrode metal combinations were prepared, and their I-V curves were analyzed. It was observed that devices with similar contacts formed ohmic contacts, while devices with dissimilar metal combinations showed Schottky contacts. The X-ray performance of the devices was also examined, and it was found that the Cr-Sc-Ni combination showed superior sensitivity and signal-to-noise ratio (SNR) due to its reduced dark current and reduced surface polarization. As a result, this combination of electrode materials was chosen for the studies conducted in Chapters 3 and 4.

Chapter 6. Conclusion and Future Work

This dissertation investigated the development of MAPbBr₃ for radiation detection through three interrelated components. First, an improved crystal growth method was designed and studied to meet the requirements of radiation detection. Second, the effect of Cl-doping with MAPbBr₃ was studied to enhance material properties necessary for radiation detection. Lastly, electrode engineering for improved sensitivity of MAPbBr₃ detectors was explored.

Radiation sensing requires large volume and high-quality crystals. The solution-based crystal growth methods currently available do not fully satisfy the need, that they either take more than two weeks if they produce high quality crystals or they are too fast that quality crystals cannot be grown. The PAITC is shown to be an innovative solution that bridges the gap between these two, so that high quality crystals could be grown in less than 2 days, this was achieved by effectively regulating the rate of crystal growth using PPG polymer. When compared with traditional ITC, the PAITC method was able to grow crystal up to 11 times bigger. Furthermore, the photoluminescence and I-V studies have shown that the crystal made through ITC have improved quality, more than nine times better carrier mobility lifetime product was observed. Additionally, the x-ray sensitivity of the crystals made through the PAITC method was improved by 1.5 times with the use of 0.01 g/ml of PPG, and by 6.9 times with the use of 0.03 g/ml of PPG. However, the use of higher concentrations of PPG led to slower crystal growth rates of up to a week. Overall, the PAITC method has been shown to produce high-quality crystals in a reasonable amount of time, making it a suitable approach for growing similar organic-inorganic perovskites such as MAPbX, FAPbX (X= Cl, Br, and I) and it could lead to wider adoption of such materials for radiation sensing as well as other photonic applications.

The impact of electrode metal selection on the performance of MAPbBr₃ detectors in terms of radiation sensing was investigated. To this end, a few candidate metals were chosen based on their work function alignment and reactivity with perovskites. The Au-Sc-Au, Cr-Sc-Cr, Au-Sc-Ni, and Cr-Sc-Ni combinations were prepared. The results showed that the sensitivity of the device was influenced by the metal selection, with the Cr-Sc-Ni combination exhibiting improved sensitivity. This was attributed to the favorable band alignment and inertness of the material, which avoided surface polarization, resulting in significantly lower dark current compared to the other electrode combinations examined. The use of Cr and Ni for electrode metal is a new practice, as Au has traditionally been the dominant choice for electronic applications. However, these results underscore that careful selection of the metal contact is necessary to unlock the full potential of perovskite devices, and that Cr and Ni could play an important role in this regard.

Despite the successful increase in the size and quality of crystals through PAITC, pure MAPbBr₃ crystals did not exhibit gamma spectroscopic response. To overcome this limitation, the Cl-doping of MAPbBr₃ was explored. The samples with 1%-4% Cl doping were evaluated for their chemical, optical, electrical, and radiation detector performance. The results demonstrated that Cl doping increased the resistivity of the material by more than an order of magnitude, and it was attributed to the slight increase in the band gap of Cl-doped crystals as confirmed by PL studies. Additionally, the $\mu\tau$ product was found to be improved as well. The combination of these improvements enabled the Cl-doped crystal to show spectroscopic response. Most importantly, the enhancements led to an impressive X-ray sensitivity of 68593 $\mu\text{C Gy}^{-1}\text{cm}^{-2}$, which is the best

reported value for this class of materials and it is 155 times better than what is commercially available currently.

The metal halide perovskites grown by the PAITC method have displayed significant potential for use as a low-cost and versatile radiation sensor for nuclear security and X-ray imaging applications. Their ease of fabrication, high X-ray sensitivity, and ability to modify their stoichiometry to achieve desired capabilities such as neutron sensitivity through doping with lithium are among their appealing characteristics. This dissertation has made notable achievements in identifying and addressing a number of obstacles in developing MAPbBr₃ detectors. However, there are still significant challenges that need to be addressed.

The X-ray sensitivity of MAPbBr₃ crystals has been demonstrated to surpass the industry standard, however, their practical implementation requires significant study on their long-term stability and reliability as organic perovskites, including MAPbBr₃, are prone to degradation, which can lead to performance loss. Therefore, it is essential to address the long-term stability and reliability of perovskite detectors. Furthermore, the devices prepared in this study only employed mechanical polishing for surface preparation, and there is room for improvement through chemical polishing, interface engineering, and the utilization of oxide layers. Lastly, this work has focused primarily on improving the material properties of MAPbBr₃, but an ocean of work is needed to address further improvement through the development of appropriate electronics and signal analysis algorithms that are compatible with perovskite detectors.

References

- [1] J.J Hack et al., Exascale requirements reviews energy crosscut report, US Department of Energy, March 9-10, 2017, Tyson Corner, Virginia.
- [2] D. E. Hinkel, “Scientific and technological advancements in inertial fusion energy,” *Nuclear Fusion*, vol. 53, no. 10, Oct. 2013, doi: 10.1088/0029-5515/53/10/104027.
- [3] T. A. Kurniawan *et al.*, “Technological solutions for long-term storage of partially used nuclear waste: A critical review,” *Annals of Nuclear Energy*, vol. 166. Elsevier Ltd, Feb. 01, 2022. doi: 10.1016/j.anucene.2021.108736.
- [4] Z. Wang *et al.*, “Application of carbon dots and their composite materials for the detection and removal of radioactive ions: A review,” *Chemosphere*, vol. 287. Elsevier Ltd, Jan. 01, 2022. doi: 10.1016/j.chemosphere.2021.132313.
- [5] A. C. Hayes, “Applications of nuclear physics,” *Reports on Progress in Physics*, vol. 80, no. 2. Institute of Physics Publishing, Feb. 01, 2017. doi: 10.1088/1361-6633/80/2/026301.
- [6] P. De Marcillac, N. Coron, G. Dambier, J. Leblanc, and J. P. Moalic, “Experimental detection of α -particles from the radioactive decay of natural bismuth,” *Nature*, vol. 422, no. 6934, pp. 876–878, Apr. 2003, doi: 10.1038/nature01541.
- [7] Sverre Lodgaard, “*Nuclear Disarmament and Non-Proliferation*”, First editon. Milton Park : Rutledge Global Security Studies, 2011.

- [8] W. J. Puglia and B. Atefi, "Examination of issues related to the development and implementation of real-time operational safety monitoring tools in the nuclear power industry," 1995.
- [9] S. N. Kile, "Nuclear Arms Control and Non-proliferation," *SIPRI Yearbook 2004: Armaments, Disarmament and International Security*, pp. 617–619, 2011, [Online]. Available: <http://en>.
- [10] G. M. West, S. D. J. McArthur, and D. Towle, "Industrial implementation of intelligent system techniques for nuclear power plant condition monitoring," *Expert Syst Appl*, vol. 39, no. 8, pp. 7432–7440, Jun. 2012, doi: 10.1016/j.eswa.2012.01.107.
- [11] C.R.Hiring, "Needs and Performance Requirements for Neutron Monitoring in the Nuclear Power Industry" *Radiation Protection Dosimetry*, Vol.70, no, 1-4 PP67-72, 1997
- [12] M. Hoheisel, "Review of medical imaging with emphasis on X-ray detectors," *Nucl Instrum Methods Phys Res A*, vol. 563, no. 1, pp. 215–224, Jul. 2006, doi: 10.1016/j.nima.2006.01.123.
- [13] H. Bradford Barber, "Applications of semiconductor detectors to nuclear medicine," *Nuclear Instruments and Methods in Physics Research A*, vol. 436, pp. 102–110, 1999.
- [14] S. Bhattacharya, M. Frank, K. Huitu, U. Maitra, B. Mukhopadhyaya, and S. K. Rai, "Probing the light radion through diphotons at the Large Hadron Collider," *Physical Review D - Particles, Fields, Gravitation and Cosmology*, vol. 91, no. 1, Jan. 2015, doi: 10.1103/PhysRevD.91.016008.

- [15] D. G. Darambara, "State-of-the-art radiation detectors for medical imaging: Demands and trends," *Nucl Instrum Methods Phys Res A*, vol. 569, no. 2 SPEC. ISS., pp. 153–158, Dec. 2006, doi: 10.1016/j.nima.2006.08.054.
- [16] D. J. Wagenaar *et al.*, "Development of MRI-Compatible Nuclear Medicine Imaging Detectors," in *IEEE Nuclear Science Symposium Conference Record*, 2006, pp. 1825–188.
- [17] C. Scheiber, "CdTe and CdZnTe detectors in nuclear medicine," *Nuclear Instruments and Methods in Physics Research A*, vol. 448, pp. 513–524, 2000.
- [18] M. Khoshakhlagh, J. Islamian, S. Abedi, and B. Mahmoudian, "Development of Scintillators in Nuclear Medicine," *World J Nucl Med*, vol. 14, no. 03, pp. 156–159, Jul. 2015, doi: 10.4103/1450-1147.163241.
- [19] D. G. Darambara and A. Todd-Pokropek, "Solid state detectors in Nuclear Medicine," *Q J NUCL MED*, vol. 46, pp. 3–7, 2002.
- [20] A. Barzilov and M. Kazemeini, "Unmanned aerial system integrated sensor for remote gamma and neutron monitoring," *Sensors (Switzerland)*, vol. 20, no. 19, pp. 1–14, Oct. 2020, doi: 10.3390/s20195529.
- [21] A. Pour Yazdanpanah, J. Hartman, E. Regentova, and A. Barzilov, "Sparse-view neutron-photon computed tomography: Object reconstruction and material discrimination," *Applied Radiation and Isotopes*, vol. 132, pp. 122–128, Feb. 2018, doi: 10.1016/j.apradiso.2017.11.029.

- [22] M. Kazemeini, Z. Cook, J. Lee, A. Barzilov, and W. Yim, “Plug-and-play radiation sensor components for unmanned aerial system platform,” *J Radioanal Nucl Chem*, vol. 318, no. 3, pp. 1797–1803, Dec. 2018, doi: 10.1007/s10967-018-6233-2.
- [23] J. Hartman and A. Barzilov, “Computational Study of Integrated Neutron/Photon Imaging for Illicit Material Detection,” *Phys Procedia*, vol. 66, pp. 85–94, 2015, doi: 10.1016/j.phpro.2015.05.013.
- [24] A. Barzilov and P. C. Womble, “Study of Doppler broadening of gamma-ray spectra in 14-MeV neutron activation analysis,” *J Radioanal Nucl Chem*, vol. 301, no. 3, pp. 811–819, 2014, doi: 10.1007/s10967-014-3189-8.
- [25] A. P. Barzilov, I. S. Novikov, and B. Cooper, “Computational study of pulsed neutron induced activation analysis of cargo,” in *Journal of Radioanalytical and Nuclear Chemistry*, Oct. 2009, pp. 177–181. doi: 10.1007/s10967-009-0298-x.
- [26] L. Clinckemalie, D. Valli, M. B. J. Roeffaers, J. Hofkens, B. Pradhan, and E. Debroye, “Challenges and Opportunities for CsPbBr₃ Perovskites in Low- and High-Energy Radiation Detection,” *ACS Energy Letters*, vol. 6, no. 4. American Chemical Society, pp. 1290–1314, Apr. 09, 2021. doi: 10.1021/acsenerylett.1c00007.
- [27] E. Enlow and S. Abbaszadeh, “State-of-the-art challenges and emerging technologies in radiation detection for nuclear medicine imaging: A review,” *Frontiers in Physics*, vol. 11. Frontiers Media SA, 2023. doi: 10.3389/fphy.2023.1106546.
- [28] H. Wei and J. Huang, “Halide lead perovskites for ionizing radiation detection,” *Nature Communications*, vol. 10, no. 1. Nature Publishing Group, Dec. 01, 2019. doi: 10.1038/s41467-019-08981-w.

- [29] J. Seco, B. Clasié, and M. Partridge, “Review on the characteristics of radiation detectors for dosimetry and imaging,” *Physics in Medicine and Biology*, vol. 59, no. 20. Institute of Physics Publishing, pp. R303–R347, Oct. 21, 2014. doi: 10.1088/0031-9155/59/20/R303.
- [30] D. G. Darambara, “State-of-the-art radiation detectors for medical imaging: Demands and trends,” *Nucl Instrum Methods Phys Res A*, vol. 569, no. 2 SPEC. ISS., pp. 153–158, Dec. 2006, doi: 10.1016/j.nima.2006.08.054.
- [31] T. Yang, F. Li, and R. Zheng, “Recent advances in radiation detection technologies enabled by metal-halide perovskites,” *Materials Advances*, vol. 2, no. 21. Royal Society of Chemistry, pp. 6744–6767, Nov. 07, 2021. doi: 10.1039/d1ma00569c.
- [32] F. Liu *et al.*, “Recent Progress in Halide Perovskite Radiation Detectors for Gamma-Ray Spectroscopy,” *ACS Energy Letters*, vol. 7, no. 3. American Chemical Society, pp. 1066–1085, Mar. 11, 2022. doi: 10.1021/acsenergylett.2c00031.
- [33] F. Liu *et al.*, “Halide perovskites and perovskite related materials for particle radiation detection,” *Nanoscale*. Royal Society of Chemistry, 2022. doi: 10.1039/d2nr01292h.
- [34] Y. Gao, Y. Pan, F. Zhou, G. Niu, and C. Yan, “Lead-free halide perovskites: A review of the structure-property relationship and applications in light emitting devices and radiation detectors,” *Journal of Materials Chemistry A*, vol. 9, no. 20. Royal Society of Chemistry, pp. 11931–11943, May 28, 2021. doi: 10.1039/d1ta01737c.
- [35] L. Gao and Q. Yan, “Recent Advances in Lead Halide Perovskites for Radiation Detectors,” *Solar RRL*, vol. 4, no. 2, Feb. 2020, doi: 10.1002/solr.201900210.
- [36] S. Flugge, *Nuclear Instrumentation II, Encyclopedia Of Physics*, vol. XLV. 1958.

- [37] Herbert Friedman, “Geiger Counter Tubes,” in *Proceedings Of The I.R.E- Waves and Electronics Section* , Jul. 1949, pp. 791–809.
- [38] Leon F. Curtiss, “The_Geiger_Müller_Counter,” *National bureau of Standards Circular* , vol. Google books, 1950.
- [39] M. Grodzicka-Kobylka, M. Moszyński, and T. Szczęśniak, “Silicon photomultipliers in gamma spectroscopy with scintillators,” *Nuclear Instruments and Methods in Physics Research, Section A: Accelerators, Spectrometers, Detectors and Associated Equipment*, vol. 926. Elsevier B.V., pp. 129–147, May 11, 2019. doi: 10.1016/j.nima.2018.10.065.
- [40] Ian Rittersdorf, “Gamma Ray Spectroscopy,” *Nuclear Engineering & Radiological Sciences, University of Michigan* . 2007.
- [41] A. T. Farsoni and D. M. Hamby, “A system for simultaneous beta and gamma spectroscopy,” *Nucl Instrum Methods Phys Res A*, vol. 578, no. 3, pp. 528–536, Aug. 2007, doi: 10.1016/j.nima.2007.06.020.
- [42] H. M. Qadr, “Effect of Ion Irradiation on the Mechanical Properties of High and Low Copper,” *Atom Indonesia*, vol. 46, no. 1, pp. 47–51, Apr. 2020, doi: 10.17146/AIJ.2020.923.
- [43] T. J. Aucott *et al.*, “Impact of detector efficiency and energy resolution on gamma-ray background rejection in mobile spectroscopy and imaging systems,” *Nucl Instrum Methods Phys Res A*, vol. 789, pp. 128–133, Jul. 2015, doi: 10.1016/j.nima.2015.04.012.
- [44] P. M. Johns and J. C. Nino, “Room temperature semiconductor detectors for nuclear security,” *J Appl Phys*, vol. 126, no. 4, Jul. 2019, doi: 10.1063/1.5091805.

- [45] J. Singh and R. T. Williams, *Excitonic and Photonic Processes in Materials*, vol. 203. Singapore: Springer Series in Materials Science, 2015. [Online]. Available: <http://www.springer.com/series/856>
- [46] Stefaan Tavernier, “Experimental Techniques in Nuclear and Particle Physics,” New York, 2022.
- [47] G. A. Morton, “Nuclear Radiation Detectors,” 1962.
- [48] Gopal B. Saha, “Physics and Radiobiology of Nuclear Medicine,” New York, 2006.
- [49] M. Nikl and A. Yoshikawa, “Recent R&D Trends in Inorganic Single-Crystal Scintillator Materials for Radiation Detection,” *Adv Opt Mater*, vol. 3, no. 4, pp. 463–481, Apr. 2015, doi: 10.1002/adom.201400571.
- [50] A. Guckes, A. Barzilov, and P. Guss, “Experimental study of directional detection of neutrons and gamma rays using an elpasolite scintillator array,” *Nucl Instrum Methods Phys Res A*, vol. 992, Mar. 2021, doi: 10.1016/j.nima.2021.165028.
- [51] J. Hartman, A. Barzilov, E. E. Peters, and S. W. Yates, “Measurements of response functions of EJ-299-33A plastic scintillator for fast neutrons,” *Nucl Instrum Methods Phys Res A*, vol. 804, pp. 137–143, Dec. 2015, doi: 10.1016/j.nima.2015.09.068.
- [52] A. Barzilov and A. Guckes, “Sensors & Transducers Time Encoded Imaging of Neutrons and Photons Using CLYC Detector Equipped with a Dual Mode Collimator,” 2019.
- [53] D. S. Mcgregor, “Materials for Gamma-Ray Spectrometers: Inorganic Scintillators,” 2018, doi: 10.1146/annurev-matsci-070616.

- [54] J. M. McKenzie, “Development Of The Semiconductor Radiation Detector,” *Nuclear Instruments and Methods*, vol. 162, pp. 49–73, 1979
- [55] G. Lutz, *Semiconductor Radiation Detectors*. Springer Berlin Heidelberg, 2007. doi: 10.1007/978-3-540-71679-2.
- [56] A. Owens and A. Peacock, “Compound semiconductor radiation detectors,” in *Nuclear Instruments and Methods in Physics Research, Section A: Accelerators, Spectrometers, Detectors and Associated Equipment*, Sep. 2004, pp. 18–37. doi: 10.1016/j.nima.2004.05.071.
- [57] M. Kazemeini, A. Barzilov, J. Lee, and W. Yim, “Integration of CZT and CLYC radiation detectors into robotic platforms using ROS,” in *AIP Conference Proceedings*, American Institute of Physics Inc., Oct. 2019. doi: 10.1063/1.5127711.
- [58] S. Linear, A. Center, and H. Spieler, “Lectures on Detector Techniques Semiconductor Detectors Part 1,” 1998. [Online]. Available: <http://www-physics.lbl.gov/~spieler>
- [59] I. C. Brownridge, *Lithium-Drifted Germanium Detectors: Their Fabrication and Use*. Springer US, 1972. doi: 10.1007/978-1-4613-4598-5.
- [60] J. Eberth and J. Simpson, “From Ge(Li) detectors to gamma-ray tracking arrays-50 years of gamma spectroscopy with germanium detectors,” *Progress in Particle and Nuclear Physics*, vol. 60, no. 2. pp. 283–337, Apr. 2008. doi: 10.1016/j.pnpnp.2007.09.001.
- [61] A. Datta, P. Becla, and S. Motakef, “Novel Electrodes and Engineered Interfaces for Halide-Semiconductor Radiation Detectors,” *Sci Rep*, vol. 9, no. 1, Dec. 2019, doi: 10.1038/s41598-019-46360-z.

- [62] A. Mirzaei, J. S. Huh, S. S. Kim, and H. W. Kim, "Room Temperature Hard Radiation Detectors Based on Solid State Compound Semiconductors: An Overview," *Electronic Materials Letters*, vol. 14, no. 3. The Korean Institute of Metals and Materials, pp. 261–287, May 01, 2018. doi: 10.1007/s13391-018-0033-2.
- [63] P. M. Johns and J. C. Nino, "Room temperature semiconductor detectors for nuclear security," *J Appl Phys*, vol. 126, no. 4, Jul. 2019, doi: 10.1063/1.5091805.
- [64] D. S. Mcgregor and H. Hermonb, "Room-temperature compound semiconductor radiation detectors," *Nuclear Instruments & Methods In Physics Research* Elsevier Section A, 1997.
- [65] R. Chaudhari, C. Ravi Kant, A. Garg, and S. K. Sharma, "A review on emerging materials with focus on BiI₃ for room-temperature semiconductor radiation detectors," *Radiation Detection Technology and Methods*, vol. 7, no. 4. Springer, pp. 465–483, Dec. 01, 2023. doi: 10.1007/s41605-023-00426-9.
- [66] M. D. Alam, S. S. Nasim, and S. Hasan, "Recent progress in CdZnTe based room temperature detectors for nuclear radiation monitoring," *Progress in Nuclear Energy*, vol. 140. Elsevier Ltd, Oct. 01, 2021. doi: 10.1016/j.pnucene.2021.103918.
- [67] A. Gädda *et al.*, "Advanced processing of CdTe pixel radiation detectors," in *Journal of Instrumentation*, Institute of Physics Publishing, Dec. 2017. doi: 10.1088/1748-0221/12/12/C12031.
- [68] C. Szeles, "CdZnTe and CdTe materials for X-ray and gamma ray radiation detector applications," in *Physica Status Solidi (B) Basic Research*, Mar. 2004, pp. 783–790. doi: 10.1002/pssb.200304296.

- [69] P. J. Sellin, “Recent advances in compound semiconductor radiation detectors,” in *Nuclear Instruments and Methods in Physics Research, Section A: Accelerators, Spectrometers, Detectors and Associated Equipment*, Nov. 2003, pp. 332–339. doi: 10.1016/j.nima.2003.08.058.
- [70] K. Yasuda *et al.*, “Development of nuclear radiation detectors with energy discrimination capabilities based on thick CdTe layers grown by metalorganic vapor phase epitaxy,” *IEEE Trans Nucl Sci*, vol. 52, no. 5 III, pp. 1951–1955, Oct. 2005, doi: 10.1109/TNS.2005.856597.
- [71] J. F. Butler *et al.*, “Cd_{1-x}Zn_xTe gamma ray detectors,” In *Conference Record of the 1991 IEEE Nuclear Science Symposium and Medical Imaging Conference*, pp. 129-133. IEEE, 1991
- [72] C. Scheiber and J. Cambron, “CdTe detectors in Medicine: a review of current applications and future perspectives”, *Nuclear Instruments and Methods in Physics Research*, A322, pp 604 -614 1992.
- [73] A. E. Bolotnikov *et al.*, “Use of high-granularity CdZnTe pixelated detectors to correct response non-uniformities caused by defects in crystals,” *Nucl Instrum Methods Phys Res A*, vol. 805, pp. 41–54, Jan. 2016, doi: 10.1016/j.nima.2015.08.051.
- [74] Y. Lei, Y. Chen, and S. Xu, “Single-crystal halide perovskites: Opportunities and challenges,” *Matter*, vol. 4, no. 7. Cell Press, pp. 2266–2308, Jul. 07, 2021. doi: 10.1016/j.matt.2021.05.002.

- [75] K. H. Kim *et al.*, “Spectroscopic properties of large-volume virtual Frisch-grid CdMnTe detectors,” *Journal of the Korean Physical Society*, vol. 66, no. 11, pp. 1761–1765, Jun. 2015, doi: 10.3938/jkps.66.1761.
- [76] M. Roth, “Advantages and Limitations of Cadmium Selenide Room Temperature Gamma Ray Detectors,” *Nuclear Instruments and Methods in Physics Research*, vol. 283, pp. 291–298, 1989.
- [77] E. Ariesanti, A. Kargar, and D. S. McGregor, “Mercuric iodide crystal growth and frisch collar detector fabrication,” in *Nuclear Technology*, American Nuclear Society, 2011, pp. 124–130. doi: 10.13182/NT11-A12280.
- [78] D. A. Vecchio, “Multi-scale Functional Nanomaterials for the Spectroscopic Detection of Ionizing Radiation and Characterization of Complex Structural Networks.”
- [79] D. Shi *et al.*, “Low trap-state density and long carrier diffusion in organolead trihalide perovskite single crystals,” *Science (1979)*, vol. 347, no. 6221, pp. 519–522, Jan. 2015, doi: 10.1126/science.aaa2725.
- [80] R. Tan, “Development of Metal Halide Perovskites for Radiation Detection,” Doctoral Dissertation , University of Tennessee Knoxville, 2022. [Online]. Available: https://trace.tennessee.edu/utk_graddiss
- [81] R. Tan, “Development of Metal Halide Perovskites for Radiation Detection,” University of Tennessee Knoxville, 2022. [Online]. Available: https://trace.tennessee.edu/utk_graddiss

- [82] H. Lei, D. Hardy, and F. Gao, “Lead-Free Double Perovskite Cs₂AgBiBr₆: Fundamentals, Applications, and Perspectives,” *Advanced Functional Materials*, vol. 31, no. 49. John Wiley and Sons Inc, Dec. 01, 2021. doi: 10.1002/adfm.202105898.
- [83] G. Volonakis *et al.*, “Cs₂InAgCl₆: A New Lead-Free Halide Double Perovskite with Direct Band Gap,” *Journal of Physical Chemistry Letters*, vol. 8, no. 4, pp. 772–778, Feb. 2017, doi: 10.1021/acs.jpcllett.6b02682.
- [84] D. H. Fabini, R. Seshadri, and M. G. Kanatzidis, “The underappreciated lone pair in halide perovskites underpins their unusual properties,” *MRS Bull*, vol. 45, no. 6, pp. 467–477, Jun. 2020, doi: 10.1557/mrs.2020.142.
- [85] T. Sato, S. Takagi, S. Deledda, B. C. Hauback, and S. I. Orimo, “Extending the applicability of the Goldschmidt tolerance factor to arbitrary ionic compounds,” *Sci Rep*, vol. 6, Apr. 2016, doi: 10.1038/srep23592.
- [86] L. Pan, Y. Feng, P. Kandlakunta, J. Huang, and L. R. Cao, “Performance of Perovskite CsPbBr₃ Single Crystal Detector for Gamma-Ray Detection,” *IEEE Trans Nucl Sci*, vol. 67, no. 2, pp. 443–449, Feb. 2020, doi: 10.1109/TNS.2020.2964306.
- [87] W. Liu *et al.*, “Twin domains in organometallic halide perovskite thin-films,” *Crystals*, vol. 8, no. 5. MDPI AG, May 01, 2018. doi: 10.3390/cryst8050216.
- [88] L. Sobotka, “Cadmium Zinc Telluride (CZT) Detectors,” *Conference presentation* . Oak Ridge, Mar. 2003.
- [89] M. D. Birowosuto *et al.*, “X-ray Scintillation in Lead Halide Perovskite Crystals,” *Sci Rep*, vol. 6, no. DOI 10.1038/srep37254, Oct. 2016.

- [90] T. Takahashi and S. Watanabe, “Recent Progress in CdTe and CdZnTe Detectors,” *IEEE Trans Nucl Sci*, vol. 48, no. 4, pp. 950–959, 2001.
- [91] K. Hitomi *et al.*, “Recent development of TlBr gamma-ray detectors,” *IEEE Trans Nucl Sci*, vol. 58, no. 4 PART 2, pp. 1987–1991, Aug. 2011, doi: 10.1109/TNS.2011.2123115.
- [92] C. C. Stoumpos *et al.*, “Crystal growth of the perovskite semiconductor CsPbBr₃: A new material for high-energy radiation detection,” *Cryst Growth Des*, vol. 13, no. 7, pp. 2722–2727, Jul. 2013, doi: 10.1021/cg400645t.
- [93] F. Arneodo, A. Di Giovanni, and P. Marpu, “A review of requirements for gamma radiation detection in space using cubesats,” *Applied Sciences (Switzerland)*, vol. 11, no. 6. MDPI AG, Mar. 02, 2021. doi: 10.3390/app11062659.
- [94] U. N. Roy, G. S. Camarda, Y. Cui, and R. B. James, “Advances in CdZnTeSe for Radiation Detector Applications,” *Radiation*, vol. 1, no. 2, pp. 123–130, Apr. 2021, doi: 10.3390/radiation1020011.
- [95] G. A. Armantrout, “Radiation Detectors: Needs and Prospects,” *Nuclear Instruments and Methods*, vol. 193, pp. 41–47, 1982.
- [96] G. Kakavelakis, M. Gedda, A. Panagiotopoulos, E. Kymakis, T. D. Anthopoulos, and K. Petridis, “Metal Halide Perovskites for High-Energy Radiation Detection,” *Advanced Science*, vol. 7, no. 22. John Wiley and Sons Inc, Nov. 01, 2020. doi: 10.1002/advs.202002098.

- [97] L. Sun, W. Li, W. Zhu, and Z. Chen, “Single-crystal perovskite detectors: development and perspectives,” *Journal of Materials Chemistry C*, vol. 8, no. 34. Royal Society of Chemistry, pp. 11664–11674, Sep. 14, 2020. doi: 10.1039/d0tc02944k.
- [98] J. Yu *et al.*, “Perovskite CsPbBr₃ crystals: Growth and applications,” *Journal of Materials Chemistry C*, vol. 8, no. 19. Royal Society of Chemistry, pp. 6326–6341, May 21, 2020. doi: 10.1039/d0tc00922a.
- [99] R. R. Sumathi *et al.*, “Development of Large-Diameter and Very High Purity Ge Crystal Growth Technology for Devices,” *Crystal Research and Technology*, vol. 58, no. 5, May 2023, doi: 10.1002/crat.202200286.
- [100] A. Zappettini *et al.*, “Growth and characterization of CZT crystals by the vertical bridgman method for X-ray detector applications,” *IEEE Trans Nucl Sci*, vol. 58, no. 5 PART 2, pp. 2352–2356, Oct. 2011, doi: 10.1109/TNS.2011.2163643.
- [101] G. Wang *et al.*, “Development of large size high-purity germanium crystal growth,” in *Journal of Crystal Growth*, Aug. 2012, pp. 27–30. doi: 10.1016/j.jcrysgro.2012.01.018.
- [102] W. Ming, D. Yang, T. Li, L. Zhang, and M. H. Du, “Formation and Diffusion of Metal Impurities in Perovskite Solar Cell Material CH₃NH₃PbI₃: Implications on Solar Cell Degradation and Choice of Electrode,” *Advanced Science*, vol. 5, no. 2, Feb. 2018, doi: 10.1002/advs.201700662.
- [103] C. H. Lin *et al.*, “Electrode Engineering in Halide Perovskite Electronics: Plenty of Room at the Interfaces,” *Advanced Materials*, vol. 34, no. 18. John Wiley and Sons Inc, May 01, 2022. doi: 10.1002/adma.202108616.

- [104] D. Shi *et al.*, “Low trap-state density and long carrier diffusion in Organo lead trihalide perovskite single crystals,” *Science (1979)*, vol. 347, no. 6221, pp. 519–522, 2015,
- [105] J. Dacuña and A. Salleo, “Modeling Space-Charge Limited Currents in Organic Semiconductors: Extracting Trap Density and Mobility,” *Phys Rev B*, vol. 84, no. 19, 2011.
- [106] D. Cao *et al.*, “Current state-of-the-art characterization methods for probing defect passivation towards efficient perovskite solar cells,” *Journal of Materials Chemistry A*, vol. 10, no. 37. Royal Society of Chemistry, pp. 19278–19303, Jun. 14, 2022. doi: 10.1039/d2ta02263j.
- [107] Y. He *et al.*, “High spectral resolution of gamma-rays at room temperature by perovskite CsPbBr₃ single crystals,” *Nat Commun*, vol. 9, no. 1, Dec. 2018, doi: 10.1038/s41467-018-04073-3.
- [108] L. Ma *et al.*, “A polymer controlled nucleation route towards the generalized growth of organic-inorganic perovskite single crystals,” *Nat Commun*, vol. 12, no. 1, Dec. 2021, doi: 10.1038/s41467-021-22193-1.
- [109] Y. Liu *et al.*, “Two-Inch-Sized Perovskite CH₃NH₃PbX₃ (X = Cl, Br, I) Crystals: Growth and Characterization,” *Advanced Materials*, vol. 27, no. 35, pp. 5176–5183, Sep. 2015, doi: 10.1002/adma.201502597.
- [110] Y. Liu *et al.*, “Low-temperature-gradient crystallization for multi-inch high-quality perovskite single crystals for record performance photodetectors,” *Materials Today*, vol. 22, pp. 67–75, Jan. 2019, doi: 10.1016/j.mattod.2018.04.002.

- [111] D. Shi *et al.*, “Low trap-state density and long carrier diffusion in organolead trihalide perovskite single crystals,” *Science (1979)*, vol. 347, no. 6221, pp. 519–522, 2015
- [112] R. Babu, L. Giribabu, and S. P. Singh, “Recent Advances in Halide-Based Perovskite Crystals and Their Optoelectronic Applications,” *Crystal Growth and Design*, vol. 18, no. 4. American Chemical Society, pp. 2645–2664, Apr. 04, 2018. doi: 10.1021/acs.cgd.7b01767.
- [113] K. H. Wang, L. C. Li, M. Shellaiah, and K. W. Sun, “Structural and Photophysical Properties of Methylammonium Lead Tribromide (MAPbBr₃) Single Crystals,” *Sci Rep*, vol. 7, no. 1, Dec. 2017, doi: 10.1038/s41598-017-13571-1.
- [114] B. Park *et al.*, “Solution-Grown MAPbBr₃ Single Crystals for Self-Powered Detection of X-rays with High Energies above One Megaelectron Volt,” *Nanomaterials*, vol. 13, no. 15, Aug. 2023, doi: 10.3390/nano13152157.
- [115] H. C. Woo, J. W. Choi, J. Shin, S. H. Chin, M. H. Ann, and C. L. Lee, “Temperature-Dependent Photoluminescence of CH₃NH₃PbBr₃ Perovskite Quantum Dots and Bulk Counterparts,” *Journal of Physical Chemistry Letters*, vol. 9, no. 14, pp. 4066–4074, Jul. 2018, doi: 10.1021/acs.jpcclett.8b01593.
- [116] J. Dai, H. Zheng, C. Zhu, J. Lu, and C. Xu, “Comparative investigation on temperature-dependent photoluminescence of CH₃NH₃PbBr₃ and CH(NH₂)₂PbBr₃ microstructures,” *J Mater Chem C Mater*, vol. 4, no. 20, pp. 4408–4413, 2016, doi: 10.1039/c6tc00563b.
- [117] M. Kaiser *et al.*, “How free exciton-exciton annihilation lets bound exciton emission dominate the photoluminescence of 2D-perovskites under high-fluence pulsed excitation at cryogenic temperatures,” *J Appl Phys*, vol. 129, no. 12, Mar. 2021, doi: 10.1063/5.0037800.

- [118] C. Yu *et al.*, “Temperature dependence of the band gap of perovskite semiconductor compound CsSnI₃,” *J Appl Phys*, vol. 110, no. 6, Sep. 2011, doi: 10.1063/1.3638699.
- [119] Y. Du *et al.*, “Temperature-Dependent Luminescence and Anisotropic Optical Properties of Centimeter-Sized One-Dimensional Perovskite Trimethylammonium Lead Iodide Single Crystals,” *Journal of Physical Chemistry Letters*, vol. 13, no. 24, pp. 5451–5460, Jun. 2022, doi: 10.1021/acs.jpcclett.2c01045.
- [120] Y. Song *et al.*, “Temperature-dependent photoluminescence of cesium lead halide perovskite (CsPbX₃, X = Br, Cl, I) quantum dots,” *Mater Res Express*, vol. 6, no. 11, Oct. 2019, doi: 10.1088/2053-1591/ab4911.
- [121] P. Dey *et al.*, “Origin of the temperature dependence of the band gap and PbSe quantum dots of PbS,” *Solid State Commun*, vol. 165, pp. 49–54, 2013, doi: 10.1016/j.ssc.2013.04.022.
- [122] R. L. Milot, G. E. Eperon, H. J. Snaith, M. B. Johnston, and L. M. Herz, “Temperature-Dependent Charge-Carrier Dynamics in CH₃NH₃PbI₃ Perovskite Thin Films,” *Adv Funct Mater*, vol. 25, no. 39, pp. 6218–6227, Oct. 2015, doi: 10.1002/adfm.201502340.
- [123] G. Mannino *et al.*, “Temperature-Dependent Optical Band Gap in CsPbBr₃, MAPbBr₃, and FAPbBr₃ Single Crystals,” *Journal of Physical Chemistry Letters*, vol. 11, no. 7, pp. 2490–2496, Apr. 2020, doi: 10.1021/acs.jpcclett.0c00295.
- [124] J. Wu *et al.*, “Unusual properties of the fundamental band gap of InN,” *Appl Phys Lett*, vol. 80, no. 21, pp. 3967–3969, May 2002, doi: 10.1063/1.1482786.

- [125] Z. M. Gibbs *et al.*, “Temperature dependent band gap in PbX (X = S, Se, Te),” *Appl Phys Lett*, vol. 103, no. 26, Dec. 2013, doi: 10.1063/1.4858195.
- [126] D. Shi *et al.*, “Low trap-state density and long carrier diffusion in organolead trihalide perovskite single crystals,” *Science (1979)*, vol. 347, no. 6221, pp. 519–522, 2015, [Online]. Available: <https://www.science.org>
- [127] A. Balcioglu, R. K. Ahrenkiel, and F. Hasoon, “Deep-level impurities in CdTe/CdS thin-film solar cells,” *J Appl Phys*, vol. 88, no. 12, pp. 7175–7178, Dec. 2000, doi: 10.1063/1.1326465.
- [128] Y. Zhang *et al.*, “Nucleation-controlled growth of superior lead-free perovskite Cs₃Bi₂I₉ single-crystals for high-performance X-ray detection,” *Nat Commun*, vol. 11, no. 1, Dec. 2020, doi: 10.1038/s41467-020-16034-w.
- [129] Z. Fan *et al.*, “Solution-Processed MAPbBr₃ and CsPbBr₃ Single-Crystal Detectors with Improved X-Ray Sensitivity via Interfacial Engineering,” *Physica Status Solidi (A) Applications and Materials Science*, vol. 217, no. 9, May 2020, doi: 10.1002/pssa.202000104.
- [130] W. Wei *et al.*, “Monolithic integration of hybrid perovskite single crystals with heterogenous substrate for highly sensitive X-ray imaging,” *Nat Photonics*, vol. 11, no. 5, pp. 315–321, May 2017, doi: 10.1038/nphoton.2017.43.
- [131] H. Wei *et al.*, “Sensitive X-ray detectors made of methylammonium lead tribromide perovskite single crystals,” *Nat Photonics*, vol. 10, no. 5, pp. 333–339, May 2016, doi: 10.1038/nphoton.2016.41.

- [132] Y. He, I. Hadar, and M. G. Kanatzidis, “Detecting ionizing radiation using halide perovskite semiconductors processed through solution and alternative methods,” *Nature Photonics*, vol. 16, no. 1. Nature Research, pp. 14–26, Jan. 01, 2022. doi: 10.1038/s41566-021-00909-5.
- [133] Y. Li *et al.*, “Bandgap tuning strategy by cations and halide ions of lead halide perovskites learned from machine learning,” *RSC Adv*, vol. 11, no. 26, pp. 15688–15694, Apr. 2021, doi: 10.1039/d1ra03117a.
- [134] A. M. A. Leguy *et al.*, “Experimental and theoretical optical properties of methylammonium lead halide perovskites,” *Nanoscale*, vol. 8, no. 12, pp. 6317–6327, Mar. 2016, doi: 10.1039/c5nr05435d.
- [135] M. Caputo *et al.*, “Electronic structure of MAPbI₃ and MAPbCl₃: importance of band alignment,” *Sci Rep*, vol. 9, no. 1, Dec. 2019, doi: 10.1038/s41598-019-50108-0.
- [136] H. P. Hsu, L. C. Li, M. Shellaiah, and K. W. Sun, “Structural, Photophysical, and Electronic Properties of CH₃NH₃PbCl₃ Single Crystals,” *Sci Rep*, vol. 9, no. 1, Dec. 2019, doi: 10.1038/s41598-019-49926-z.
- [137] X. Cheng, L. Jing, Y. Zhao, S. Du, J. Ding, and T. Zhou, “Crystal orientation-dependent optoelectronic properties of MAPbCl₃ single crystals,” *J Mater Chem C Mater*, vol. 6, no. 6, pp. 1579–1586, 2018, doi: 10.1039/c7tc05156e.
- [138] H. Wei *et al.*, “Dopant compensation in alloyed CH₃NH₃PbBr_{3-x} Cl_x perovskite single crystals for gamma-ray spectroscopy,” *Nat Mater*, vol. 16, no. 8, pp. 826–833, Aug. 2017, doi: 10.1038/nmat4927.

- [139] L. T. Mix *et al.*, “Hot carrier cooling and recombination dynamics of chlorine-doped hybrid perovskite single crystals,” *Journal of Physical Chemistry Letters*, vol. 11, no. 19, pp. 8430–8436, Oct. 2020, doi: 10.1021/acs.jpcclett.0c02243.
- [140] L. Bergman, X. B. Chen, J. L. Morrison, J. Huso, and A. P. Purdy, “Photoluminescence dynamics in ensembles of wide-band-gap nanocrystallites and powders,” *J Appl Phys*, vol. 96, no. 1, pp. 675–682, Jul. 2004, doi: 10.1063/1.1759076.
- [141] C. Yi *et al.*, “Entropic stabilization of mixed A-cation ABX₃ metal halide perovskites for high performance perovskite solar cells,” *Energy Environ Sci*, vol. 9, no. 2, pp. 656–662, Feb. 2016, doi: 10.1039/c5ee03255e.
- [142] M. Saliba *et al.*, “Cesium-containing triple cation perovskite solar cells: Improved stability, reproducibility and high efficiency,” *Energy Environ Sci*, vol. 9, no. 6, pp. 1989–1997, Jun. 2016, doi: 10.1039/c5ee03874j.
- [143] A. Walsh, “Principles of chemical bonding and band gap engineering in hybrid organic-inorganic halide perovskites,” *Journal of Physical Chemistry C*, vol. 119, no. 11, pp. 5755–5760, Mar. 2015, doi: 10.1021/jp512420b.
- [144] M. E. A. Madjet *et al.*, “Enhancing the carrier thermalization time in organometallic perovskites by halide mixing,” *Physical Chemistry Chemical Physics*, vol. 18, no. 7, pp. 5219–5231, 2016, doi: 10.1039/c5cp06603d.
- [145] W. Wei *et al.*, “Monolithic integration of hybrid perovskite single crystals with heterogenous substrate for highly sensitive X-ray imaging,” *Nat Photonics*, vol. 11, no. 5, pp. 315–321, May 2017, doi: 10.1038/nphoton.2017.43.

- [146] G. R. Monama, K. E. Ramohlola, E. I. Iwuoha, and K. D. Modibane, “Progress on perovskite materials for energy application,” *Results in Chemistry*, vol. 4. Elsevier B.V., Jan. 01, 2022. doi: 10.1016/j.rechem.2022.100321.
- [147] A. S. R. Bati, Y. L. Zhong, P. L. Burn, M. K. Nazeeruddin, P. E. Shaw, and M. Batmunkh, “Next-generation applications for integrated perovskite solar cells,” *Communications Materials*, vol. 4, no. 1. Springer Nature, Dec. 01, 2023. doi: 10.1038/s43246-022-00325-4.
- [148] N. Suresh Kumar and K. Chandra Babu Naidu, “A review on perovskite solar cells (PSCs), materials and applications,” *Journal of Materiomics*, vol. 7, no. 5, pp. 940–956, Sep. 2021, doi: 10.1016/j.jmat.2021.04.002.
- [149] T. H. Bui and J. H. Shin, “Perovskite materials for sensing applications: Recent advances and challenges,” *Microchemical Journal*, vol. 191. Elsevier Inc., Aug. 01, 2023. doi: 10.1016/j.microc.2023.108924.
- [150] L. Ortega-San-Martin, “Introduction to perovskites,” in *Perovskite Ceramics: Recent Advances and Emerging Applications*, Elsevier, 2022, pp. 3–29. doi: 10.1016/B978-0-323-90586-2.00015-2.
- [151] C. He and X. Liu, “The rise of halide perovskite semiconductors,” *Light Sci Appl*, vol. 12, no. 1, Dec. 2023, doi: 10.1038/s41377-022-01010-4.
- [152] C. H. Lin *et al.*, “Electrode Engineering in Halide Perovskite Electronics: Plenty of Room at the Interfaces,” *Advanced Materials*, vol. 34, no. 18. John Wiley and Sons Inc, May 01, 2022. doi: 10.1002/adma.202108616.

- [153] D. Luo *et al.*, “Dual-Source Precursor Approach for Highly Efficient Inverted Planar Heterojunction Perovskite Solar Cells,” *Advanced Materials*, vol. 29, no. 19, May 2017, doi: 10.1002/adma.201604758.
- [154] L. Zuo *et al.*, “Enhanced photovoltaic performance of CH₃NH₃PbI₃ perovskite solar cells through interfacial engineering using self-assembling monolayer,” *J Am Chem Soc*, vol. 137, no. 7, pp. 2674–2679, Feb. 2015, doi: 10.1021/ja512518r.
- [155] Z. Wang and Y. Jiang, “Advances in perovskite solar cells: Film morphology control and interface engineering,” *Journal of Cleaner Production*, vol. 317. Elsevier Ltd, Oct. 01, 2021. doi: 10.1016/j.jclepro.2021.128368.
- [156] Y. Liu *et al.*, “Understanding interface engineering for high-performance fullerene/perovskite planar heterojunction solar cells,” *Adv Energy Mater*, vol. 6, no. 2, Jan. 2016, doi: 10.1002/aenm.201501606.
- [157] S. Demchyshyn *et al.*, “Designing Ultraflexible Perovskite X-Ray Detectors through Interface Engineering,” *Advanced Science*, vol. 7, no. 24, Dec. 2020, doi: 10.1002/advs.202002586.
- [158] Z. Yang *et al.*, “Review on Practical Interface Engineering of Perovskite Solar Cells: From Efficiency to Stability,” *Solar RRL*, vol. 4, no. 2. Wiley-VCH Verlag, Feb. 01, 2020. doi: 10.1002/solr.201900257.
- [159] Y. Bai, X. Meng, and S. Yang, “Interface Engineering for Highly Efficient and Stable Planar p-i-n Perovskite Solar Cells,” *Advanced Energy Materials*, vol. 8, no. 5. Wiley-VCH Verlag, Feb. 15, 2018. doi: 10.1002/aenm.201701883.

- [160] J. T. Tisdale *et al.*, “Dynamic Impact of Electrode Materials on Interface of Single-Crystalline Methylammonium Lead Bromide Perovskite,” *Adv Mater Interfaces*, vol. 5, no. 18, Sep. 2018, doi: 10.1002/admi.201800476.

Curriculum Vitae

Kaleab Ayalew

Education

Ph.D. in Mechanical Engineering, candidate, 4.0 GPA, University of Nevada Las Vegas, 12/2023

Graduate Certificate in Nuclear Criticality Safety, University of Nevada Las Vegas, 12/2023

Graduate Certificate in Nuclear Nonproliferation and Safeguards, University of Nevada Las Vegas,
12/2023

M.S. in Mechanical Engineering, University of Nevada Las Vegas, 7/2019

Bachelor of Science in Mechanical Engineering (B.S.M.E.), Addis Ababa University, Addis
Ababa, Ethiopia, 2016

Email Kaleab.aw@gmail.com